

PHOTOCATALYTIC ACTIVITY AND DYE-SENSITIZED SOLAR CELL PERFORMANCE
OF HIGH ASPECT RATIO TITANIUM DIOXIDE NANOFLOAKES

By

YANG-YAO LEE

A DISSERTATION PRESENTED TO THE GRADUATE SCHOOL
OF THE UNIVERSITY OF FLORIDA IN PARTIAL FULFILLMENT
OF THE REQUIREMENTS FOR THE DEGREE OF
DOCTOR OF PHILOSOPHY

UNIVERSITY OF FLORIDA

2010

© 2010 Yang-Yao Lee

To my wife, Hung-Ju, who companies me with endless support.

ACKNOWLEDGMENTS

I would first thank my advisor, Dr. Kevin Powers, for his patience, enthusiasm, and wisdom. He always guided me to observe and think my work scientifically. I also would like to thank my co-chair, Dr. El-Shall, for introducing the concept of statistics design of experiment to me. He helped me develop the engineering aspect of scientific work.

I would like to acknowledge my committee members, Dr. Rajiv Singh, Dr. Ronald Baney, and Dr. Myoseon Jang for their invaluable discussions and suggestions. Special thanks to Dr. Arun Ranade at Particle System, LLC. for his compassion and support through the project.

I express my gratitude to my parents who endlessly supported me throughout my Ph.D. and always encouraged me to continue my dreams. I am always grateful for having your support with me.

I especially thank my wife, Hung-Ju, for lasting encouragement and support. She helped me in every aspect of life in United States. Thanks for her selfless sacrifice.

I gratefully acknowledge my group members including Dr. Nate Stevens, Dr. Steve Tedeschi, Ming-Chi “Tim” Yang, Gary Scheiffele, Gill Brubaker, Kerry Siebein, Jiaqing Zhou, Paul Carpinone, David Wiggins and all the staff of the Particle Engineering Research Center for their help in all aspects of my research.

Finally, I acknowledge the Particle Engineering Research Center for financial support and friendly environment for carrying out research.

TABLE OF CONTENTS

	<u>page</u>
ACKNOWLEDGMENTS	4
LIST OF TABLES	7
LIST OF FIGURES	9
ABSTRACT.....	15
CHAPTER	
1 INTRODUCTION	17
The Most Essential Component of Life: Water	17
Traditional Wastewater Treatments	17
Advanced Oxidation Processes (AOPs)	18
The Coming Global Energy Crisis	18
Finite Energy Source: Fossil Fuels.....	19
Alternative Clean Energy Demand.....	20
The Remedy for Energy Crisis: Nanotechnology?.....	20
Gap Analysis and Statement of Problem.....	22
2 BACKGROUND	24
Photocatalysis on Titanium Dioxide Surface	24
Photocatalyst Loading	27
Light Intensity	28
pH	28
Temperature.....	29
Oxygen Pressure.....	29
Charge separation.....	30
Generation of active species.....	30
Maintenance of the stoichiometry of titania.....	30
Enhanced of Photocatalysis	31
Size Reduction.....	31
Shape Control	32
Doping (Narrowing Band Gap)	34
3 HIGH ASPECT RATIO titanium dioxide FLAKES AS PHOTOCATALYSTS	41
Synthesis of High Aspect Ratio of TiO ₂ Flakes	41
Benchmark: Degussa® P25	49
Experiment Apparatus	49
Photocatalytic Degradation of Dye Molecules under UVA Light Illumination.....	50
Statistical Design of Experiments.....	52

	Synthesized Flakes	53
	Calcined Flakes	55
	P25	56
4	TRANSITION METAL DOPING OF TITANIA PARTICIELS AS VISIBLE PHOTOCATALYSTS.....	87
	Synthesis of Vanadium Doped Titania Flakes.....	87
	Characterization of Vanadium Doped TiO ₂ Flakes.....	87
	XPS Spectra of Series Vanadium Doped Flakes	92
	Experiment Apparatus	94
	Statistical Design of Experiments.....	97
5	TITANIA NANOFLAKES BASED DYE-SENSITIZED SOLAR CELLS.....	125
	Introduction.....	125
	Basic Principles and Components of DSSCs	125
	The Energetic Aspect of DSSCs.....	126
	Experiment.....	127
	Photoelectrodes Characterization	128
	Photovoltaic Measurements.....	129
	Assembling DSSCs using High Aspect Ratio Titania Particles	129
	Characterization of Titania Photoelectrodes	130
	Photovoltaic Performance of Titania Photoelectrodes	134
6	SUMMARY, CONCLUSIONS, AND FUTURE WORK	149
	Summary.....	149
	Conclusions.....	150
	Future Work.....	151
APPENDIX		
A	ANALYSIS VARIANCE FOR UV PHOTOCATALYSIS USING SYNTHESIZED FLAKES	152
B	ANALYSIS VARIANCE FOR UV PHOTOCATALYSIS USING CALCINED FLAKES	154
C	ANALYSIS VARIANCE FOR UV PHOTOCATALYSIS USING P25 NANOPARTICLES	155
D	ANALYSIS VARIANCE FOR VISIBLE PHOTOCATALYSIS USING VANADIUM DOPED FLAKES	156
	LIST OF REFERENCES	157
	BIOGRAPHICAL SKETCH	167

LIST OF TABLES

<u>Table</u>	<u>page</u>
2-1 Bulk properties of three TiO ₂ polymorphs [24].	37
2-2 Oxidation power of species [26].	37
3-1 Particle diameter statistics for synthesized and calcined flakes.	57
3-2 Grain size calculation by the Scherer equation for both nanoflakes.	57
3-3 Physisorption measurements of P25, synthesized and calcined titania nanoflakes.	57
3-4 Optical and electrostatic properties of titania samples.	57
3-5 Pseudo-first order rate constants of methylene blue under photocatalytic degradation.	57
3-6 The 2 ³ factorial design used to investigate the most important factors for UV light photocatalysis.	58
4-2 Grain size calculation by the Scherer equation for series calcined vanadium doped nanoflakes.	100
4-3 Physisorption measurements of P25, and series calcined vanadium doped titania nanoflakes.	100
4-4 V/Ti molar ratio and band gap energy of series vanadium doped samples.	100
4-5 Pseudo-first order rate constants of methylene blue under visible photocatalytic degradation.	101
4-6 The 2 ³ factorial design used to investigate the most important factors for visible light photocatalysis.	101
5-1 Particle diameter statistics for P25, synthesized and calcined flakes after ultrasonication.	136
5-2 Dye loading and physisorption measurements of P25, synthesized and calcined titania nanoflakes.	136
5-3 Photovoltaic properties of the dye sensitized solar cells assembled by using anodes made from P25 nanoparticles and calcined titania flakes of different thickness.	136
A-1 Analysis of variance table	152
A-2 Statistical results	153
B-1 Analysis of variance table	154

B-2	Statistical results	154
C-1	Analysis of variance table.....	155
D-1	Analysis of variance table.....	156
D-2	Statistical results	156

LIST OF FIGURES

<u>Figure</u>	<u>page</u>
2-1	Schematic representation of the photoelectrochemical mechanism taking place inside titania:38
2-2	Schematic photoexcitation in a solid followed by deexcitation events38
2-3	Secondary reactions with active oxygen species in the photoelectrochemical mechanism39
2-4	The schematic diagram of conduction and valence bands positions of several semiconductors. The left hand scale is the internal energies to the vacuum level and the right hand scale represented the comparison to normal hydrogen electrode (NHE) ...39
2-5	Schematic energy level diagram of metal doped TiO ₂40
3-1	Photographs of titania slurries.59
3-2	Optical micrographs of titania samples.....59
3-3	SEM images of titania samples.....60
3-4	SEM images of edge view of titania samples.60
3-5	Particle size distribution for synthesized and calcined flakes.....61
3-6	XRD patterns of titania samples.61
3-7	HR-TEM images of titania samples (the SAD pattern as inset).62
3-8	XPS analysis of the titania samples.63
3-9	UV-Visible spectra of titania samples. A) Diffuse reflectance spectra. B) the dependence of $(\alpha h\nu)^2$ on the photon energy for synthesized and calcined titania flakes.64
3-11	True absorption spectra of titania samples using the modified integration sphere method. (note: reflectivity in an integrating sphere is provided by a coating of pigment grade TiO ₂ or ZnO. Thus the absorbance above represents only the increased absorbance over the control.).....65
3-12	Zeta potential versus solution pH for three titania samples.....66
3-13	Photocatalytic decomposition of 50 μ M methylene blue with synthesized titania flakes under UVA illumination.....66

3-14	Photocatalytic decomposition of methylene blue by using synthesized and calcined flakes. A) without bubbling treatment. B) with bubbling treatment.	67
3-15	Linear transforms $-\ln(C/C_0)$ vs. time for methylene blue decomposition for different photocatalysts. A) without bubbling treatment. B) with bubbling treatment. Note the difference in scales of the normalized concentrations.	68
3-16	Experimental design decomposition% results of synthesized flakes photocatalysis.	69
3-17	The 3D response surface plot of dye decomposition% of synthesized flakes as a function of the factor A and B under different light intensity. A) 2. B) 4. C) 6.	70
3-18	Model graphs of synthesized flakes as the function of A and B at constant light intensity (C = 2). A) Contour plot of decomposition% B) Interaction plot of response data against factor A for both levels of factor B.	71
3-19	Model graphs of synthesized flakes as the function of A and B at constant light intensity (C = 6). A) Contour plot of decomposition%. B) Interaction plot of response data against factor A for both levels of factor B.	72
3-20	The 3D response surface plot of dye decomposition% of synthesized flakes as a function of the factor B and C under different aeration. A) 0. B) 5. C) 10 ft ³ /hr.	73
3-21	Model graphs of synthesized flakes as the function of B and C at constant flow rate (A = 0). A) Contour plot of decomposition%. B) Interaction plot of response data against factor B for both levels of factor C.	74
3-22	Model graphs of synthesized flakes as the function of B and C at constant flow rate (A = 10). A) Contour plot of decomposition% of synthesized flakes B) Interaction plot of response data against factor B for both levels of factor C.	75
3-23	Experimental design decomposition% results of calcined flakes photocatalysis.	76
3-24	The 3D response surface plot of dye decomposition% of calcined flakes as a function of the factor A and B under different light intensity. A) 2. B) 4. C) 6.	77
3-25	Model graphs of calcined flakes as the function of A and B at constant light intensity (C = 2). A) Contour plot of decomposition%. B) Interaction plot of response data against factor A for both levels of factor B.	78
3-26	Model graphs of calcined flakes as the function of A and B at constant light intensity (C = 6). A) Contour plot of decomposition%. B) Interaction plot of response data against factor A for both levels of factor B.	79
3-27	The 3D response surface plot of dye decomposition% of calcined flakes as a function of the factor B and C at different aeration rate. A) 0. B) 5. C) 10 ft ³ /hr.	80

3-28	Model graphs of calcined flakes as the function of B and C at constant flow rate (A = 0). A) Contour plot of decomposition% of calcined flakes. B) Interaction plot of response data against factor B for both levels of factor C.	81
3-29	Model graphs of calcined flakes as the function of B and C with constant flow rate (A = 10). A) Contour plot of decomposition%. B) Interaction plot of response data against factor B for both levels of factor C.	82
3-30	Experimental design decomposition% results of P25 photocatalysis.	83
3-31	The 3D response surface plot of dye decomposition% of P25 as a function of the catalyst concentration and Flow rate under different light intensity. A) 2. B) 4. C) 6.	84
3-32	The 3D response surface plot of dye decomposition% of P25 as a function of the catalyst concentration and light intensity at different aeration rate. A) 0. B) 5. C) 10 ft ³ /hr.	85
3-33	Interaction plot of response data against factor B for both levels of factor C at different aeration rate for P25. A) 0. B) 5. C) 10 ft ³ /hr.	86
4-1	Photographs of synthesized vanadium doped titanium dioxide flakes. A) 1. B) 5. C) 10 atomic% vanadium (note the pearlescence of the samples).	102
4-2	Photographs of calcined vanadium doped titanium dioxide flakes. A) 1. B) 5. C) 10 atomic% vanadium (note the pearlescence of the samples).	102
4-3	Optical micrographs of vanadium doped titanium dioxide flakes. A) synthesized. B) calcined 5 atomic% vanadium doped flakes.	103
4-4	Optical micrographs of calcined vanadium doped flakes. A) 1. B) 10 atomic% vanadium.	103
4-5	SEM images of synthesized 5 atomic% vanadium doped titania nanoflakes. A) surface morphology. B) thickness. C) EDX. D) mapping.	104
4-6	SEM images of calcined 5 atomic% vanadium doped titania nanoflakes. A) surface morphology. B) thickness. C) EDX. D) mapping.	105
4-7	SEM images of calcined 1 atomic% vanadium doped titania nanoflakes. A) surface morphology. B) thickness. C) EDX. D) mapping.	106
4-8	SEM images of calcined 10 atomic% vanadium doped titania nanoflakes. A) surface morphology. B) thickness. C) EDX. D) mapping.	107
4-9	Volume based particle size distribution for synthesized and calcined vanadium doped flakes. A) 1. B) 5. C) 10 atomic% vanadium.	108

4-10	XRD patterns of vanadium doped flakes. A) 5 atomic% vanadium. B) Anatase (101) peak for series calcined vanadium doped flakes (at slow scanning mode: 0.01 °/step)...109	109
4-11	Zeta potential of the vanadium doped flakes as the function of pH. A) 0, 1, 5, 10 atomic% vanadium B) The IEP versus the amount of vanadium in the series vanadium doped flakes.110	110
4-12	Diffuse reflectance spectra of vanadium doped titania flakes. A) 5 atomic% vanadium. B) the absorbance spectra for synthesized and calcined vanadium doped titania flakes.111	111
4-13	The true absorption spectra of vanadium doped flakes. A) series synthesized vanadium doped flakes. B) series calcined vanadium doped flakes. C) photoresponse of series vanadium doped flakes in the visible range.112	112
4-14	XPS spectra of vanadium doped flakes. A) O 1s and V 2p _{3/2} peaks for series vanadium doped flakes (b) V 2p _{3/2} peak of 10 atomic% vanadium doped flakes.113	113
4-15	XPS spectra of Ti 2p _{3/2} and Ti 2p _{1/2} peaks for vanadium doped flakes. A) series vanadium doped flakes. B) Ti 2p _{3/2} peak of 10 atomic% vanadium doped flakes.114	114
4-16	XPS spectra of O 1s peak fitting.....115	115
4-17	Visible photocatalytic decomposition of methylene blue by using vanadium doped titania flakes with three vanadium doping levels under bubbling condition.116	116
4-18	Linear transforms $-\ln(C/C_0)$ vs. time for methylene blue decomposition for vanadium doped titania flakes with three vanadium doping levels under bubbling.....116	116
4-19	Linear transforms $-\ln(C/C_0)$ vs. time for methylene blue decomposition for vanadium doped titania flakes with three vanadium doping levels under bubbling condition. (Note the difference in scales of the normalized concentrations).....117	117
4-20	Comparison of the ratio of V ⁴⁺ /V ⁵⁺ and photocatalytic reaction rate for series vanadium doped flakes.117	117
4-21	Experimental design visible light decomposition% results of vanadium doped titania flakes photocatalysis with three different doping levels.....118	118
4-22	The 3D response surface plot of dye decomposition% of series calcined vanadium doped flakes as the factor A and B under different aeration rate.....119	119
4-23	Model graphs of series vanadium doped flakes as the function of B and C at constant aeration rate (A = 0). A) Contour plot of decomposition% of series vanadium doped flakes. B) Interaction plot of response data against factor B for both levels of factor C.....120	120

4-24	Model graphs of series vanadium doped flakes as the function of B and C at constant aeration rate (A =10). A) Contour plot of decomposition% of series vanadium doped flakes. B) Interaction plot of response data against factor B for both levels of factor C.....	121
4-25	The 3D response surface plot of dye decomposition% of series calcined vanadium doped flakes as the factor B and C.....	122
4-26	Model graphs of calcined 1 atomic% vanadium doped flakes as the function of A and B. A) Contour plot of decomposition%. B) Interaction plot of response data against factor A for both levels of factor B.....	123
4-27	Model graphs of calcined 5 atomic% vanadium doped flakes as the function of A and B. A) Contour plot of decomposition%. B) Interaction plot of response data against factor A for both levels of factor B.....	124
5-1	Schematic structure of DSSCs [163].	137
5-2	Energy levels in the typical DSSCs [164].....	137
5-3	Typical I-V curves of the solar cells. (The fill factor, FF, could be calculated by the ratio of the area A to the area B).....	138
5-4	Schematic cross sectional view of electron transport through titania layer. A) Degussa P25 nanoparticles. B) calcined titania nanoflakes (two dimensional nanostructures).....	139
5-5	Optical micrographs of sintered titania photoelectrodes made from Degussa P25 nanoparticles. A) 5. B) 50 magnifications.	140
5-6	Optical micrographs of sintered titania photoelectrodes made from calcined titania flakes. A) 5. B) 50 magnifications.	140
5-7	SEM micrographs of sintered photoelectrodes made from P25 nanoparticles under different magnifications.	141
5-8	Cross section of sintered photoelectrodes made from P25 nanoparticles under different magnifications.	141
5-9	SEM micrographs of sintered photoelectrodes made from calcined titania flakes under different magnifications.	142
5-10	Cross section of sintered photoelectrodes made from calcined titania flakes under different magnifications.	142
5-11	SEM images of platinum counterelectrode. A) surface morphology. B) thickness. C) EDX. D) mapping.	143

5-12	Particle size distribution of titania slurries for P25, synthesized and calcined titania flakes after ultrasonication at 100W for 15 minutes.	144
5-13	Absorption spectrum of 0.3 mM Ru complex dye solution (also as known N-719 dye).	144
5-14	Diffuse reflectance spectra of the titania films prepared from Degussa P25 nanoparticles, synthesized and calcined titania flakes of similar thickness.....	145
5-15	I-V curves of dye sensitized solar cells with different film thicknesses. A) calcined titania flakes. B) P25.....	146
5-17	Comparison of the Jsc and Voc of P25 and calcined flakes cells as a function of film thickness.....	148

Abstract of Dissertation Presented to the Graduate School
of the University of Florida in Partial Fulfillment of the
Requirements for the Degree of Doctor of Philosophy

PHOTOCATALYTIC ACTIVITY AND DYE-SENSITIZED SOLAR CELL PERFORMANCE
OF HIGH ASPECT RATIO TITANIUM DIOXIDE NANOFLAKES

By

Yang-Yao Lee

December 2010

Chair: Kevin William Powers

Cochair: Hassan El-Shall

Major: Materials Science and Engineering

Protection of clean water sources and exploring clean energy resources are two of the most important issues in the 21st century. Although advanced oxidation processes with titanium dioxide (TiO₂) photocatalytic nanoparticles have been a somewhat effective alternative in this regard, the low quantum efficiency of the TiO₂ semiconductor and the difficulty of separation from water prevent practical applications. Therefore, there is a need to develop a novel material with higher photocatalytic activity to develop viable commercial products.

The first goal of this research project is to develop a cost efficient, and easily separated photocatalyst for water purification. This goal was achieved by synthesizing TiO₂ nanoflakes with enhanced quantum yield. The synthesis of nanoflakes has been chosen for increased quantum efficiency and their ease of separation. The results showed that titania flakes have higher photocatalytic activity than the reference commercial product, Degussa P25. Ultimately, more than 99% of methylene blue molecules (150 ml of 50 μ M) in simulated wastewater were decomposed within 2 hours by adding 100 ppm of TiO₂ nanoflakes under UVA light illumination. From the energy aspect, a more energy-efficient way for purifying the polluted water needs to be developed.

Transition metal doping has been shown to extend the absorption edge of TiO₂ from the UV into visible region (~ 2.8 eV). In these studies, it is proposed to investigate the factors affecting their photocatalytic activities under visible light. Ultimately, it was shown that vanadium doped flakes at 1 atomic % exhibited the highest visible photocatalytic activity.

Due to the depletion of fossil fuel in the future, many researchers focused on finding renewable energy sources. Of the many different types of solar cells, the dye-sensitized solar cell (DSSC) is a promising device with sufficiently low manufacturing cost to compete in the commercial market place. In this study, titania nanoflakes were used to prepare the semiconductor layer of DSSC. The highest efficiency of nanoflake-based cell was 7.4% and 5 fold improvement was achieved by replacing P25 nanoparticles with calcined titania flakes in the photoelectrodes on the basis of film thickness.

CHAPTER 1 INTRODUCTION

The Most Essential Component of Life: Water

Water is one of the most essential substances for life. The total amount of water in the world is about 1.4 billion km³ and only 2.5% or 35 million km³ is considered freshwater suitable for human usage [1]. The continued explosive growth in the human population has increased the demand for this limited supply of freshwater. According to the World Health Organization (WHO) [2], more than 40% of the world population suffers from the chronic shortage or lack of water due to political, economical and climatological reasons. Health and hygienic problems related to water affects more than 25% of the world's population. Despite the plans carried out by United Nations (UN) in recent years, 1.1 billion people still do not have access to adequate water supplies and sanitation. This condition is especially concentrated in the underdeveloped countries of Africa, Asia, and Latin America [2]. Moreover, the increasing domestic and industrial activities generate high amounts of polluted water which directly flow into natural channels of water bodies. Therefore, protecting the cleanliness of our water sources is one of the most important environmental issues in the 21st century.

Traditional Wastewater Treatments

There are many different pollutants involved with the contamination of environmental water such as detergents, pesticides, herbicides, solvent and chemical wastes produced by industries. The conventional wastewater treatments used can be classified as physical, biological, and chemical. Physical water treatment methods include UV light irradiation and filtration. Biological treatment uses bacteria to treat leachates. Chemical treatment uses chlorine to eliminate microorganisms. Although the most popular methods for wastewater treatment are biological methods due to low costs, they have been largely unsuccessful in the removal of many

contaminants such as pesticides since these tend to be toxic to the microorganisms used.

Chemical treatments are limited due to high costs and slow reaction times.

Advanced Oxidation Processes (AOPs)

Advanced oxidation processes (AOPs) present a promising way of decomposing biologically and chemically stable molecules in waste. Reviews on this topic have been published recently [2-4]. Although there are many different systems, the common mechanism of AOPs is the oxidation and mineralizing of organic species using hydroxyl radicals ($OH \bullet$) and other reactive oxygen species. Although the strong ability of AOPs for eliminating hazard compounds in the wastewater is recognized, the operating costs for total oxidation of the organic molecules are still more expensive than the conventional biological treatments. However, in many instances, they are suitable for pre-treatment or enhancement of the biodegradation. The use of solar energy can improve not only the economics, but also contribute in process sustainability by saving electricity. In addition, the AOPs can be used to remediate almost any kind of wastewater containing harmful organic compounds. Among these different systems of AOPs, titanium dioxide (TiO_2) is a well-studied, chemical stable, environmentally friendly, reusable, and most importantly, inexpensive material. Therefore, we propose to use TiO_2 as the water treatment reagent in this study.

The Coming Global Energy Crisis

The booming economic growth in the World over the past few decades was mainly supported by the affordable energy costs. The majority of energy sources, about 80-85%, come from fossil fuels which are a product refined from the ancient biomass under the earth's surface for more than 200 million years. And the electricity, one of the most vital parts of modern life, is primarily dependent on the combustion of coal, natural gas, and oil. Worldwide population has increased at least four times in the 20th century and consequent energy consumption increment is

up by 16 fold. Currently, the total energy demand per year is about 13 terawatts ($TW = 10^{12}$ watts) for the world's 6.5 billion people [5]. In another 40 years, it is expected to increase to 23 TW for the increasing population to sustain the current lifestyle [5]. Except for the tremendous energy demand in the future, the energy production based on fossil fuels also has the significant impact on the environment. When we produce the energy from burning fossil fuels, pollutants and greenhouse gases were inevitably generated. The current global warming phenomenon has been attributed by many to the emission of greenhouse gases in the atmosphere [6]. The historic high mean surface and ocean temperatures were recorded and stronger and stronger tropical storms and hurricanes have occurred in recent years. The United Nations Framework Convention on Climate Change calls for "stabilization of greenhouse-gas concentrations in the atmosphere at a level that would prevent dangerous anthropogenic interference with the climate system" [7-9]. In one possible proposed scenario, aggressive policy intervention used to limit greenhouse-gas emissions has the potential to ass 10 TW of carbon-emission-free power by the year 2050, equivalent to the power provided by all today's energy sources combined [6].

Finite Energy Source: Fossil Fuels

Hubbert proposed a model to predict the production of oil and found that the current exponential growth in the last century is a transient phenomenon [10,11]. It will not continuously increase in the future and this predictive model fits the peak fossil fuel production in 1970. The total storage of global oil is 2000 billion barrels and 1800 billion barrels have been found [12]. Moreover, we are using 4 billion barrels of fossil fuels for discovering every new billion barrel of oil and total of 875 billion barrel have been consumed. Therefore, we will be forced to diversify our energy supply especially alternative clean energy resources in order to keep not only global economic growth but also healthy environment.

Alternative Clean Energy Demand

There are two major types of energies proposed to fully or partially replace the fossil fuel consuming in the world: nuclear and renewable energies. If we use nuclear power as the main source of energy, 1 Gigawatts of nuclear fission plant will be required to build per day for the following 50 years usage of energy [9]. Furthermore, the undesired high-level radioactive waste in the nuclear reactor remains the most significant pollution problem and had to handle and store with extreme care. According to the United States Environment Protection Agency standard, the radioactive decay life of these spent fuels is up to 10,000 years. Renewable energies mainly come from natural resources such as wind, ocean currents, gravity (hydroelectric), geothermal heat, and sun. Therefore, the renewable energies are the most environmental friendly energy resources in the world due to the nature of the production. They are naturally replenished and estimated to be the amount of electricity as the progressively increasing sequences: hydroelectricity (0.5 TW), ocean currents (2 TW), extractable wind power (2-4 TW), geothermal over the whole surface of earth (12 TW), and solar energy (120000 TW) [9]. Among these energy options, solar energy is the most abundant resource for our energy demand. Total amount of energy consumed annually by the world is equivalent to one hour illumination of sun light irradiation on earth. In spite of the tremendous amount of energy supplied by the sun, only a very small portion of total energy produced (~ 0.01%) comes from the solar energy [9]. The major hurdles of solar energy application are the cost issues and not sufficient efficiency. Therefore, we need more advanced technology with substantially reduced manufacturing cost and improved energy conversion efficiency to fully utilize the solar energy.

The Remedy for Energy Crisis: Nanotechnology?

During the last decade, nanomaterials have been attracted wide attention owing to unique chemical and physical properties. Therefore, nanotechnology has been involved in a vast range

of applications such as medicine, electronics, biomaterials, and energy production. Novel nanomaterials provide advanced strategies for designing next generation energy conversion devices and serve as the building blocks to harvest solar power. The best known energy device for directly utilizing solar energy is the solar cell which is able to convert sun light directly into electricity by the photovoltaic effect. There are three major classifications for solar cell based on the generation: silicon bulk heterojunction cells (first generation), the CuInGaSe₂ (CIGS) cells (second generation), and organic and inorganic solar cells (third generation). Single crystalline silicon cells currently provide the highest efficiency (up to 15%) but suffer from high manufacturing cost [7]. With such efficiency, the sale price of grid generated electricity is about \$0.25 to \$0.30 per kilowatt-hour (kWh) which is much higher than the current price of utility scale electricity production (\$0.03 to \$0.05 kWh) [7]. The second generation devices made with CIGS thin film bring down the cost significantly but the efficiency is not high enough for practical application. Among the third generation of solar cells, dye-sensitized solar cells (DSSCs) provide an efficient method to mimic the natural photosynthesis process. Although the energy conversion efficiency of DSSCs is not as high as it of conventional silicon based solar cell, the price/performance ratio should be high enough to compete with fossil-based electricity. The estimated manufacturing cost of the DSSCs is 1/3-1/5 of the conventional solar cells. One of the key components in the DSSCs is an electron transport layer consisting of the semiconductor materials such as TiO₂, ZnO, and SnO₂. Titanium dioxide is a well known low toxicity, chemically stable, and cost effective material used in many industrial applications. Recently researchers have focused on synthesis of TiO₂ nanostructures with desired shapes such as nanotubes, nanorods, and nanowires. Using these low dimensional nanostructures as the building blocks, new electron transportation pathway could be established and opened a new strategy of

improving energy conversion efficiency of the DSSCs. In this study, we will use our synthesized titania nanoflakes as the starting material and investigate the photon energy conversion efficiency of titania nanoflake-based DSSCs.

Gap Analysis and Statement of Problem

Research focused on the remediation of wastewater has been very limited and most use advanced oxidation processes (AOPs). AOPs are defined as processes that generate hydroxyl radicals with sufficient concentration to oxidize most organic chemicals present in the effluent water. Although AOPs with TiO_2 photocatalysts have been shown to be an effective alternative in this regard, the two major obstacles preventing the use of TiO_2 semiconductors in practical applications is its low quantum efficiency ($< 1\%$) and the requirement of UV light irradiation.

There is extensive literature considering the effect of size on photocatalytic activity especially the use of ultrafine particles. Only a few researchers have studied shape control of titania photocatalysts. Although the photocatalytic efficiency is increased due to the quantization effect of ultrafine particles, absorption in the visible region for nanoparticles tends to decrease. Hence, the first objective of this research is to study the effect of changing shape on photocatalytic behavior. TiO_2 nanoflakes with micron size width but nanoscale thickness create a short diffusion path for charge carriers and reduce surface recombination. In addition the effect of transition metal doping level on the visible light absorption characteristics and subsequent influence on the photocatalysis needs to be investigated systematically. The final goal of this research is to eliminate $> 95\%$ of 50 ppm of organic pollutant in 150 ml wastewater by adding 0.1 g of transition metal doped titania nanoflakes under visible light illumination.

To achieve this goal, experimental and fundamental studies are proposed. In these studies, the effect of changing shape on photocatalytic efficiency under UV and visible irradiation are

compared to conventional photocatalysts. The factors include: light intensity, catalyst loading, aeration rate, and vanadium dopant concentration. The effect of these factors on the final photodegradation behavior has been systematically and experimentally investigated. To do so, undoped and vanadium doped titanium dioxide flakes with high aspect ratios were synthesized by a modified surface hydrolysis method. Then the flakes are directly injected into the stimulated wastewater under UV and visible light. This will facilitate an understanding of the significance and magnitude of each factor on the UV and visible light photocatalysis behavior.

DSSC is a promising solar cell technology with potentially high enough efficiency and cost effective fabrication. However, the overall efficiency has been not maximized and the current technology is not yet cost competitive with the current electrical power generation. The purpose of this study is to investigate the effect of using low dimensional nanomaterials as the alternative materials in the semiconductor layers of the DSSCs. A titania nanoflake-based DSSC with higher efficiency is compared to a P25 based cell. To achieve this goal, calcined titania nanoflakes were used to prepare the titania slurry to deposit on the transparent glass substrate and the photon energy conversion efficiency of the nanoflake-based DSSC was measured under the simulated sun light illumination (AM 1.5). The effect of thickness of semiconductor layer on the photovoltaic performance was also systematically and experimentally investigated.

CHAPTER 2
BACKGROUND

Photocatalysis on Titanium Dioxide Surface

In 1972, Fujishima and Honda discovered the electrochemical photolysis of water on TiO₂ surface [13]. This significant event opened the era of heterogeneous photocatalysis on the environmental application. Titanium dioxide has since attracted much attention because of its unique properties such as high photocatalytic activity, moderate band gap and suitable band position, nontoxicity, availability, and low cost [14,15]. Furthermore, TiO₂ powders also have versatile optical properties in tinting strength, hiding power, and ultraviolet (UV) light shielding. These properties have many industrial applications such as pigments, cosmetics, and so on [14,15]. Figure 2-1 schematically represents the steps of photocatalysis. The main reactions [13,16-20] and the required time measured by laser flash photolysis [21,22] are listed as follows:

- Charge-carrier generation

$$TiO_2 + h\nu \rightarrow h_{VB}^+ + e_{CB}^-, \dots\dots\dots 10^{-15} s$$
- Charge-carrier trapping

$$h_{VB}^+ + >Ti^{IV}OH \rightarrow \{>Ti^{IV}OH \bullet\}^+, \dots\dots\dots 10 \times 10^{-9} s$$

$$e_{CB}^- + >Ti^{IV}OH \leftrightarrow \{>Ti^{III}OH\}^-, \dots\dots\dots 100 \times 10^{-12} s$$

$$e_{CB}^- + >Ti^{IV} \rightarrow >Ti^{III}, \dots\dots\dots 10 \times 10^{-9} s$$
- Charge-carrier recombination

$$e_{CB}^- + \{>Ti^{IV}OH \bullet\}^+ \rightarrow >Ti^{IV}OH, \dots\dots\dots 100 \times 10^{-9} s$$

$$h_{VB}^+ + \{>Ti^{III}OH\}^- \rightarrow >Ti^{IV}OH, \dots\dots\dots 10 \times 10^{-9} s$$
- Oxidation or reduction

$$\{>Ti^{IV}OH \bullet\}^+ + Red^0 \rightarrow >Ti^{IV}OH + Red \bullet^+, \dots\dots\dots 100 \times 10^{-9} s$$

$$e_{TR}^- + O_x \rightarrow >Ti^{IV}OH + O_x \bullet^-, \dots\dots\dots 10^{-3} s$$

where e_{CB}^- is a conduction band electron, h_{VB}^+ is a valence band hole, $>TiOH$ represents the hydrated surface of TiO_2 , $\{>Ti^{IV}OH\bullet\}^+$ is the surface-trapped hole, $\{>Ti^{III}OH\}^-$ is the surface-trapped electron, Red is an electron donor (i.e., reductant), O_x is an electron acceptor (i.e., oxidant).

According to the above equations, the overall photocatalytic efficiency depends on the competition between the interfacial charge-transfer and the electron-hole recombination. Therefore, the photocatalytic reaction will be accelerated by increasing either the lifetime of electron-hole pairs (retarding recombination) or the rate of interfacial charge transfer. From the results of laser flash photolysis, the dominant reaction is the recombination of the electron and hole (1 ns) followed by the reduction reaction (10 ns) and oxidation (1 ms) [21,22]. Figure 2-2 illustrates some of the recombination pathways for electrons and holes [19]. Depending on the location of the sites, there are two types of possible recombinations: surface recombination (path (A)) and volume recombination (path (B)). Both recombinations are detrimental to the efficiency of photocatalysts as energy is released as heat. Several approaches have been tried to suppress the recombination of electron-hole pairs including addition of metals, dopants, or combinations with other semiconductors [19]. More detailed information will be discussed in the following section. The efficiency of photocatalytic process is measured as the quantum yield (Φ) which is defined as the rate of reaction induced by photon absorption / flux of absorbed photon. However, it is very difficult to measure the precise quantity of absorbed light in the heterogeneous system since scattering of light usually occurs at the semiconductor surface. Therefore, most researchers used an assumption that all incident light is absorbed and calculate a so called “apparent” quantum yield. The “apparent” quantum yield will be calculated and compared in this study to elucidate the influence of different samples on a photocatalysis

process. There are eight TiO_2 polymorphs in principle, which are anatase, rutile, brookite, columbite, baddeleyite, cotunnite, pyrite, and fluorite structures [23]. In nature, titania exists three main phases which are rutile, anatase, and brookite, in order of abundance. The basic properties of these three polymorphs are listed in Table 2-1 [24]. Only anatase and rutile showed significant photocatalysis under ultraviolet light irradiation; the former generally has higher photocatalytic activity in general. Only a few investigators have investigated the photocatalysis with the brookite phase, which may be attributed to the difficulty of highly pure brookite synthesis [25].

Since one of the important applications for photocatalysis is water purification, several specific mechanisms for interfacial charge transfer in water are illustrated and listed in the following reactions.

- Specific examples of interfacial charge transfer

$$\{>Ti^{IV}OH\bullet\}^+ + H_2O \rightarrow Ti^{IV}OH + OH\bullet + H^+$$

$$\{>Ti^{IV}OH\bullet\}^+ + OH^- \rightarrow Ti^{IV}OH + OH\bullet$$

$$e_{TR}^- + O_2 \rightarrow Ti^{IV}OH + O_2\bullet^-$$

$$e_{TR}^- + H_2O_2 \rightarrow Ti^{IV}OH + OH\bullet + OH^-$$

From the above reactions, highly reactive species such as hydroxyl radicals ($OH\bullet$) and superoxide ions ($O_2\bullet^-$) could either oxidize or reduce a wide variety of organic compounds in waste water. Elizardo compared many oxidizing agents with chlorine and found that hydroxyl radicals have the highest oxidation power (Table 2-2) [26]. Many researchers assumed that the primary oxidizing species in the photocatalytic reaction are hydroxyl radicals especially in water [17,26]. One of the reasons is the abundant source of hydroxide ions exists in the environment when photocatalysis proceeding in water. However, there is still an argument that the oxidation process occurs at the titania surface formed directly by direct reaction with holes instead of

hydroxyl radicals [27-29]. The quantum yield can be directly related to the generation of hydroxyl radicals and can be rewritten as: $\Phi = \text{generation rate of hydroxyl radicals} / \text{flux of absorbed photon}$. Quantum yields under typical reactor conditions are frequently below 1% [30]. Many researchers have attempted to enhance the photocatalytic efficiency of TiO_2 . However, the previous research has focused on either scavenging the electrons away from the system to prevent recombination, or by retarding the recombination so that a greater proportion of holes will reach the surface and generate $\text{OH} \bullet$ [31]. Furthermore, there are many parameters which were found to affect the photocatalytic degradation rate. Some of them will be discussed in the following sections.

Photocatalyst Loading

The stoichiometry of a photocatalytic reaction in solution is comparable to that of any chemical reaction. It is straightforward that higher dosage concentration leads to more efficient photocatalytic reaction because of more adsorption and decomposition at higher available specific surface area [32]. In any given experiment, an optimum value of photocatalyst loading should be explored to avoid the waste of materials and fully utilize total incident photons. When adding excess catalysts into the system, reduction of quantum yield was observed due to undesired light scattering of titania particles and then diminution of light penetration in the solution.

There is also a relationship between photocatalyst concentration and type of reactor. Two main kinds of reactors have been used in the photocatalytic application: immobilized and slurry reactors. In the immobilized system, an optimum thickness of photocatalyst film instead of optimum loading is determined according to the geometry of reactor. For the slurry reactors, optimum concentration of catalysts have been reported in a wide range from 0.15 to 8 g/l

depending on the specific set-up of photoreactors [33-37]. The effective penetration of light resulting from optimum loading is especially important for a slurry system. The maximum utilization is achieved by adjusting the best combination of illumination intensity and catalyst concentration.

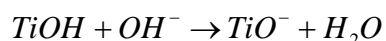
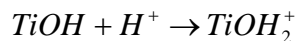
Light Intensity

Light absorption of the photocatalysts strongly affects the photocatalytic degradation rate since it is the first step of photocatalysis [38]. Generally, the degradation rate of organic compounds increases with the illumination intensity during a photocatalysis process. However, the nature of incident light does not alter the reaction pathway of photocatalysis [39]. In other words, there is no direct relationship between the electron-hole excitation mechanism and decomposition of organic species during photocatalysis.

Although photon flux is proportional to degradation rate, there are two regimes of decomposition process which could be classified with respect to light intensity. One is a first-order reaction at low light intensities, especially laboratory scale (usually up to $\sim 25 \text{ mW/cm}^2$). The other is a half-order reaction for even higher intensity. The reason why these two regimes occur is related to the recombination process in photocatalysis. Recombination is limited by the electrochemical reaction for the former case, but it becomes dominate by the photocatalytic reaction in the latter case.

pH

The behavior of metal oxide particles in water is well known to be amphoteric [40-42]. The surface of TiO_2 particles can be protonated or deprotonated under acidic or alkaline condition respectively. The basic mechanisms were described in the following reactions:



Therefore, the titania surface can be either positively or negatively charged depending on the pH value of aqueous solution. There are two aspects of the influence of surface charges at titania surfaces. One is the degree of dispersion for particles in water. Measuring the magnitude of the zeta potential is a common way to evaluate the stability of colloidal suspension. Generally, a value of more than 25 mV or less than -25 mV for zeta potential will be taken as a stabilized system [40-44]. Another important parameter with respect to surface charge is the isoelectric point (IEP). IEP is the pH value of slurry with zero surface charge. For example, the IEP of Degussa P25 was reported to be 6.5-6.7 [17,45]. Thus, better dispersibility of a P25 aqueous suspension could be achieved by adjusting the pH value to higher or lower than 6.5. Surface charges of titania surfaces also strongly affected the adsorption of organic species which is a crucial step for photocatalysis. In short, cationic molecules will be favored for the photocatalysis system with higher pH ($>$ IEP) and anionic molecules will be favored at lower pH ($<$ IEP).

Temperature

Temperature rise usually occurred in the system during photocatalytic reaction due to when the high intensity of illumination unless appropriate cooling system is used. An increase in temperature tends to intensify the recombination of electron-hole pairs and promotes desorption of the organic species at the titania surface [45-49]. Therefore, the temperature of a given photocatalysis system must be monitored and maintained in order to achieve optimum performance.

Oxygen Pressure

Dissolved oxygen plays an important role in photocatalytic reaction. The molecular oxygen is electrophilic and thus captures the photogenerated electrons to prevent unfavorable recombination [50-53]. Furthermore, it also generated some active species such as superoxygens and may involve in the photocatalytic reaction to enhance the mineralization rate of organic

pollutant in water; it helps to maintain the stoichiometry of titanium dioxide during photocatalysis as well. These effects have been extensively studied, and will be listed in the following sections.

Charge separation

It was found that dissolved oxygen not only trap the photoassisted electrons but also capture the holes [31,54]. In other words, the present of molecular oxygen in water tend to suppress the undesired recombination. Researchers design two experiments to demonstrate that [55]. They record the EPR spectra of titania photocatalysis with and without the present of dissolved oxygen. In the latter case, the number of trapped holes was proportional to the oxygen pressure in water. The results illustrate the relationship between photogenerated holes and dissolved oxygen molecules. In these experiments, oxygen is supplied to the system by aeration with ambient air.

Generation of active species

Depending on the number of electron reduction by dissolved oxygen, superoxygen ions or hydrogen peroxide are the two main products [17,56,57]. Some researchers suggest that electron trapping by dissolved oxygen may be the rate-limiting step in semiconductor photocatalysis [58-60]. Figure 2-3 summarized the formation of active oxygen species in the secondary reactions [17]. It is worthy to note that both superoxygen ions and hydrogen peroxide help to accelerate the photocatalytic reaction.

Maintenance of the stoichiometry of titania

Because of oxygen consuming during photocatalysis, the oxygen depletion leads to reduction of stoichiometry of TiO_2 and thus the photocatalytic ability [61-65]. Muggli et al. designed an experiment of photocatalysis of formic acid and acetic acid under inert gas atmosphere [62,63]. The results showed the rapid deactivation of photocatalysis and then fast

recovery of photocatalytic activity after providing the system with oxygen again. Based on this experiment, they suggested that the oxygen in the titania lattice is gradually lost during the photocatalytic reaction and could be compensated by aeration process.

Enhanced of Photocatalysis

Titanium dioxide can be only excited by the UV light irradiation since it is a wide band gap material (3.0 or 3.2 eV for rutile or anatase phase respectively). However, the UV range is only about 3% of the solar spectrum. There are two pathways for improving the photocatalytic efficiency of TiO₂: (1) enhancing the photoabsorption in the near-UV region [66] and (2) shift the absorption threshold towards visible light region [66-69]. To enhance photoabsorption, researchers have found that the enhanced photodegradation rate of organic species was achieved by using TiO₂ nanoparticles under UV light irradiation. This method is relatively cost and energy intensive since the photochemical reaction has to be generated by a UV lamp. On the other hand, extending the photoresponse to the visible light range will enable the materials to better utilize the abundant and free solar energy. For this purpose, many attempts have been made by incorporating another semiconductor material or by dye sensitization. Nevertheless, the short-term stability, low interparticle electron transfer rate, and low photocorrosion resistance have been difficult to overcome.

Size Reduction

During the last decade, the interest in the semiconductor nanoparticles originated from their unique physical and chemical properties [70]. One of the advantages of using nanoscaled photocatalysts is the extension of the effective band gap due to the quantum confinement effects. When the particles size becomes smaller or comparable to the wavelength of electron (the DeBroglie wavelength), the charge carriers will be constrained within a potential well [71,72]. And the bands of the semiconductor will split into several discrete electronic states (quantized

level) in the valence and conduction bands [73,74]. The other benefit of using nanomaterials is the enhanced photocatalytic activity due to the high surface/volume ratio [32]. Many researchers investigated the role of particle size in titania photocatalysis [71,75-77]. Some of them claimed that nanoparticles possess higher photoactivities than bulk materials. The other observed the opposite trend of reducing size on photocatalytic reaction rate [78,79]. The possible explaining of that could be attributed to the competition between the positive factor (i.e. interfacial charge transfer) and the negative factor (i.e. surface recombination) for photocatalysis. When the size of titania particles falls below a certain level, surface recombination starts to overcome the fast interfacial charge transfer due to the short diffusion path of charge carriers in nanoparticles.

Shape Control

Recently, nanoscale functional materials, especially low-dimensional inorganic semiconductor materials have attracted great interest because of their size-dependent optical and electronic properties and potential applications in nanoscale electronics and photonics. Therefore, there has been great interest in these kinds of materials. Research has been focused on the morphology control, such as synthesis of nanotubes [52], nanowires [80,81], nanoribbons [35], diskettes [82], nanobelts, nanosaws, nanowalls, nanomultipods, nanorings, nanocages, nanohelices, nanopropellers, and many others [83-85]. While one-dimensional nanowires and nanorods have been extensively studied, two-dimensional (2D) nanostructured materials have attracted much less attention until recently. However, 2D nanomaterials show strong potential as chemical and biological sensors, nanoelectronic devices, and catalysts with high surface areas and large pore volumes. Great interest in nanostructured materials have been focused on controlling the shapes of materials and finding novel properties [86]. The preparation of nanoscale photocatalysts is also of great interest, because nanomaterials offer a high surface-to-volume ratio and short distance from the bulk material to the surface [32]. Many small band gap

materials such as ZnO, ZnS, and Bi₂WO₆ with flake-like or plate-like morphologies have been already synthesized successfully [87-89]. For example, Ye *et al.* indicated that thinner ZnO nanoplates had higher photocatalytic activity [90]. Although the above materials possess visible light absorption, the relatively expensive precursors hinder practical application.

Since titanium dioxide is a versatile and low cost material in many industrial applications, many scientific works have been focused on particle size control down to the order of tens of nanometers. Quantization effects result in a shift in the absorption edges to longer wavelengths (blue shift) of absorption and therefore the UV light absorption is enhanced [42,71,91]. Except for size control, shape control of particulates, especially on a nanometer scale, is more difficult and receives less attention. The most common shape of the fine titanium dioxide particles is spherical in many processes. Thin films or fibers have been fabricated by being supported on a substrate or in the interstices in some three-dimension network [92]. However, the practical application is limited by the complexity and cost of the synthesis process. Sasaki fabricated thin titania flakes through exfoliation of a layered precursor [93]. Although the specific surface area of the flakes is about 110 m²/g, the photocatalytic activity is still less than commercial product, Degussa P25 (49 m²/g). Li *et al.* in 2007 synthesized Brookite phase titania nanoplates by using titanium trichloride (TiCl₃) precursor through hydrothermal processes [94]. Under the same surface area of loaded TiO₂, the brookite nanoplates exhibit the highest efficiency in the bleaching of methyl orange solution under UV irradiation. Therefore, this research is focused on the effect of shape on photocatalysis with titania.

Using TiO₂ nanoparticles for water treatment is limited in practical application since it is very difficult to remove these ultrafine particles due to very small mass. Therefore, the conventional separation methods such as centrifuging, filtration, and sedimentation are difficult

and expensive to implement. In addition, the efficiency of photodegradation by using nanoparticles is not very high because of the poor accessibility of the organic pollutants to catalyst surface caused by the agglomeration of particles [95]. However, synthesizing larger flake-like titania with nanosized thickness will alleviate this problem. These titania flakes can be easily separated from the treated water by simply filtration or sedimentation. Because the flakes are nano thin, superior photocatalytic properties are retained due to high surface to volume ratios and short diffusion paths, which are favorable for the migration of electrons and holes. This reduces the probability of the recombination of photogenerated electrons and holes. At the same time, the common agglomeration problem caused by nanoparticles can also be mitigated and therefore maintain the advantages of micro and nanostructure.

Doping (Narrowing Band Gap)

The most abundant energy source on earth is the solar energy which is mostly in the visible and near-infrared ranges with a very small part of UV. The incoming solar irradiation at the upper earth surface is 174 petawatts and about half of them will be reflected back to the space. Despite of that, one hour sun light irradiation was still more than the energy consuming of entire human being for one year according to 2002 statistics. Unfortunately, titanium dioxide can only absorb the UV light which is the small portion of solar energy due to the large band gap (Figure 2-4) [72]. Therefore, there is a need to develop the smaller band gap of photocatalysts associated with high visible light activities in order to utilize a greater portion of solar spectrum.

Nonmetallic doping in titania is one of the effective methods to narrow the band gap of the photocatalyst. In 2001, Asahi et al. reported that nitrogen-doped titanium dioxide showed photoresponse at wavelengths longer than 400nm [96]. They found that nitrogen atoms substituted the oxygen atoms in the TiO_2 lattices and narrowed the band gap by mixing the N 2p and O 2p states. After that, the synthesis of titanium dioxide with high photoactivity under

visible light was attempted by doping different nonmetallic ions (S, N, C, P ions etc.) into TiO₂ [67,96-99]. However, the nonmetallic doping methods usually required either complicated equipments or extreme process conditions such as high temperature, high pressure or poisoned dopant sources and therefore were not a cost effective way to fabricate the visible light photocatalyst. Except for nonmetallic elements, doping titania with transition metal ions was found to cause the red shift of band gap and therefore was a promising way to produce visible photocatalysts. There were many different metal elements successfully doped into the lattice of TiO₂ such as vanadium, chromium, manganese, iron, copper, zirconium, and tungsten [100]. Figure 2-5 shows the schematic representation of energy levels of several dopant ions in TiO₂ [100]. Among these dopants, vanadium is the most frequently investigated candidate elements because of its promising red shift ability, comparable ion radius of titanium and outstanding catalytic ability of titania-vanadia composite. Anpo *et al.* demonstrated the doping effect on red shift of photocatalyst absorption edge as the following sequence: V > Cr > Mn > Fe > Ni by bombarding ion beams into titania lattice [101,102]. Several approaches have been used to fabricate titania-vanadia mixed photocatalyst such as co-precipitation [103], ion-implantation [104,105], liquid phase deposition [106], wet impregnation [107], and sol-gel [108]. The sol-gel process provides a new approach for the synthesis of novel nanomaterials. Starting from molecular precursors, a three-dimensional oxide network is formed by hydrolysis and polymerized reaction. These reactions occur in solution and are usually termed sol-gel processing which is used to describe the preparation of inorganic oxide by wet chemistry routes. Furthermore, the incorporation with metal ions occurs in the sol-gel formation step which provides better homogeneity and feasible control of the final product shape. Therefore, unique catalytic properties could be expected using this technique. Wu *et al.* developed two modified

sol-gel methods for synthesis of series vanadium doped titania samples with pertained anatase phase after 400 °C heat treatment [108]. Kiosek *et al.* investigated the photocatalysis process of ethanol on titania-vanadia mixed catalysts under visible light using ^{13}C NMR method and found that the active species was V^{4+} instead of V^{5+} [109]. Zhao *et al.* synthesized vanadium doped titania photoelectrodes using sol-gel process and generated photocurrents under visible light irradiation [110]. So far, vanadium doping was proved to be an effective method to not only narrow the band gap of titania but also enhance the photocatalytic efficiency under visible light illumination. In this study, we utilized this method to produce visible light photocatalysts and investigated the doping effect of vanadium on the visible photocatalysis efficiency of vanadium doped titania nanoflakes.

Table 2-1. Bulk properties of three TiO₂ polymorphs [24].

	Rutile	Anatase	Brookite
Crystal structure	Tetragonal	Tetragonal	Orthorhombic
Space group	$D_{4h}^{14} - P_2^4 / mnm$	$D_{4h}^{19} - I_1^4 / amd$	$D_{2h}^{15} - Pbca$
Lattice constant (Å)	a = 4.584; c = 2.953	a = 3.733; c = 9.370	a = 5.436; b = 9.166; c = 5.135
Density (g/cm ³)	4.24	3.83	4.17
Electron mobility (cm ² /Vs)	1	10	—
Dielectric constant	6.62	6.04	7.89
Refractive index (np)	2.621	2.561	2.583
Band gap (eV)	3.0 (indirect)	3.2 (indirect)	—

Table 2-2. Oxidation power of species [26].

Species	Relative oxidation power
Hydroxyl radical	2.06
Singlet oxygen radical	1.78
Hydrogen peroxide	1.31
Perhydroxyl radical	1.25
Chlorine dioxide	1.15
Chlorine	1.00

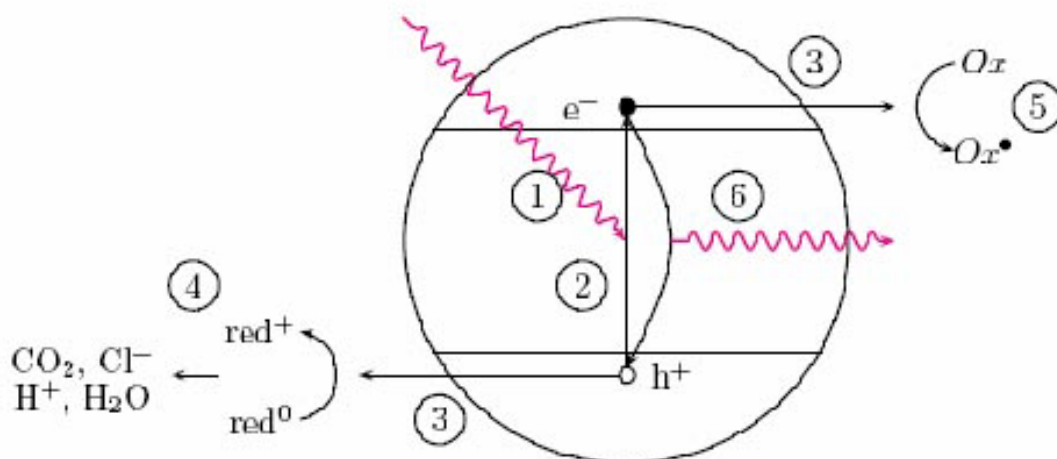


Figure 2-1. Schematic representation of the photoelectrochemical mechanism taking place inside titania: (1) light irradiate the semiconductor. (2) forming of electron-hole pair. (3) charge carriers migrate to the surface. (4) initiation of an oxidative pathway by a valence-band hole. (5) initiation of a reductive pathway by a conduction-band electron. (6) electron and hole recombination to heat or light.

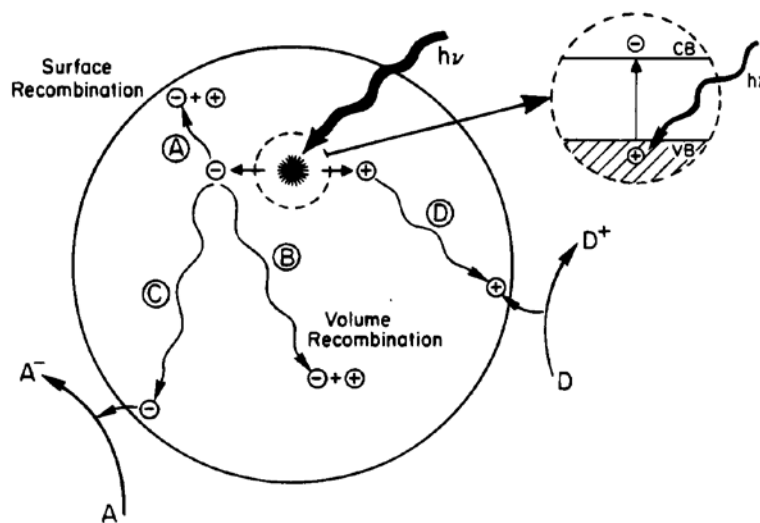


Figure 2-2. Schematic photoexcitation in a solid followed by deexcitation events [19].

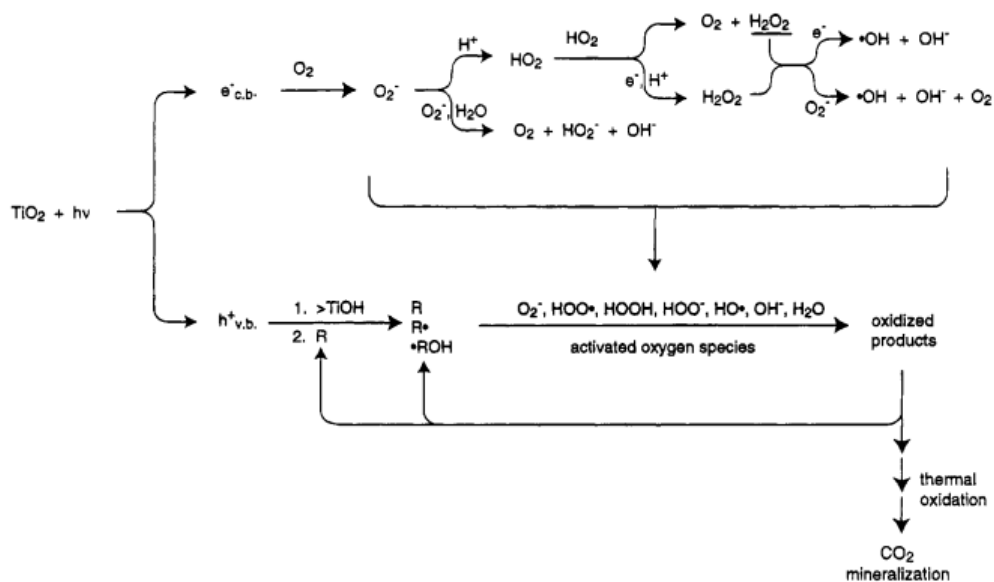


Figure 2-3. Secondary reactions with active oxygen species in the photoelectrochemical mechanism [17].

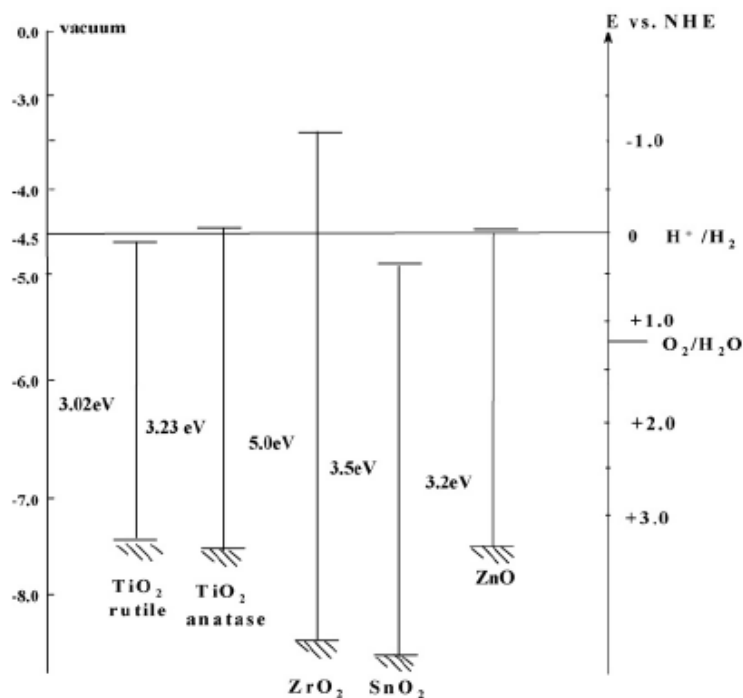


Figure 2-4. The schematic diagram of conduction and valence bands positions of several semiconductors. The left hand scale is the internal energies to the vacuum level and the right hand scale represented the comparison to normal hydrogen electrode (NHE) [72].

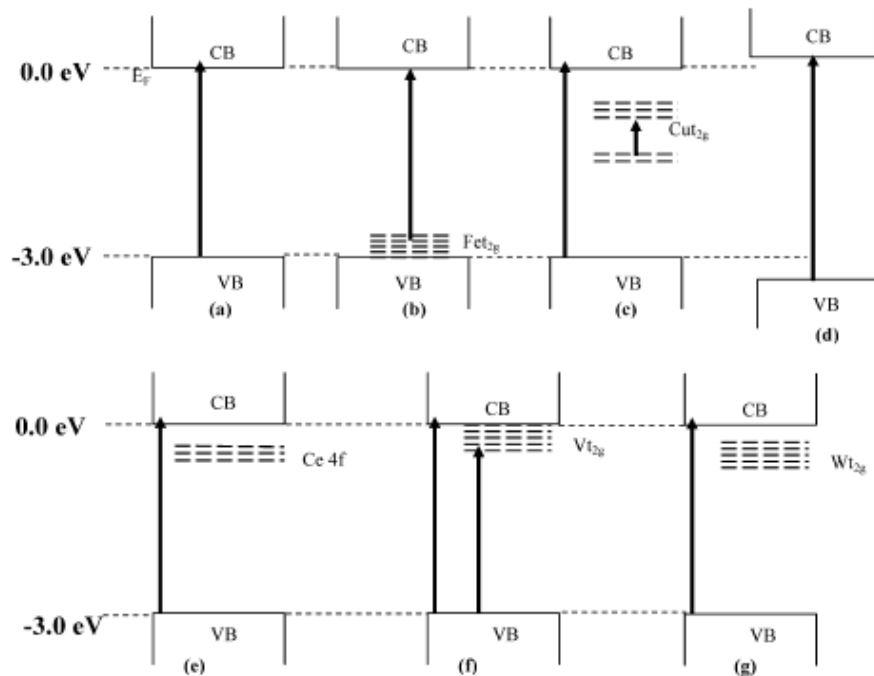


Figure 2-5. Schematic energy level diagram of metal doped TiO₂ (a) Pure TiO₂ (b) Iron doped (c) Copper doped (d) Zirconium doped (e) Cerium doped (f) Vanadium doped (g) Tungsten doped TiO₂ [100].

CHAPTER 3 HIGH ASPECT RATIO TITANIUM DIOXIDE FLAKES AS PHOTOCATALYSTS

Synthesis of High Aspect Ratio of TiO₂ Flakes

Titania nanoflakes were synthesized by a modified sol-gel method which was based on surface controlled hydrolysis of titania precursor on water surface. A mixed oil phase contained stearic acid (C₁₈H₃₆O₂), hydrocarbon and titanium tetraisopropoxide (Ti(OC₃H₇)₄) was delivered by spreading it on the surface of an aqueous phase which was consisted of high purity water (Barnstead Nanopure Infinity, 18MΩ/cm⁻¹), nitric acid (HNO₃), and sodium dodecyl sulfate (C₁₂H₂₅SO₄Na). Stearic acid and hydrocarbon were used to decrease the viscosity of titania precursor and enhance the spreading ability of the mixture. After spreading, a titania precursor film spontaneously hydrolyzed at the oil/water interface, leading to the formation of thin titanium dioxide flakes. The thickness of nanoflakes could be easily manipulated by varying the volume ratio of titania precursor and hydrocarbon. Typically, a 1:8 volume ratio of titania tetraisopropoxide to hydrocarbon was used to synthesize titania nanoflakes with thickness of about 40 nm. The resulting slurry was washed with Nanopure water and then centrifuged (Beckman JA-21 Centrifuge) at 3000 rpm for 15 minutes to concentrate the slurry. The above cleaning process was repeated five times to get rid of organic residuals. After solvent exchanging with isopropanol alcohol ((CH₃)₂CHOH), the nanoflakes were dried by a supercritical fluid drying process [111]. The following heat treatments were obtained by using a programmable electric furnace with desired heating rate. For convenience, we will call the non-heat treated and heat treated materials as synthesized and calcined flakes respectively.

Characterization of TiO₂ Flakes

When an appropriate amount of flakes are dispersed in water, significant visual pearlescence occurs when shaking the solution, a qualitative indication that particles in water are

flaky (Figure 3-1A and B). It is well known that titania is a high refractive index material within the visible light range, and therefore is commonly used as the basic pigment in paintings. When the larger side of flakes faced to the incident light, the strong reflection of light occurs at the surface of the particles and generates the luster effect. However, the luster is reduced when the incident light diffusely scattered by the edge of the flakes [112,113]. Alternative brightness and darkness occurred when flakes are randomly orientated in the solvent. This pearlescent effect does not occur in the P25 slurry owing to the isotropic shape of the particles (Figure 3-1C). The low magnification optical microscopic (OM) images of both flakes indicated flat particles with major dimension in micrometer range (Figure 3-2). The strong interference color observed under dark field microscopy indicates a thin minor dimension, confirmed by SEM to be in the 30-40 nanometer range.

The flakes were further characterized with Scanning Electron Microscopy (SEM), Laser Diffraction for particle size analysis, X-Ray Diffraction (XRD), Transmission Electron Microscopy (TEM), Physisorption Techniques, UV-Visible Spectrometer (UV-Vis), X-ray Photoelectron Spectroscopy (XPS), and Electrophoretic Mobility (Zeta Potential). The surface morphology of synthesized nanoflakes was investigated using SEM images, shown in Figure 3-3. The major diameter of the flakes was found to be of the order of 20-30 μm (Figure 3-3), and the thickness of these flakes was approximately 40 nm (Figure 3-4 A). The aspect ratio of major dimension to thickness ranged from 250:1 to 500:1. The flakes were further treated by calcination at 400 $^{\circ}\text{C}$ in air for 2 hours. Aggregation was not apparent when comparing these treated flakes with those obtained directly from synthesis. Moreover, the thickness of calcined flakes did not change by the heat treatment (Figure 3-4 B). A comparison of particle size distributions measured on the synthesized and calcined flakes is shown in Figure 3-5. Particle size distributions of synthesized and calcined flakes were measured using laser diffraction. When

we were using a differential volume distribution for flaky particles that moved in turbulence and passed the laser beam, the maximum diameter was measured through the average random orientation of the flakes. The larger dimension of nanoflakes were estimated by dispersing both flakes in deionized water with liquid modules and were fairly close to the results taken from the SEM images (Figure 3-3). The D_{10} , D_{50} , D_{90} , mean and standard deviation values for the particle size distributions are shown in Table 3-1. The synthesized material has a broad size distribution spanning from 1-100 μm with a D_{50} of 39.1 and 23.5 μm for the synthesized and calcined flakes respectively (Figure 3-5). Comparing the volume distributions, it is evident some larger flakes break or crack during dehydration and crystallization.

Crystalline structure changes of the titanium dioxide flakes were monitored by powder XRD (Figure 3-6). The synthesized flakes show broadening and weak Bragg peaks which indicates the nature of flakes consist of partially amorphous material with a presence of the anatase phase (Figure 3-6 A). After heat treatment, the expected phase transformation from amorphous to crystalline titanium dioxide was confirmed by seven characteristic diffraction peaks (Figure 3-6 B). The heat treated flakes were converted to a pure anatase phase [JCPDS: 21-1272] which is the most photoactive phase of titanium dioxide [16,17,72]. There is no indication of the rutile phase by XRD. The intensity of characteristics peaks is comparable to commercially available pure anatase standard materials (Figure 3-6 C) which indicate complete conversion of the amorphous titanium dioxide. The average crystal grain size can be calculated by the Scherer equation (equation 3-1):

$$d = \frac{k\lambda}{B \cos \theta_B} \dots\dots\dots(3-1)$$

where d is the calculated grain size, λ is the wavelength of X-ray (Cu $K\alpha$ 1.54 \AA), B is the full-width at half-maximum intensity, and θ_B is the Bragg diffraction angle. The grain size is

determined to be 4 and 9 nm for synthesized and calcined flakes respectively (Table 3-2). The photocatalytic activity of nanocrystallite titanium dioxide was shown to be strongly dependent on the grain size [114,115]. Generally, the enhancement of interfacial charge transfer rate occurs at smaller grain due to the decrease of volume recombination process and the increase of the surface area. However, the photocatalytic efficiency is not continuously increasing with decreasing grain size since surface recombination process tends to dominate the photocatalysis. Therefore, a critical size for optimum photocatalytic efficiency is about 10-15 nm has been reported by several researchers [114-116].

The crystalline structure of the flakes was further investigated under HR-TEM. The images show the flakes are comprised of circular crystalline platelets of about 5-8 nm in diameter (Figure 3-7). The interference lattice fringes can be seen in the TEM images and has a separation distance of 0.35 nm, corresponding to the interplanar spacing of the (101) planes for anatase [117]. Random orientation of individual grains over both flakes is suggested from the concentric diffraction rings in the select area diffraction mode and consistent with the anatase (101), (004), (200), (105) for circles 1 to 4 respectively (the insets of Figure 3-7). On closer inspection, an amorphous layer can be seen surrounding the smaller circular crystallites in synthesized sample (Figure 3-7 A). After calcination, pores developed due to local rearrangement and growth of crystal grains. Consequently, it is thought that the flakes are polycrystalline consisting of fine grains of anatase titanium dioxide.

Surface area and porosity measurements were performed to verify the changes in the structure of the titanium dioxide due to the calcination treatment. This was measured using nitrogen absorption isotherms in conjunction with the Brunauer-Emmett-Teller (BET) model. It is desirable for photocatalytic materials to have higher specific surface area as the reaction rate is proportional to the number of available surface sites. However, high surface area powders are

usually associated with large amounts of crystal defects favoring fast recombination of electrons and holes, ultimately leading to lower photoactivity. Compared to a commercial photocatalyst, Degussa P25, the surface areas of nanoflakes were 3-6 times higher (Table 3-3).

Except for specific surface area, the surface chemistry of titanium dioxide is another surface property which significantly affects the photocatalytic reaction. This study is mainly focused on the photocatalysis in water. Therefore, the interaction between titanium dioxide particles and water is an essential problem. It was well known that the chemistry of metal oxides surface is mainly dominated by the hydroxyl groups arise from the interaction with the environment such as moisture in atmosphere or water in aqueous solution [118,119]. Surface OH groups were determined by taking XPS spectra of O 1s signal for all of the samples under the same preparation condition. Using the Gaussian mixture peak fitting technique, two components are shown in the typical O 1s XPS spectrum (Figure 3-8 A). One represents the oxygen element in titania lattice (529.9 eV) and the other corresponds to the surface hydroxyl species (531.9 eV) [120]. The ratio of surface OH to total oxygen 1s signals for the samples is shown in Figure 3-8 B. It should be noted that both samples have higher surface hydroxyl concentration than commercial product, P25, on the same mass basis. Calcined flakes have less OH groups than synthesized samples due to the dehydroxylation process after heat treatment. It has been widely reported that the removal of surface absorbed water was carried out by annealing the sample at 450-500 °C [118,121]. Higher density of OH groups for synthesized and calcined flakes were attributed to the higher specific surface area comparing to the Degussa P25. Hydroxyl radical, one of the most reactive species in the photocatalysis process, is strongly related to the hydroxyl group concentration at titania surface. Therefore, we could expect that better photocatalytic performance could be achieved by the sample showing the larger OH component in the XPS oxygen 1s signal.

The photocatalytic activity of these flakes was investigated by performing dye degradation experiments under ultraviolet activation. Figure 3-9 A shows typical UV-visible diffuse reflectance spectra in the wavelength range of 250-500 nm for the synthesized flakes together with the calcined flakes. The sharp decrease in the diffuse reflectance in the UV region results from the fundamental light absorption of the titanium dioxides flakes and a blue shift of the onset of reflectance occurred at calcined sample due to heat treatment. In semiconductor physics, the general relation between the absorption coefficient and the band gap energy is given by

$$(\alpha h \nu)^m = h \nu - E_g \dots\dots\dots(3-2)$$

where m is an index depending on the nature of the electron transitions, α is the absorption coefficient, h is the Planck constant, ν is the frequency of electromagnetic radiation, and E_g is band gap energy of the semiconductor. To estimate band gap energies of both nanoflakes, α data in Figure 3-9 B is plotted as $(\alpha h \nu)^2$ versus $h \nu$ and the optical absorption energy is determined via extrapolation. An increase in band gap from 3.25 to 3.33 eV, i.e. a blue shift, is mostly likely due to the quantum confinement effect of higher crystallinity after calcination and thin flaky morphology [117]. Kim *et. al* suggested that the differences in atomic structure between the grain boundary and the amorphous area potentially leads to larger concentrations of electrons and holes as well as the existence of potential barriers at these interfaces [122]. Hence it is possible for an electric field to be generated, the band gap energy to increase, and the absorption limit shift to a narrower wavelength range. It is important, but also difficult to measure the fraction of light absorbed in the TiO₂ suspensions due to the inevitable scattering effect. In this study, a modified method based on the use of the integrating sphere was used to evaluate the “true absorbance” in the titania slurries [123]. The schematic of assembling integrating sphere in this method is shown in Figure 3-10. The fundamental principle of this method is described as

the followings: First of all, the reference solution (for example, water) was placed between the incident beam and reflection plate which consisted of fine barium sulfate particles (Figure 3-10(a)). The absorbance of the standard could be calculated by equation 3-3.

$$A_R = -\log\left(\frac{I_0 - 2I_a}{I_0}\right) \dots\dots\dots(3-3)$$

Where A_R is the instrumental reading, I_a is the light flux absorbed by the reference solution, and the coefficient “2” comes from the incident beam pass through the cell and back scatter again. When the titania samples were put in the same position of reference solution (Figure 3-10(b)), the instrumental reading could be described as equation 3-4.

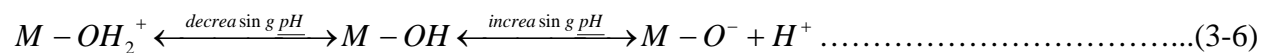
$$A_s = -\log\left(\frac{I_0 - 2I_a - 2I_{sa}}{I_0}\right) \dots\dots\dots(3-4)$$

Where A_s is the instrumental reading of titania sample, I_{sa} is the photon flux absorbed by titania particles in water. According to these two equation, the “true absorbance” of titania particles is a function of the ratio of I_{sa} to I_a and could be expressed by equation 3-5.

$$A = -\log\left(1 - \frac{I_{sa}}{I_a}\right) = -\log\left(1 - \frac{10^{-A_R} - 10^{-A_s}}{2}\right) \dots\dots\dots(3-5)$$

Figure 3-11 shows the comparison of the true absorbance for three different titania samples using the modified method on the same mass basis. Calcined titania flakes have the highest optical absorption within the wavelength range from 250 to 350 nm. The synthesized titania flakes have similar absorbance on the shorter wavelength (250-300 nm) regime compared to P25. The higher photon flux absorbed by titania sample implied that more active species generated during the photocatalytic process and thus higher quantum yield could be achieved.

The surface charges of a metal oxide surface within an aqueous solution are highly affected by the dissociation of the surface hydroxyl groups [118,121]. The equilibrium of an oxide in water could be expressed by equation 3-6.



The above equation indicated that the surface of metal oxide may carry either positive or negative charges according to the pH of the solution. In terms of the chemical structure of the methylene blue, it is a cationic dye and therefore adsorbed preferentially at the negatively charged surface [124]. The pH of 50 μM of methylene blue solution was determined to be about 6.6-6.7 using the pH meter. In order to evaluate the surface charge of the titania samples, the electrophoretic mobility of the particles were measured to determine the zeta potential of the surface (Brookhaven Zetaplus Zeta Potential Analyzer). Zeta potential of the titania samples as the function of solution pH is plotted in Figure 3-12 and the isoelectric points (IEP) are listed in Table 3-4. The IEPs were estimated to be 5.8, 5.1, 5.0 for P25, synthesized and calcined titania flakes respectively. Both titania flakes have lower IEPs than P25 nanoparticles owing to the higher concentration of surface hydroxyl groups (Figure 3-8 B). It was well known that the surface charge of the particles is very sensitive to the surface density of OH group especially in the aqueous solution. It is noteworthy that the IEP of the flakes is not severely shifted after heat treatment which implies that there is no difference in the nature of the surface hydroxyl group between both flakes. However, the lower magnitude of the surface charge at the same pH value for calcined flakes was due to the dehydroxylation process during heat treatment. The surface charges of both flakes at pH= 6.6 were higher than that of P25 (Table 3-3) and indicated the more favorable adsorption of methylene blue molecules at the surface of the both flakes.

Therefore, higher photocatalytic performance of the flakes could be expected due to the stronger surface adsorption of the methylene blue molecules.

Benchmark: Degussa® P25

Degussa® P25 is a commercial titanium dioxide nanoparticles synthesized by using a high temperature flame pyrolysis process with titanium chloride precursor. The primary particle size is 30 nm under TEM investigation [125]. It is a mixed phase material which contains anatase and rutile phases in a ratio of 3:1. However, rutile particles exist separately from larger anatase particles instead of covering the surface of P25 nanoparticle as surface layer. The specific surface area is relatively high, $\sim 50 \text{ m}^2/\text{g}$ (Table 3-3). Because of its high activity for many kinds of different photocatalytic reactions, it was used as the benchmark for activity comparison. Researchers summarized the reasons why P25 showed high photocatalytic efficiency for two points: (1) slow recombination due to stable charge separation by electron transfer between the mixed two phases (2) the smaller band gap of rutile phase (3.0 eV) extend the photoresponse to the visible light region [125,126].

Experiment Apparatus

Dye decomposition experiments were performed inside a cylinder UV reactor equipped with 6 UVA lamps (Southern New England Ultra Violet Company, Branfield, CT). A 150ml Erlenmeyer flask contained dye solution with TiO_2 particles were placed inside the UV reactor and continuously agitated by a magnetic stir. House air was delivered by a glass tip connected to the plastics hoods from air outlet for investigating the aeration process. The amount/volume of input air flow was controlled by a flow meter. A cold air flow generated by a cooling fan circulated through the cylinder UV reactor was to prevent the heating effect during the photocatalysis process. 100 ml of dye solution with concentration of $50 \mu\text{M}$ were prepared. Three photocatalysts were added to the dye solution respectively and then stirred for 10 minutes

in the dark before UV light illuminating. Prior to turn on the UV light, about 2 ml of dye solution was pipetted out and stored in a plastic vial. After starting the photocatalytic process, the same amounts of samples were taken by every 15 minutes for decoloration study. For avoiding the artificiality caused by reflection of titania dioxide particles during the UV-Visible spectrometer study, each collected sample were centrifuged at 10000 g three times to settle down the particles. Then the centrifuged sample was carefully transferred into a double sided cuvette without breaking the bottom titania cakes.

Photocatalytic Degradation of Dye Molecules under UVA Light Illumination

The photocatalytic activity of titanium dioxide nanoflakes were probed by decomposition of methylene blue solutions. Degussa P25, one of the most efficient photocatalysts was used as benchmark for comparison. The UV-Visible spectra were obtained to evaluate the photocatalytic degradation of dye solution. Figure 3-13 is a typical methylene blue dye absorbance spectra resulting from 2 hours photocatalysis with synthesized titania flakes. The maximum absorption wavelength (λ_m) of methylene blue, 662 nm, was chosen for calculation the decomposition rate of dye solution under photocatalytic process.

Figure 3-14 compares the photocatalytic activity of P25, synthesized and calcined titanium dioxide nanoflakes by removing the methylene blue from water under UV light irradiation. Degussa P25 was used as a reference material. It has a mean diameter of 30 ~ 40 nm which is comparable to the minor dimension of nanoflakes (40 nm). It was observed that calcined flakes exhibited the highest photocatalytic efficiency on the degradation of methylene blue among all tested samples. A first order rate reaction showing in Figure 3-14 A indicates that dye concentration is the limiting factor. In contrast, significant enhancement is observed when introducing air bubbles into the system continuously (Figure 3-14 B). It was well known that surface adsorption of organic species is very crucial to the titania photocatalysis. The whole

photocatalysis process could be separated by several parts. First, organic molecules need to be adsorbed at the available sites of titania surface. Then the UV light strikes the titania particles which generate an electron-hole pair. The charge carriers diffuse to the surface and form either hydroxyl radicals or super oxide ions. Finally, the adsorbed molecules contact the above strong reductants or oxidants and then photocatalysis occurs. It has been demonstrated experimentally by several researchers that dye degradation rate of UV/TiO₂ photocatalysis follows a pseudo first order expressed by the Langmuir-Hinshelwood (L-H) mechanism [16,20,127-131]. Therefore, this model will be used to analyze and calculate the kinetics of dye degradation with photocatalysis in this study. In the L-H model, the reaction rate is proportional to the surface coverage θ which becomes proportional to the concentration C at low concentrations range and could be written as equation 3-6.

$$r = k\theta = k \frac{KC}{1 + KC} \approx kKC = k_{pseudo}C = \frac{-dC}{dt} \dots\dots\dots(3-6)$$

Where r is the reaction rate, k is the kinetics constant, K is the absorption constant, C is the concentration of dye solution and k_{pseudo} is the pseudo first order constant. The linear transform of degradation curve is plotted as $-\ln(C/C_0)$ versus irradiation time and the rate constants are calculated from the slopes of Figure 3-15. The rate constants are shown in Table 3-5. The reaction with added turbulence present a pseudo first order reaction and much higher efficiency especially for the flake systems. One possible explanation of these differences may be correlated to oxygen depletion during the photocatalysis process. From the results of XRD and TEM, both flakes consisted of very small nanocrystallites which imply a large number of defects (grain boundaries) within both materials. Consequently, fast recombination of photoassisted charge carriers preferentially occurs at these local defect sites and dominates the reaction. The photocatalytic performance is not proportional to surface area without supplying oxygen to the

system. By introducing air into the system, dissolved oxygen will primarily become an electron acceptor and may form superoxide radicals [132]. More importantly, fast recombination, the rate limiting step, could be depressed by eliminating excited conduction band electron for higher efficiency.

Statistical Design of Experiments

There are several possible parameters that affect the heterogeneous photocatalysis of this system such as light wavelength, light intensity, irradiation time, catalyst loading, target pollution concentration, pH, reactor geometry, and dissolved oxygen concentration [45]. It is impossible to systematically study all of the parameters in limited time. However, from the preliminary experiments (Figure 3-14), light intensity, catalyst loading and aeration rate were determined to significantly affect the photocatalytic efficiency. Therefore, a statistical design of experiments was performed addressing these three parameters by using the Design Expert “7” software. There are at least three advantages for doing so. First, the interaction between multiple parameters could be easily investigated by limited experiments. It saves time, cost, and materials. Second, the experiment error could be separated from results leading to more accurate evaluation of these parameters. Third, fewer experiments are needed to obtain statistically relevant results. More importantly, this method allows the researcher to generate mathematical models and map the experimental space by identifying which variables are significant and fitting the data to the developed model. The optimized response is identified by using the developed model leading to the conditions necessary to achieve the highest performance.

The parameters investigated in the design of experiments were A: bubbling flow rate (cubic feet per hour), B: mass concentration of photocatalysts (ppm), and C: Ultraviolet light intensity (number of lamps). A full 2^3 factorial design with three center points was used to obtain the developed model and estimate the experiment error. The detail of design of experiments is

shown in Table 3-6. This statistical design was performed for three different materials as listed in the preliminary results for further comparison. The results for three photocatalysts are outlined in the following sections.

Synthesized Flakes

The results for the synthesized flakes are shown as a 3D representation of design space (Figure 3-16). Three experiment variables are presented on each side of the cube respectively and each corner indicated one point in the design matrix. The dye degradation% obtained by synthesized flakes photocatalysis is pointed out as the number located at each corner inside the cube. The best results for synthesized flakes could be seen using high level of light intensity, catalyst loading, and flow rate. However, the complete degradation of dye molecules within 2 hours is not found in the whole range of design points (Figure 3-16). A developed model expressed by the equation 3-7 was developed by the software.

$$\text{Dye degradation\%} = 42.45 + 5.63A (\text{Flow rate}) + 17.48B (\text{Catalyst loading}) + 10.32C (\text{Light intensity}) + 5.30AB + 8.25BC \dots \dots \dots (3-7)$$

The significant factors for dye degradation with synthesized flakes are shown in equation 3-7 with the magnitude of their effect. The mathematical equation indicates that light intensity and mass concentration of catalysts have the largest effect on photocatalytic efficiency. There were some small interactions between these factors and the model did not include the AC (Flow rate * Light intensity) interaction because it was insignificant compared to the decomposition%. It is reasonable that these two factors are controlled by individual devices (i.e. flow meter and UV lamps) and there are not any intrinsic effects between these two factors on the photocatalytic efficiency.

The surface response plots, the contour lines of the constant response and interaction curves are constructed to give the graphical representations of the decomposition% as a function

of two factors when the third factor is fixed. The surface response of factor A and B under different intensity of light are shown in Figure 3-17. These curves show that there is only limited benefit on degradation rate at low concentration of catalyst no matter how high the flow rate is. However, the dramatic increase occurs when increasing the amount of photocatalysts. The results indicate that there were not enough active species (or photocatalyst) to oxidize the organic pollutants and therefore increasing bubbling rate did not speed up the photocatalytic reaction. Moreover, the aeration process further improved the overall efficiency only with moderate to high catalyst concentration (Figure 3-17 B and C). The 2D contour lines of response data and interaction plots are shown in Figure 3-18 and 3-19 for two levels of light intensity (C = 2 and 6 lamps) respectively. The curvature of these contour lines suggests interactions between factors A and B (Figure 3-18 A). Both the interaction plots show similar trends: degradation efficiency increases by increasing the amount of catalyst and bubbling rate further increases the efficiency especially for higher loadings of titania (Figure 3-18 B and 3-19 B). It is worthy to note that increasing mass of catalyst did not improve the efficiency at low light intensity and flow rate, presumably due to insufficient photons activating the reaction at the excess available surface area (Figure 3-18 B). Figure 3-20 shows the 3D surface response of decomposition% as the function of factor B and C. It is apparent that the interactions between these two parameters are significantly stronger than the AB interaction (Figure 3-17) especially for high level of both factors. This result is also confirmed by the magnitude of BC term in equation 3-7. There is only minor enhancement on reaction rate when increasing the light intensity at low catalyst loading. In contrast, the increase in the amount of photocatalyst largely improved the efficiency without changing the intensity of light. This is consistent with both the experimental observation (equation 3-7) and fundamental theory: the photocatalyst is the most significant factor in the photocatalysis reaction. Figure 3-21 and 3-22 show both the contour lines and interaction plots as the function

of B and C for two levels of flow rate (A = 0 and 10) respectively. When fixing the flow rate, the BC (catalyst loading* light intensity) interaction shows the same trend but stronger interaction. The 3D surface response of factor A and B shows an incremental trend for both factors and similar trend also presents in response of factor B and C (Figure 3-19). The maximum degradation%, 86.7%, could be predicted using the developed model and further proved by experiment. The full ANOVA analysis is listed in Appendix A.

Calcined Flakes

The cube plot of calcined flakes photocatalysis is shown in Figure 3-23. The complete degradation of dye indicates that calcined flakes have higher photocatalytic activity than synthesized flakes and P25. The software generated model for calcined flakes is described by equation 3-8.

$$\text{Dye degradation\%} = 62.10 + 2.18A (\text{Flow rate}) + 14.55B (\text{Catalyst loading}) + 16.85C (\text{Light intensity}) + 1.07AB + 3.30BC \dots \dots \dots (3-8)$$

The most significant factors are the mass concentration of catalysts and light intensity for calcined flakes. Again there is no AC interaction owing to the nature of these two parameters.

Figure 3-24 shows the surface response as the function of factor A and B. There is a dramatic increase at constant light intensity when adding more catalysts into the system. Aeration process did not improve the efficiency at low catalyst concentration (50ppm), but helped to enhance the reaction rate when higher amount of photocatalyst presented in the system (Figure 3-25 and 3-26). It is worthy to note that there is an enhancement of catalyst loading on overall efficiency for calcined flakes under weak illumination compared to no apparent effect for synthesized sample under the same condition (comparing Figure 3-18 B and 3-25 B). When the 3D response plot is considered as the function of factor B and C, factor C (light intensity) is the most significant factor and the strong interaction is shown in the Figure 3-27. It is more obvious

in the contour and interaction plot (Figure 3-28 and 3-29). These results suggested that current light source was not enough for the excess surface area of calcined flakes. Therefore, the number or intensity of photon flux is the limiting factor for photocatalysis with calcined flakes in this case. Back to the characterization part, we know that calcined flakes have good crystallinity, high specific surface area, appropriate grain size and higher light absorption ability which implied high photocatalytic activity. From both characteristics and experiment design aspects, we could conclude that the calcined flakes are the most efficient materials for photocatalysis in this study.

P25

The maximum decomposition% of P25 was slightly higher than synthesized flakes under the same condition. Complete degradation of dye molecules was not achieved using Degussa P25 as photo-mediated agent in the current design of experiment (Figure 3-30). Factor C is again the most significant factor and weaker interactions also present in the computer developed model equation 3-9.

$$\text{Dye degradation\%} = 50.10 + 2.08A (\text{Flow rate}) + 14.15B (\text{Catalyst loading}) + 19.03C (\text{Light intensity}) + 2.02AB + 0.77BC \dots \dots \dots (3-9)$$

The similar trends respect to calcined sample are shown when the surface responses are plotted as the function of AB and BC for P25 (Figure 3-31 and 3-32). It is worthy to note that there is a very weak interaction between factor B and C compared to both flakes (equation 3-9). It is more apparent when the parallel lines presented in the interaction plots under the constant flow rate (Figure 3-33). The results suggested that the amount of catalyst is the limiting factor for photocatalysis. In order to achieve higher efficiency, we need to increase the amount of P25 instead of adding more lamps.

Table 3-1. Particle diameter statistics for synthesized and calcined flakes.

Sample	D ₁₀ (μm)	D ₅₀ (μm)	D ₉₀ (μm)	Median (μm)	Standard Deviation (μm)
Synthesized flakes	5.2	39.1	81.6	20.8	58.9
Calcined flakes	5.1	23.5	50.1	18.4	18.8

Table 3-2. Grain size calculation by the Scherer equation for both nanoflakes.

Sample	B (degree)	θ_B (degree)	d (nm)
Synthesized flakes	2.72	25.91	4.1
Calcined flakes	0.93	25.35	8.7

Table 3-3. Physisorption measurements of P25, synthesized and calcined titania nanoflakes.

Sample	Specific surface area (m^2/g)	Specific pore volume (cm^3/g)	Average pore diameter (nm)
Synthesized flakes	323	—	—
Calcined flakes	151	0.511	7.2
P25	49	—	—

Table 3-4. Optical and electrostatic properties of titania samples.

Sample	Band gap energy (eV)	IEP	Surface charge at pH= 6.7 (mV)
Synthesized flakes	3.25	5.1	17.9
Calcined flakes	3.33	5.0	12.7
P25	—	5.8	7.5

Table 3-5. Pseudo-first order rate constants of methylene blue under photocatalytic degradation.

Without bubbling treatment		With bubbling treatment	
Sample	k_{pseudo} (10^{-3} min^{-1})	Sample	k_{pseudo} (10^{-3} min^{-1})
Synthesized flakes	1.0	Synthesized flakes	10.0
Calcined flakes	3.8	Calcined flakes	32.5
P25	2.0	P25	11.9

Table 3-6. The 2³ factorial design used to investigate the most important factors for UV light photocatalysis.

Factor 1 A: Light intensity (number of lamps)	Factor 2 B: Catalyst loading (ppm)	Factor 3 C: Bubbling flow rate (ft ³ /hour)
- (2)	- (50)	- (0)
+ (6)	- (50)	- (0)
- (2)	+ (100)	- (0)
+ (6)	+ (100)	- (0)
- (2)	- (50)	+ (10)
+ (6)	- (50)	+ (10)
- (2)	+ (100)	+ (10)
+ (6)	+ (100)	+ (10)

*Center point: A (flow rate): 5; B (catalyst loading): 75; C (light intensity): 4

A **B** **C**

Figure 3-1. Photographs of titania slurries. A) synthesized flakes. B) calcined flakes. C) P25 on the same mass basis (note the pearlescence of the samples).

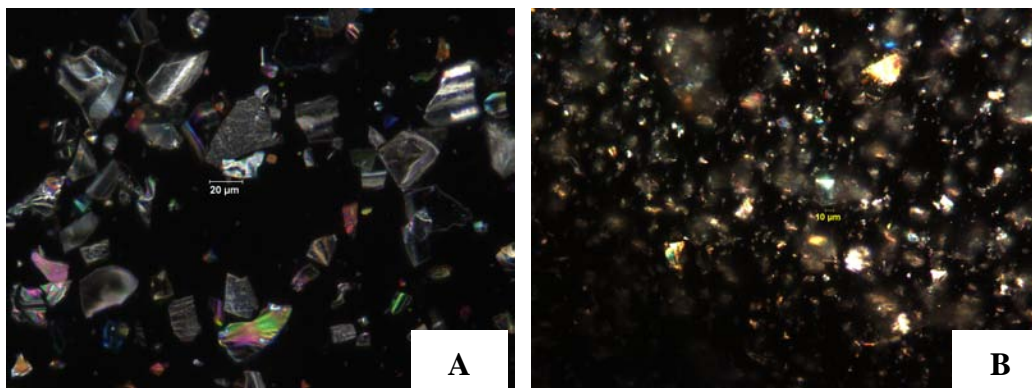


Figure 3-2. Optical micrographs of titania samples. A) synthesized flakes. B) calcined flakes.

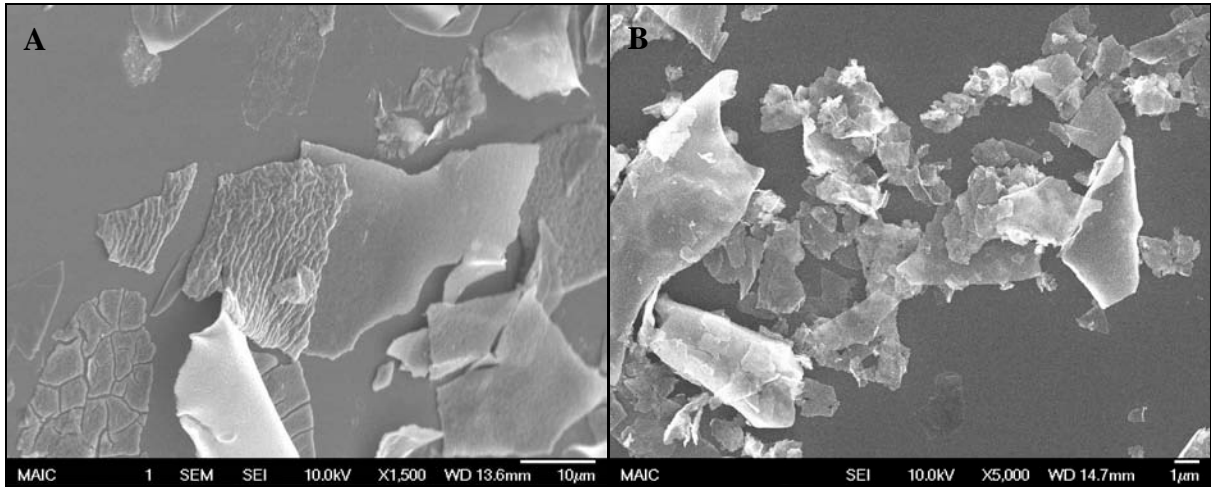


Figure 3-3. SEM images of titania samples. A) synthesized flakes. B) calcined flakes.

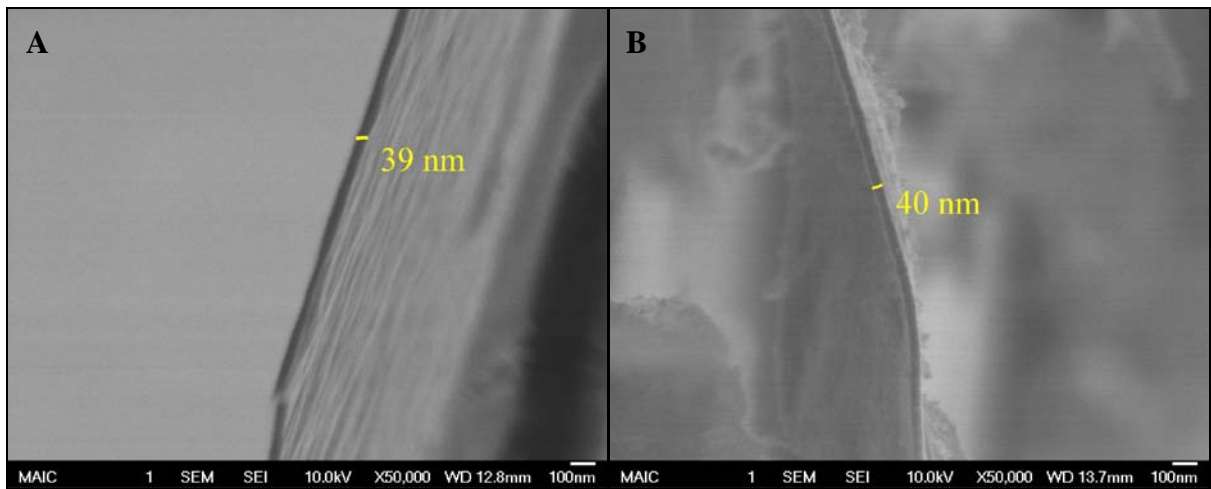


Figure 3-4. SEM images of edge view of titania samples. A) synthesized flakes. B) calcined flakes.

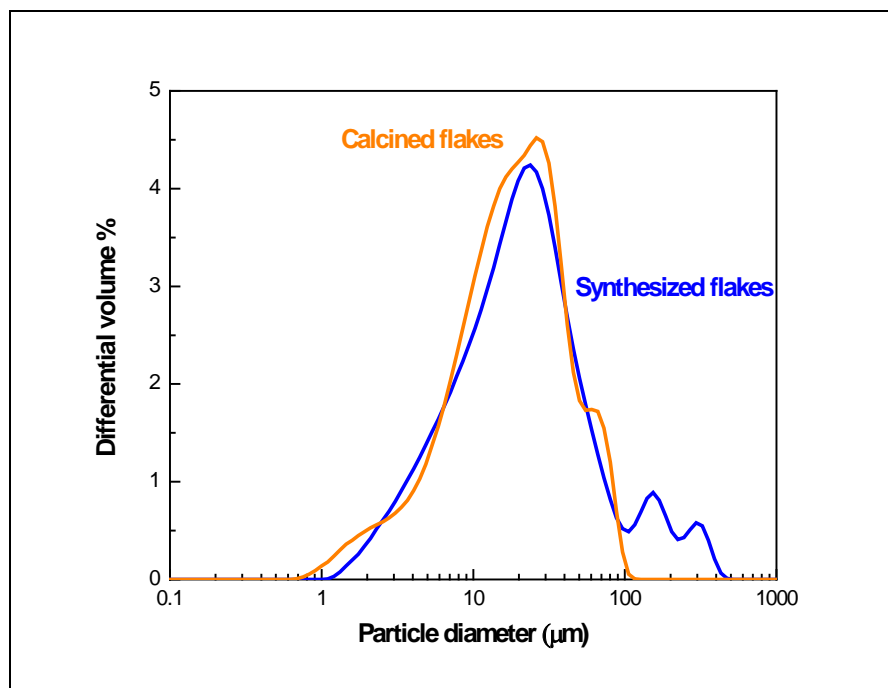


Figure 3-5. Particle size distribution for synthesized and calcined flakes.

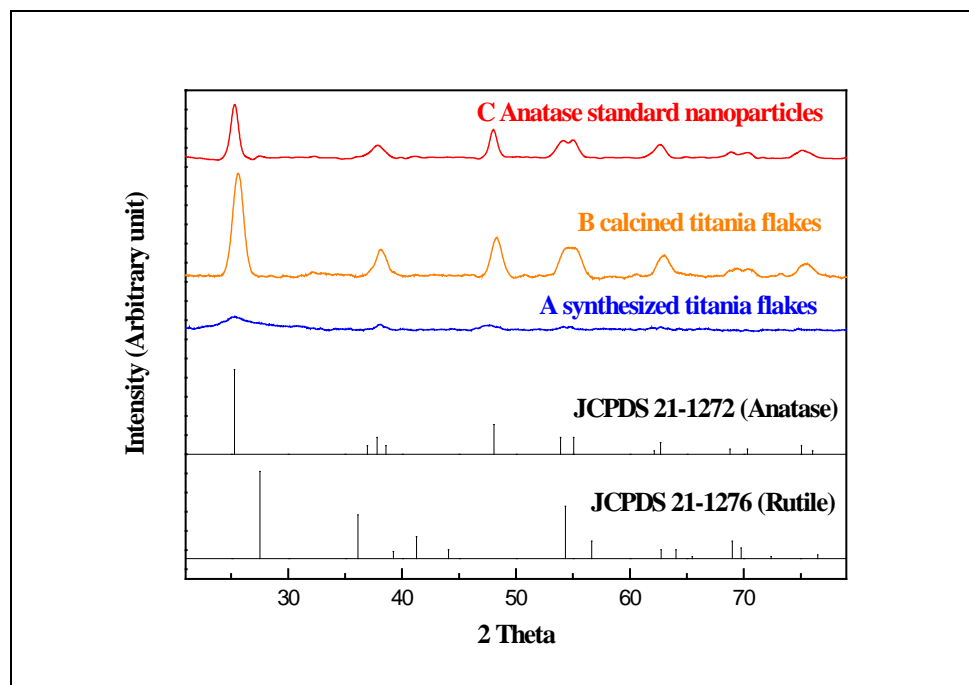


Figure 3-6. XRD patterns of titania samples. A) synthesized flakes. B) calcined flakes. C) Anatase nanoparticles (Titanium(IV) oxide nanopowder, 99.9% anatase, Fisher Chemical).

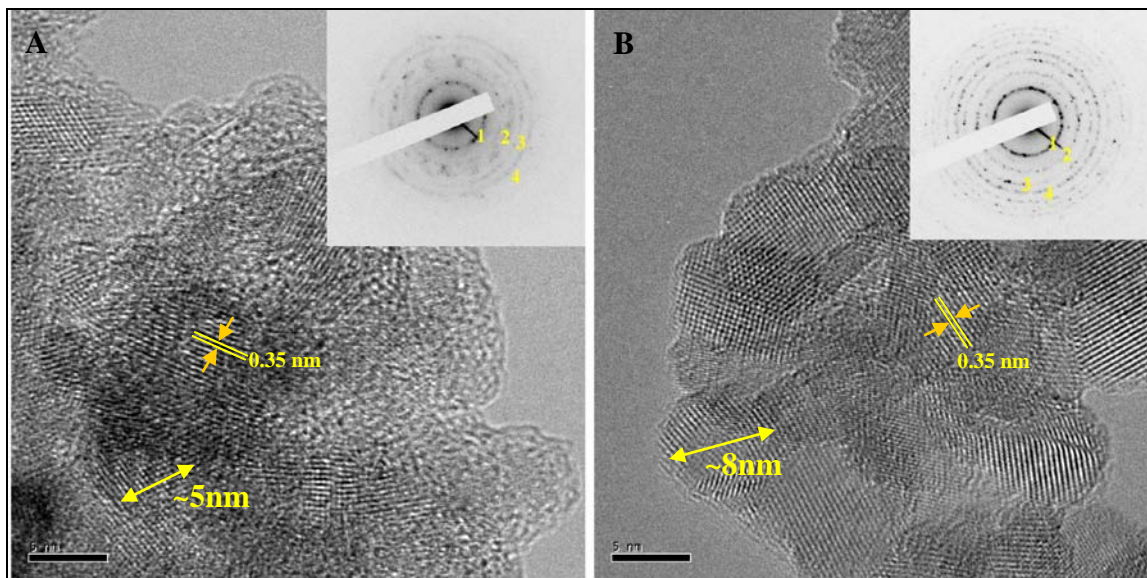


Figure 3-7. HR-TEM images of titania samples (the SAD pattern as inset). A) synthesized flakes. B) calcined flakes. The diffraction rings are indexed as (1) 101 (2) 004 (3) 200 (4) 105 for anatase.

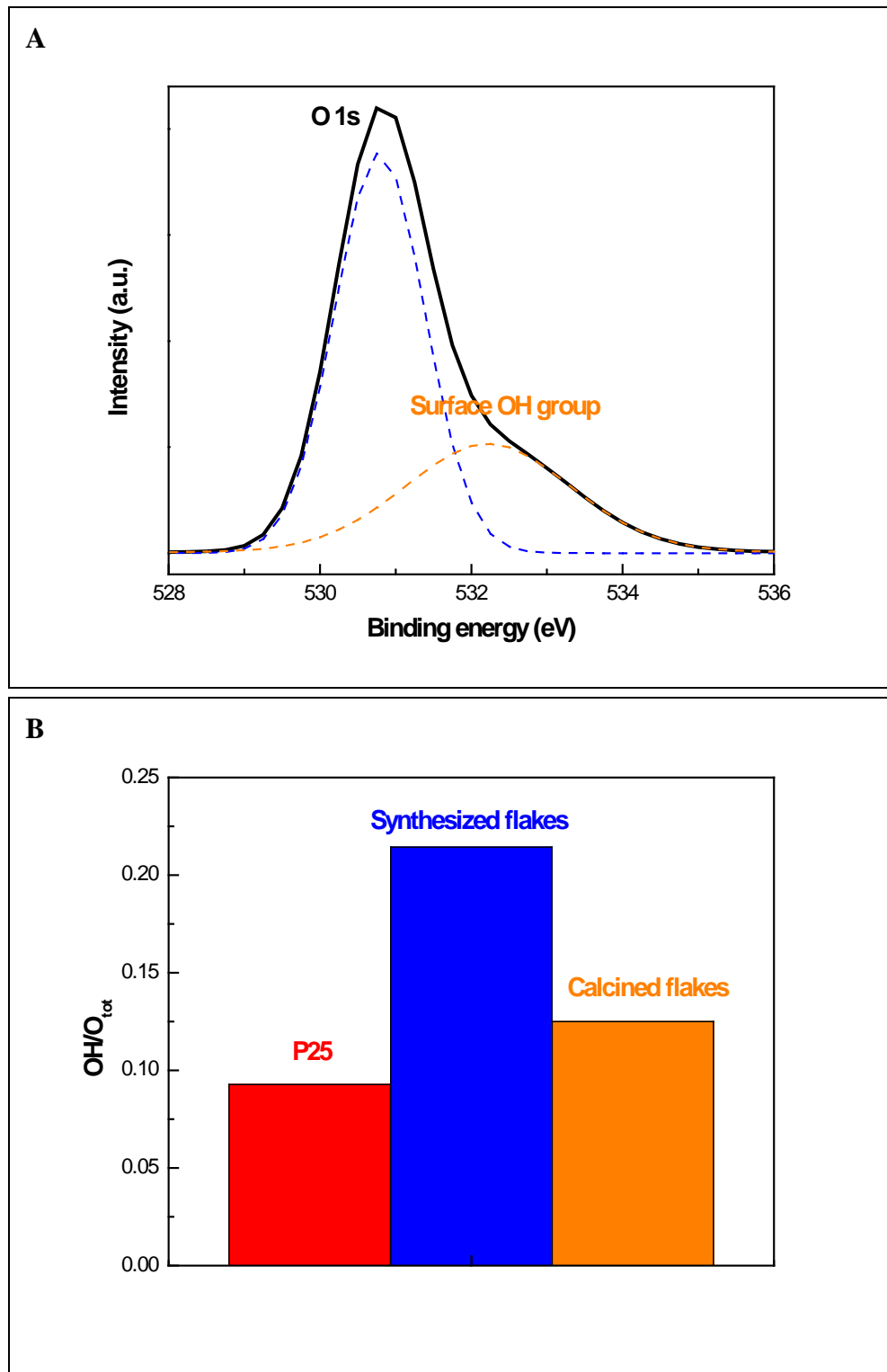


Figure 3-8. XPS analysis of the titania samples. A) O 1s peak fitting of synthesized flakes. B) OH/O_{tot} XPS surface ratio of the titania samples.

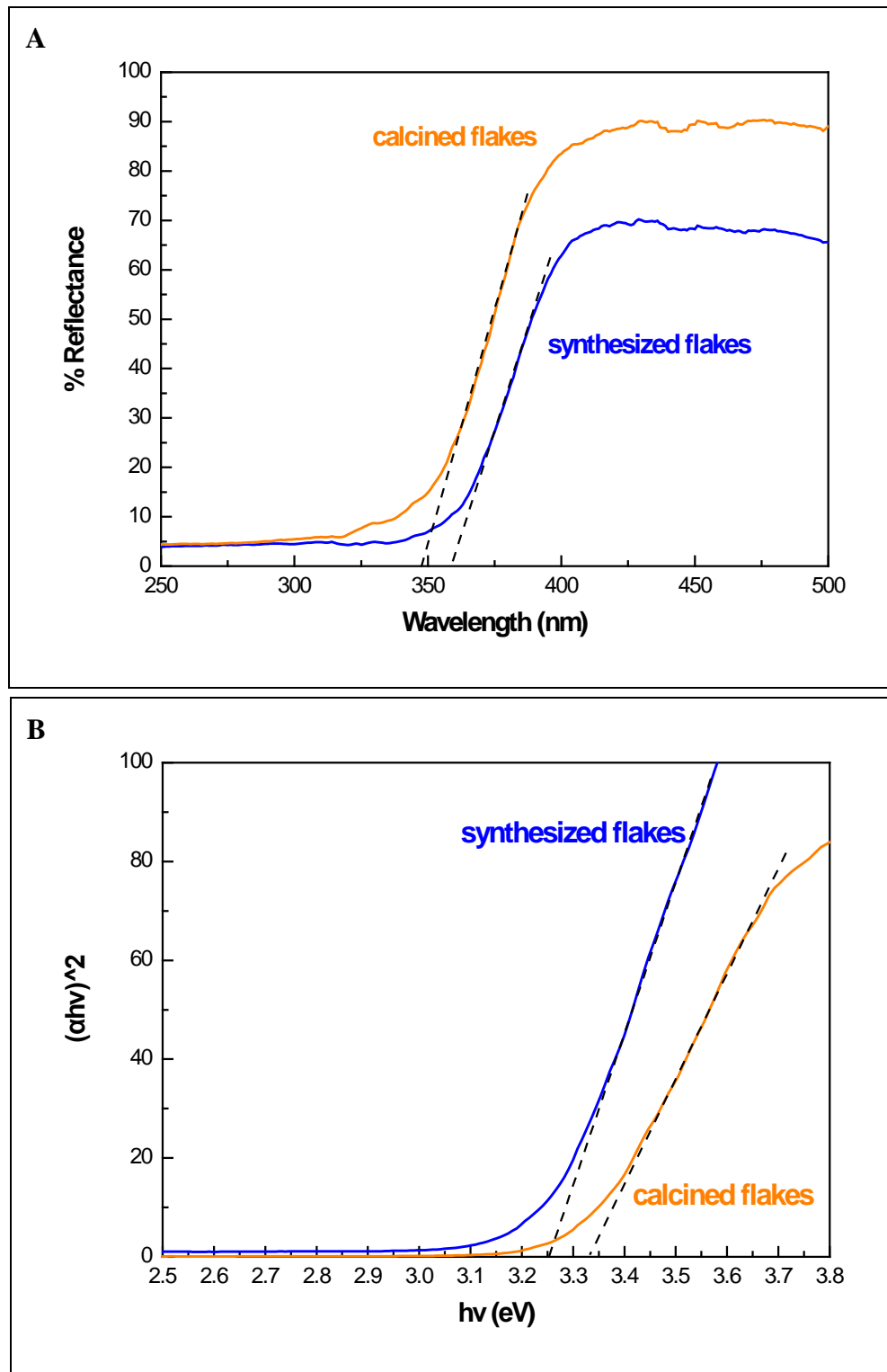


Figure 3-9. UV-Visible spectra of titania samples. A) Diffuse reflectance spectra. B) the dependence of $(\alpha h\nu)^2$ on the photon energy for synthesized and calcined titania flakes.

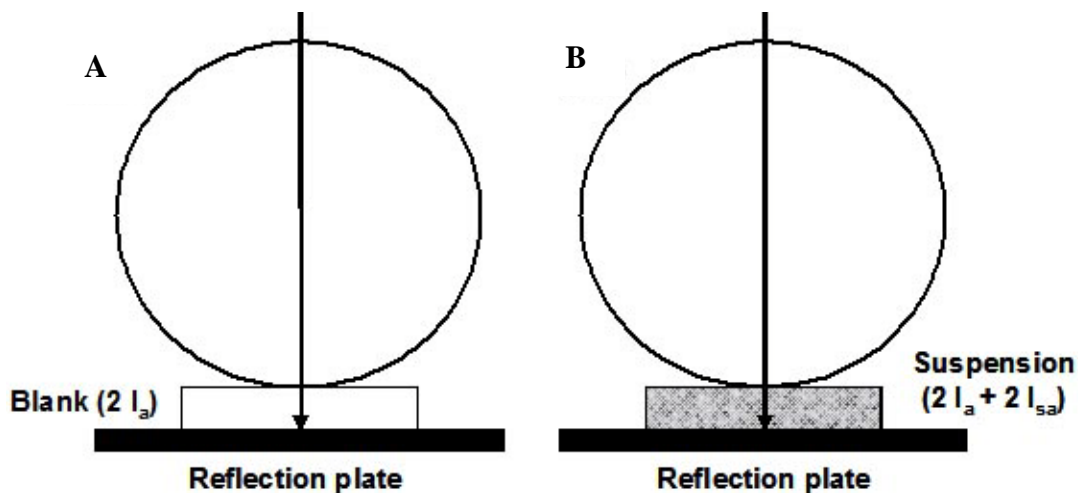


Figure 3-10. Schematic diagram of integrating sphere set-up in the modified method for measuring the true absorption of titania suspension. A) reference standard. B) sample [123].

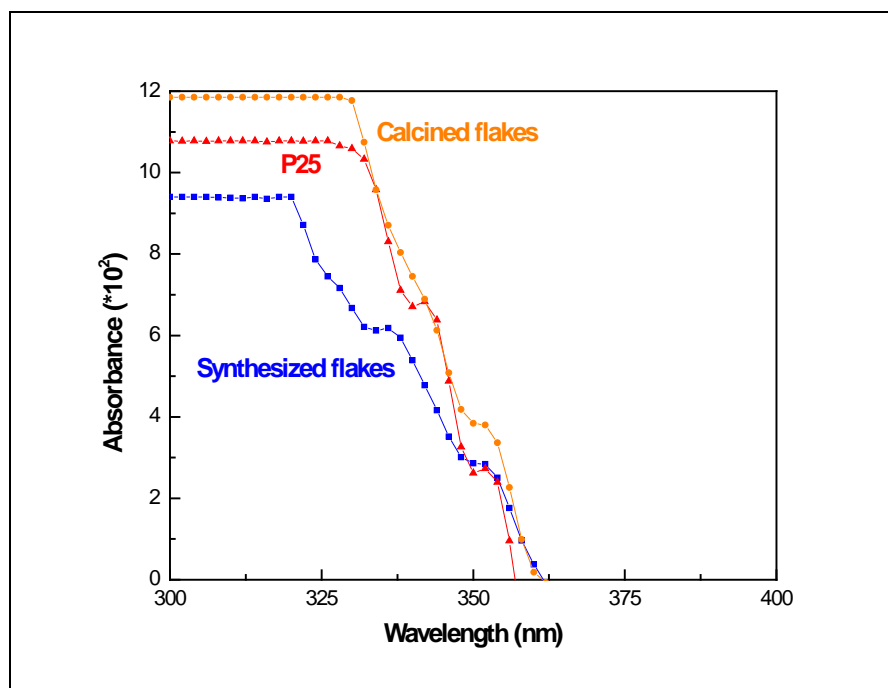


Figure 3-11. True absorption spectra of titania samples using the modified integration sphere method. (note: reflectivity in an integrating sphere is provided by a coating of pigment grade TiO₂ or ZnO. Thus the absorbance above represents only the increased absorbance over the control.)

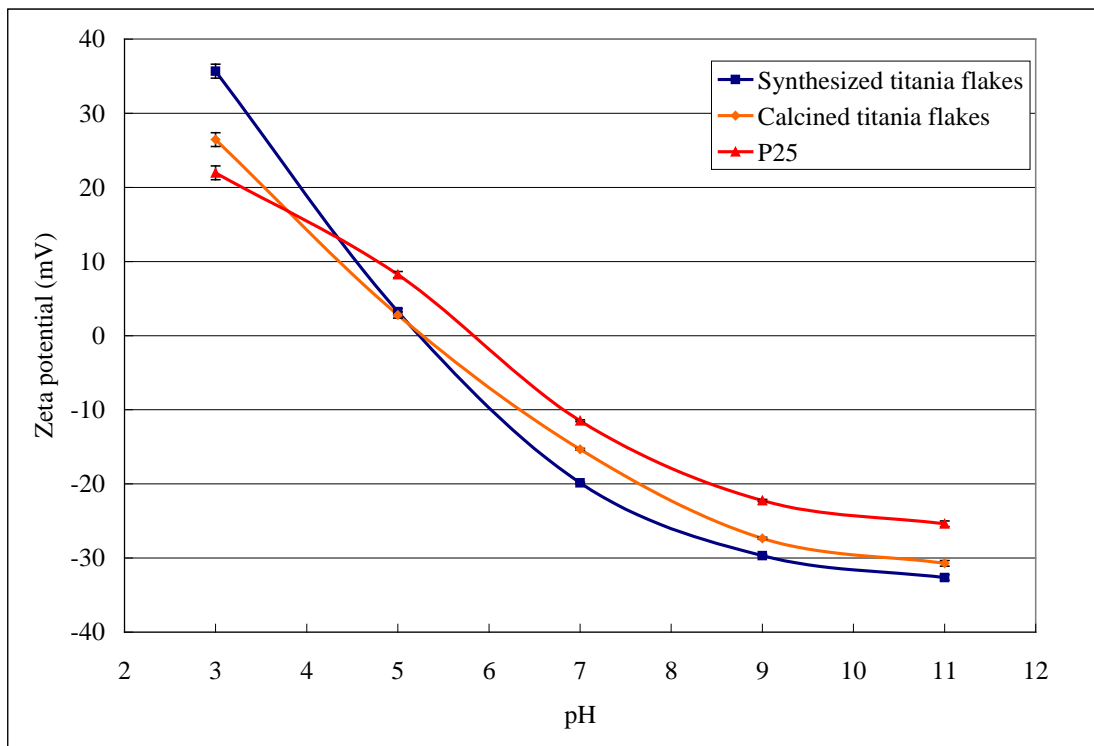


Figure 3-12. Zeta potential versus solution pH for three titania samples.

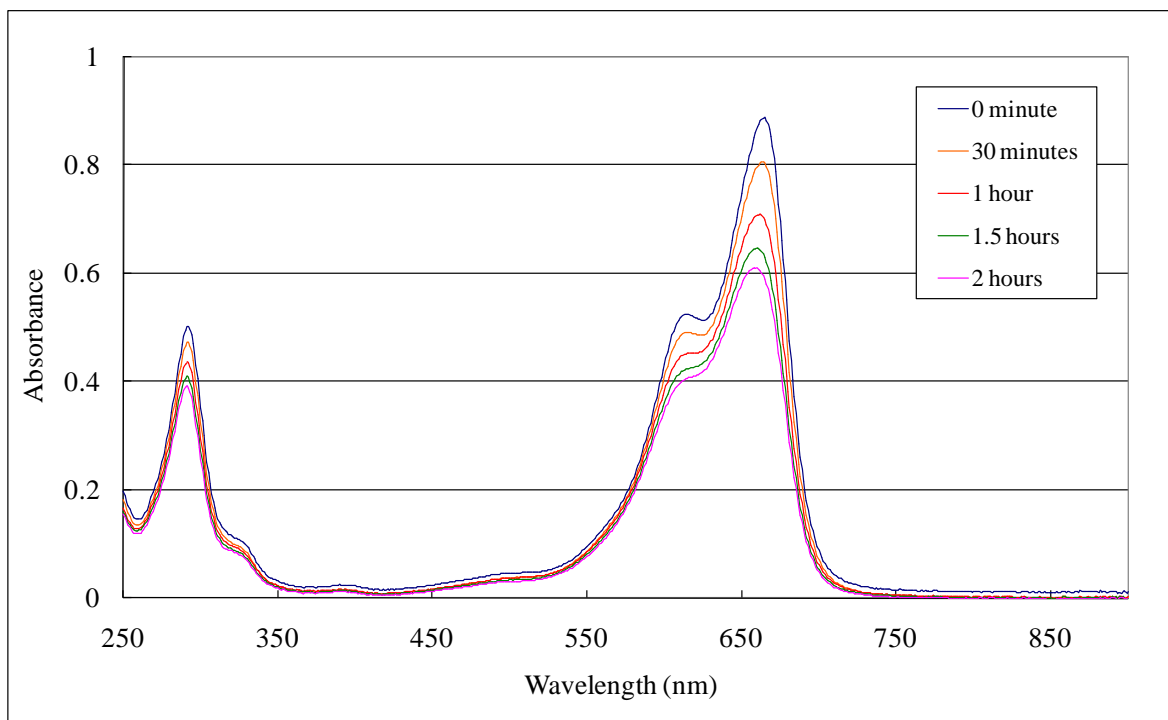


Figure 3-13. Photocatalytic decomposition of 50 μM methylene blue with synthesized titania flakes under UVA illumination.

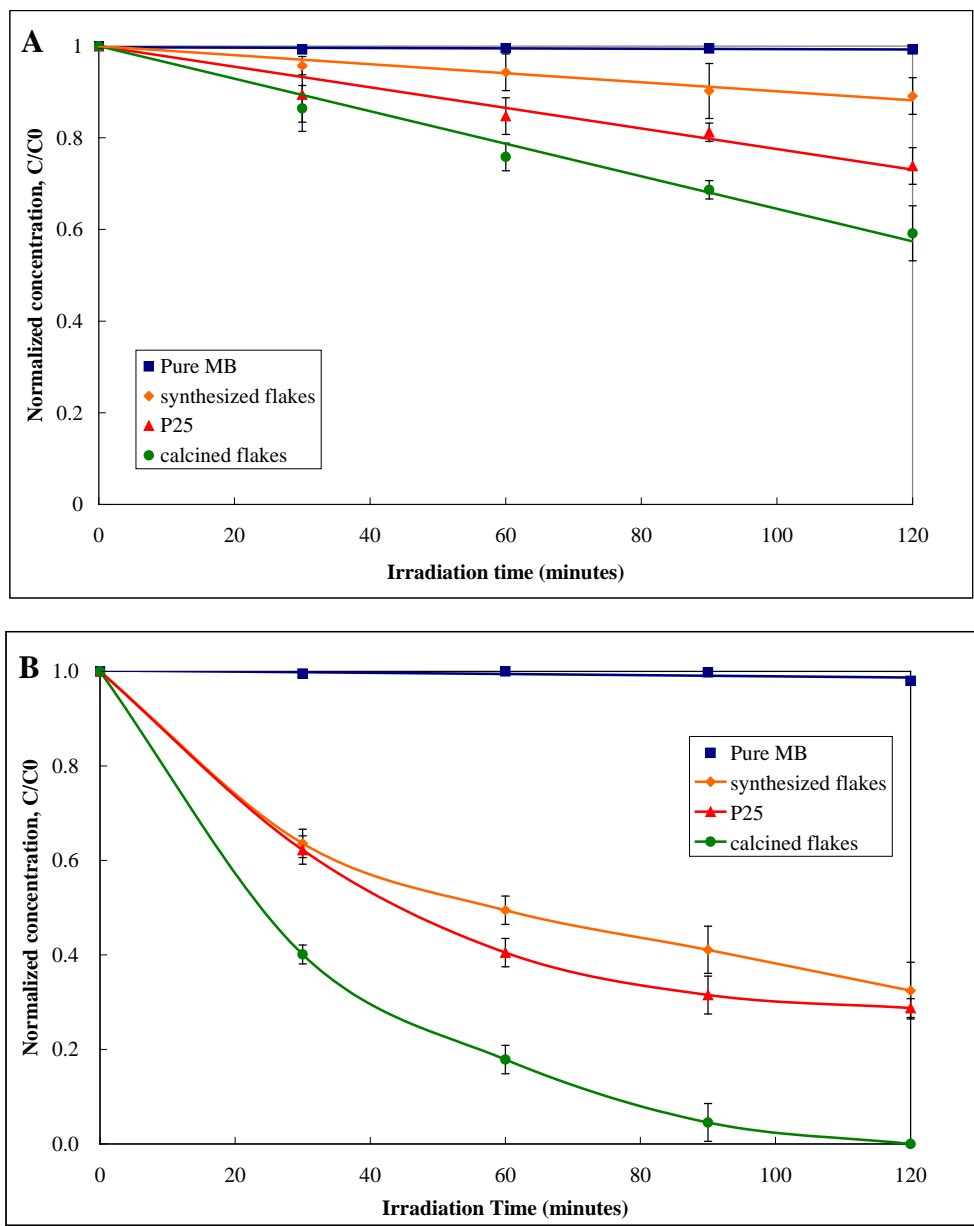


Figure 3-14. Photocatalytic decomposition of methylene blue by using synthesized and calcined flakes. A) without bubbling treatment. B) with bubbling treatment.

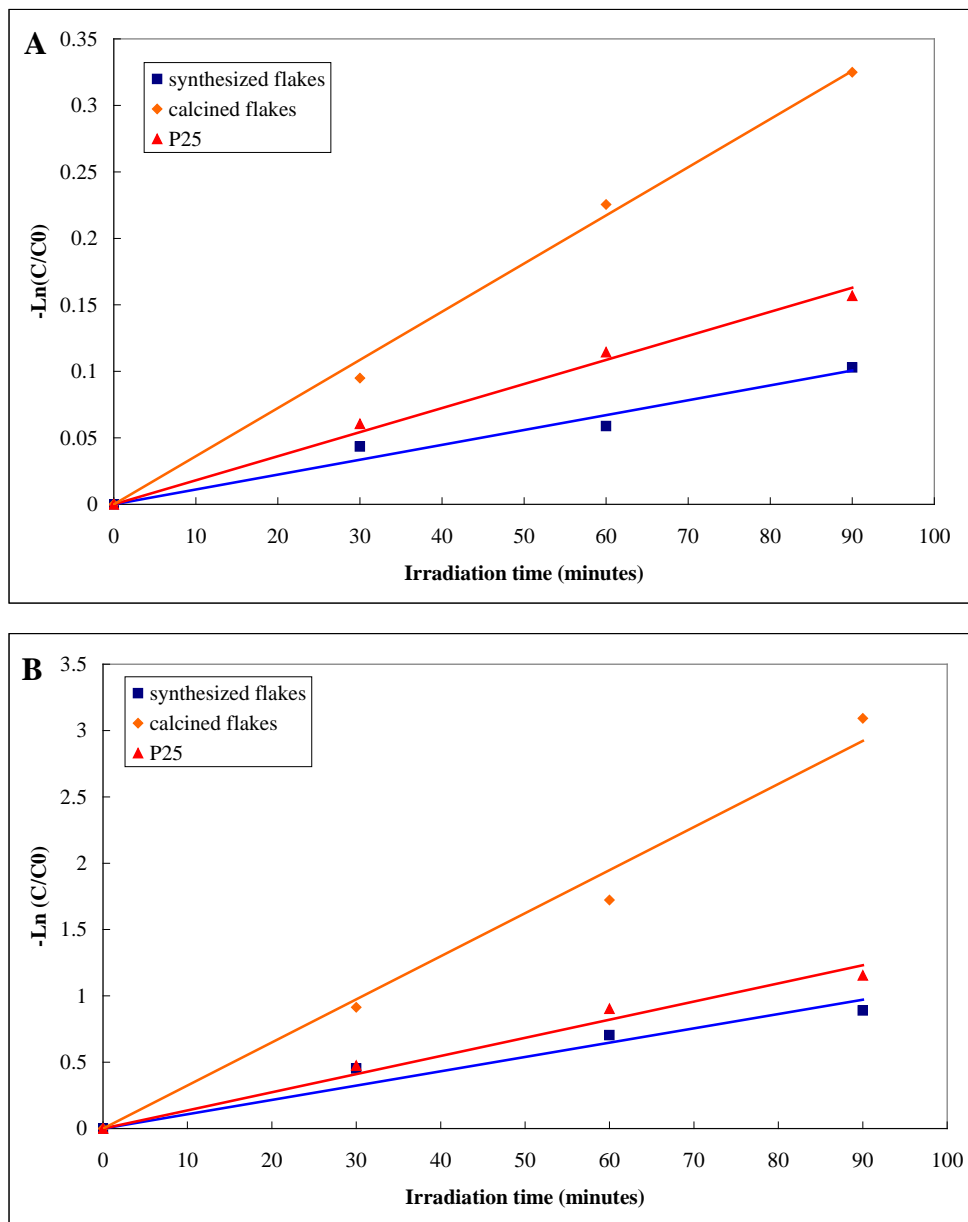


Figure 3-15. Linear transforms $-\ln(C/C_0)$ vs. time for methylene blue decomposition for different photocatalysts. A) without bubbling treatment. B) with bubbling treatment. Note the difference in scales of the normalized concentrations.

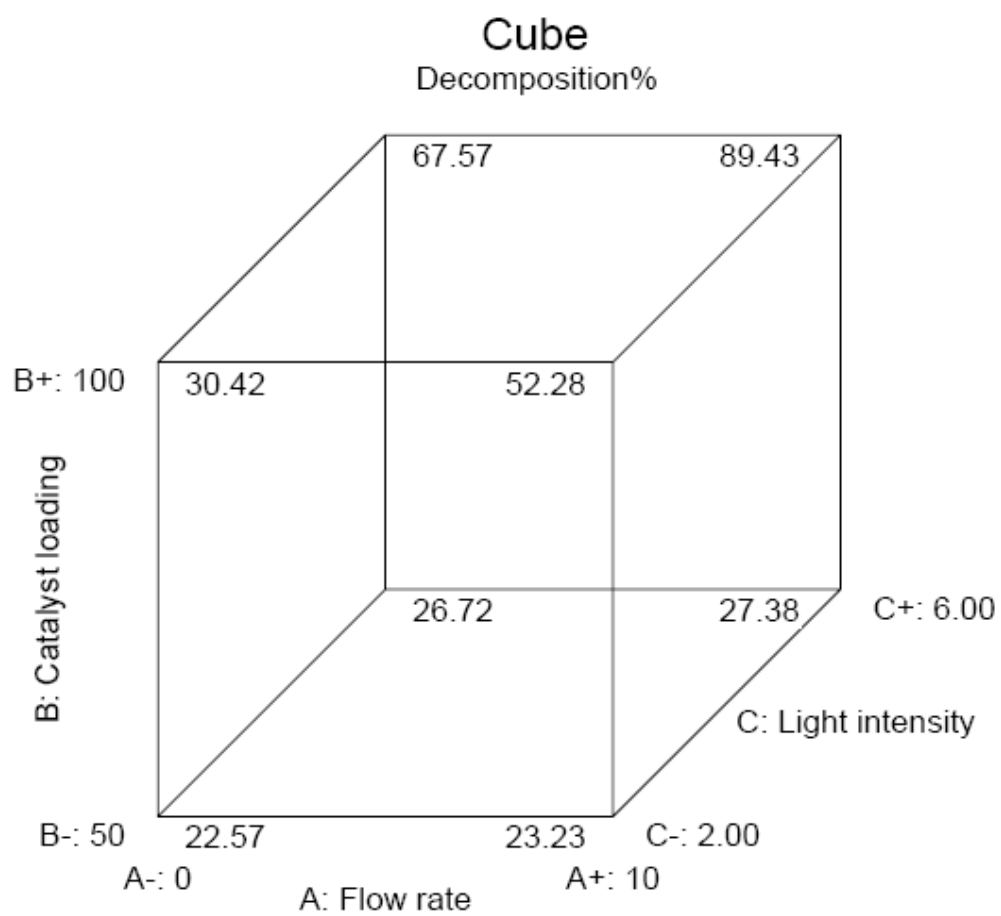


Figure 3-16. Experimental design decomposition% results of synthesized flakes photocatalysis.

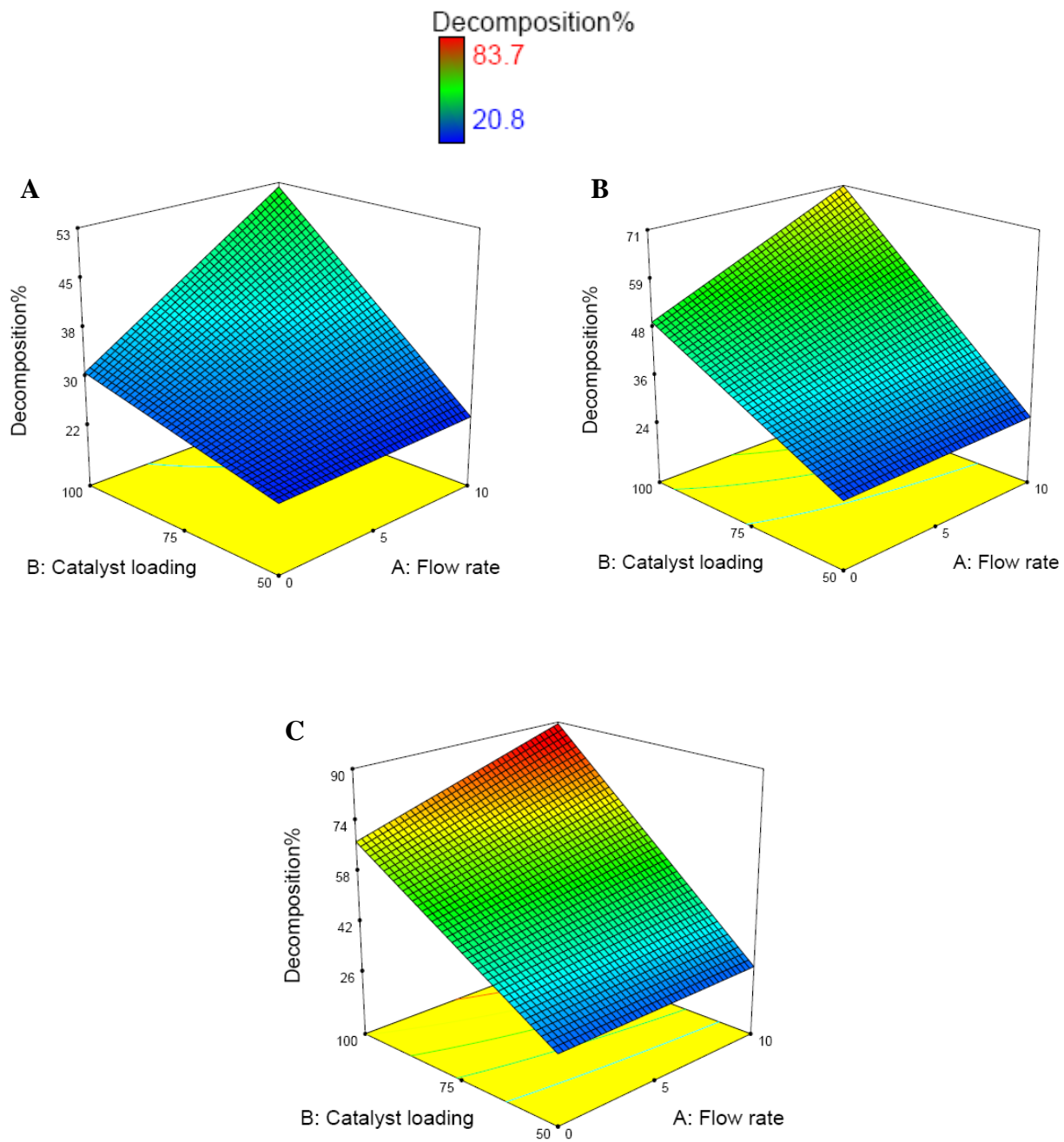


Figure 3-17. The 3D response surface plot of dye decomposition% of synthesized flakes as a function of the factor A and B under different light intensity. A) 2. B) 4. C) 6.

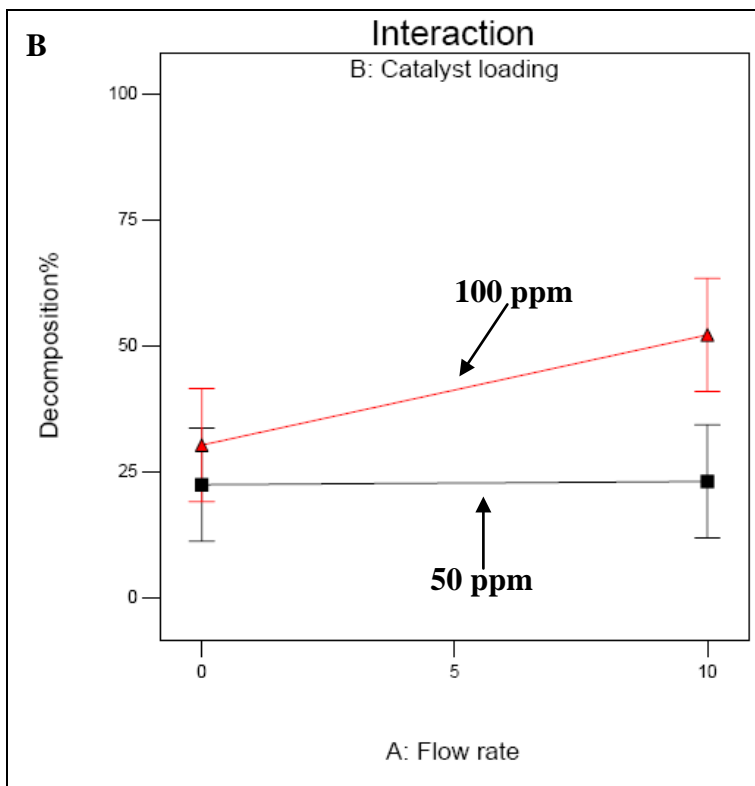
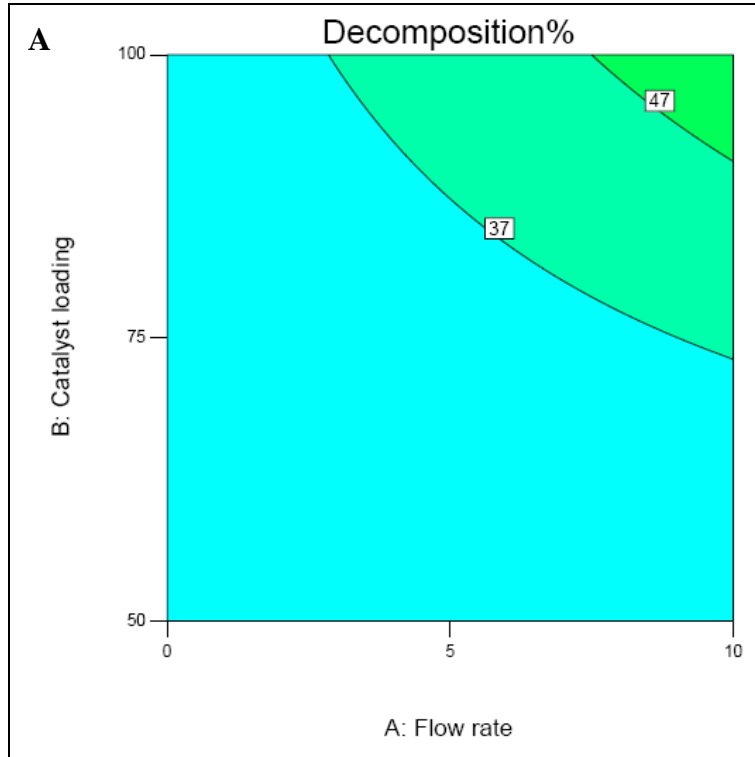


Figure 3-18. Model graphs of synthesized flakes as the function of A and B at constant light intensity ($C = 2$). A) Contour plot of decomposition% B) Interaction plot of response data against factor A for both levels of factor B.

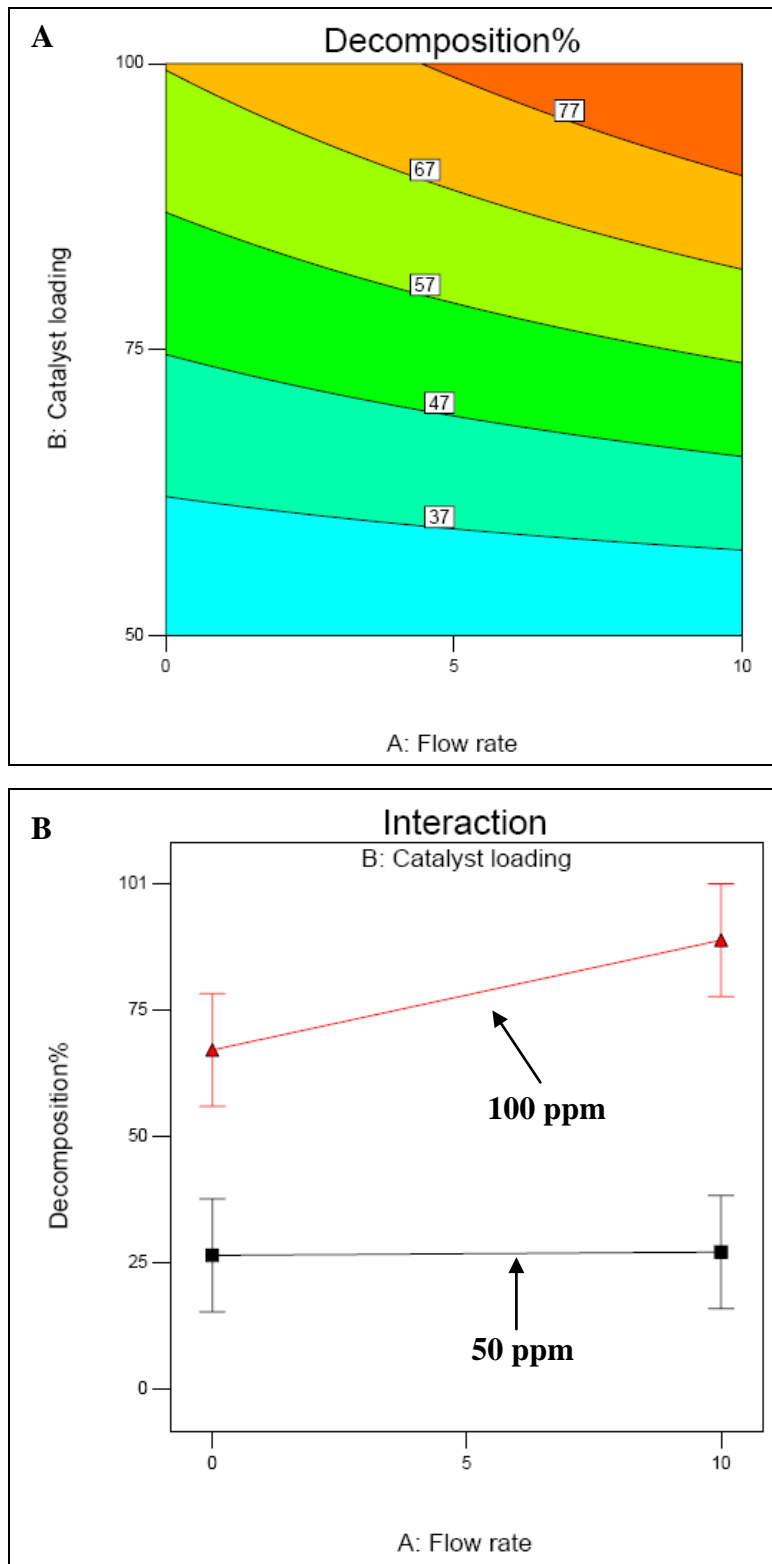


Figure 3-19. Model graphs of synthesized flakes as the function of A and B at constant light intensity ($C = 6$). A) Contour plot of decomposition%. B) Interaction plot of response data against factor A for both levels of factor B.

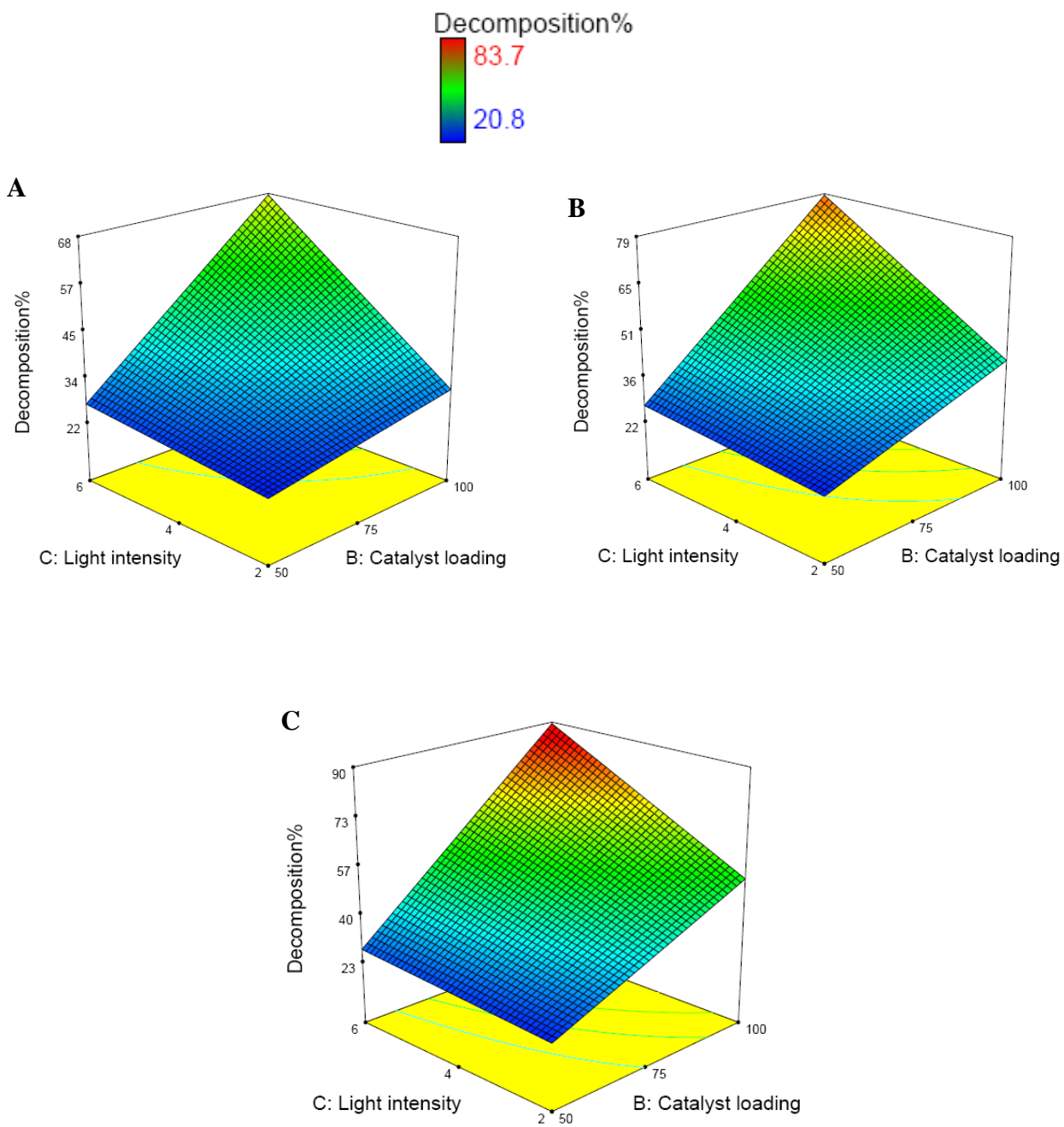


Figure 3-20. The 3D response surface plot of dye decomposition% of synthesized flakes as a function of the factor B and C under different aeration. A) 0. B) 5. C) 10 ft³/hr.

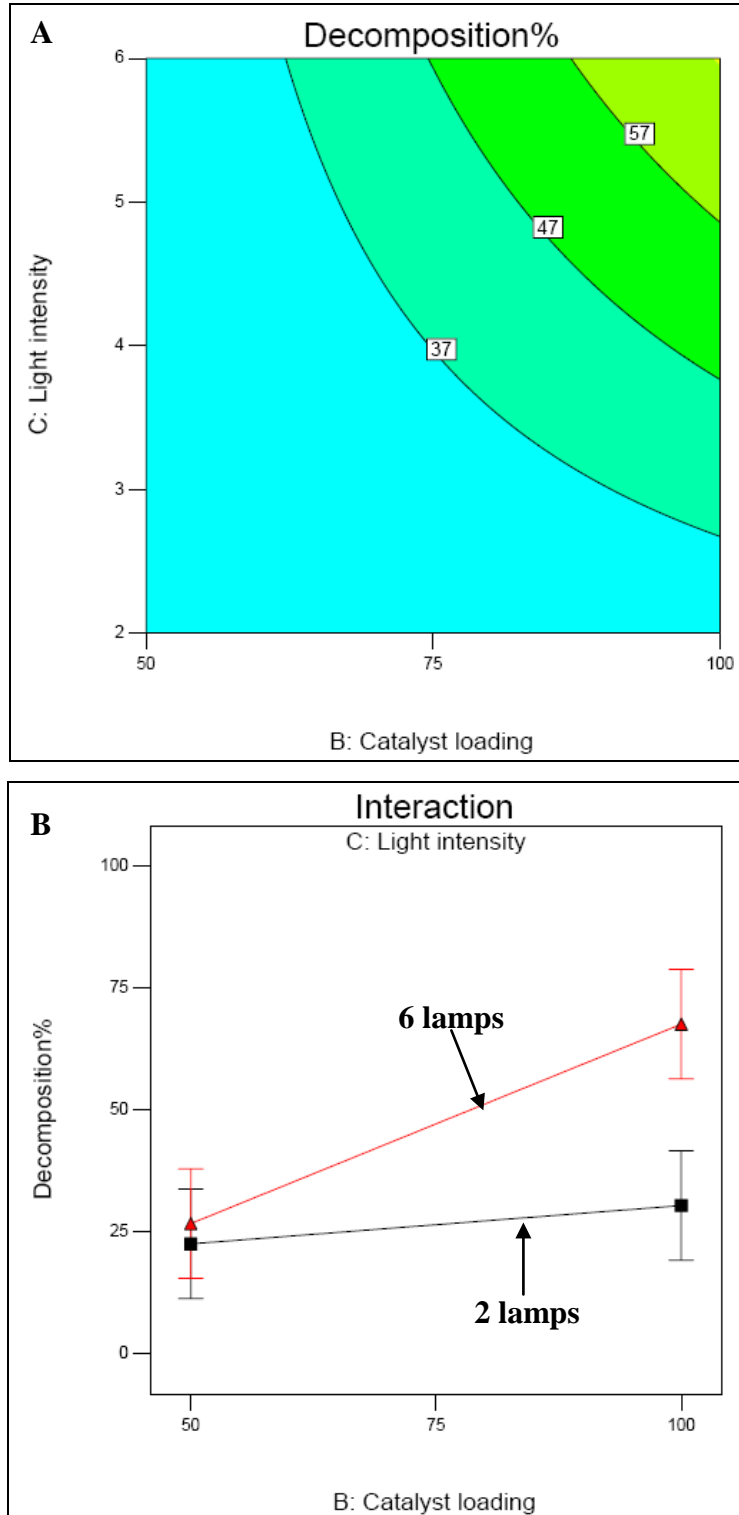


Figure 3-21. Model graphs of synthesized flakes as the function of B and C at constant flow rate (A = 0). A) Contour plot of decomposition%. B) Interaction plot of response data against factor B for both levels of factor C.

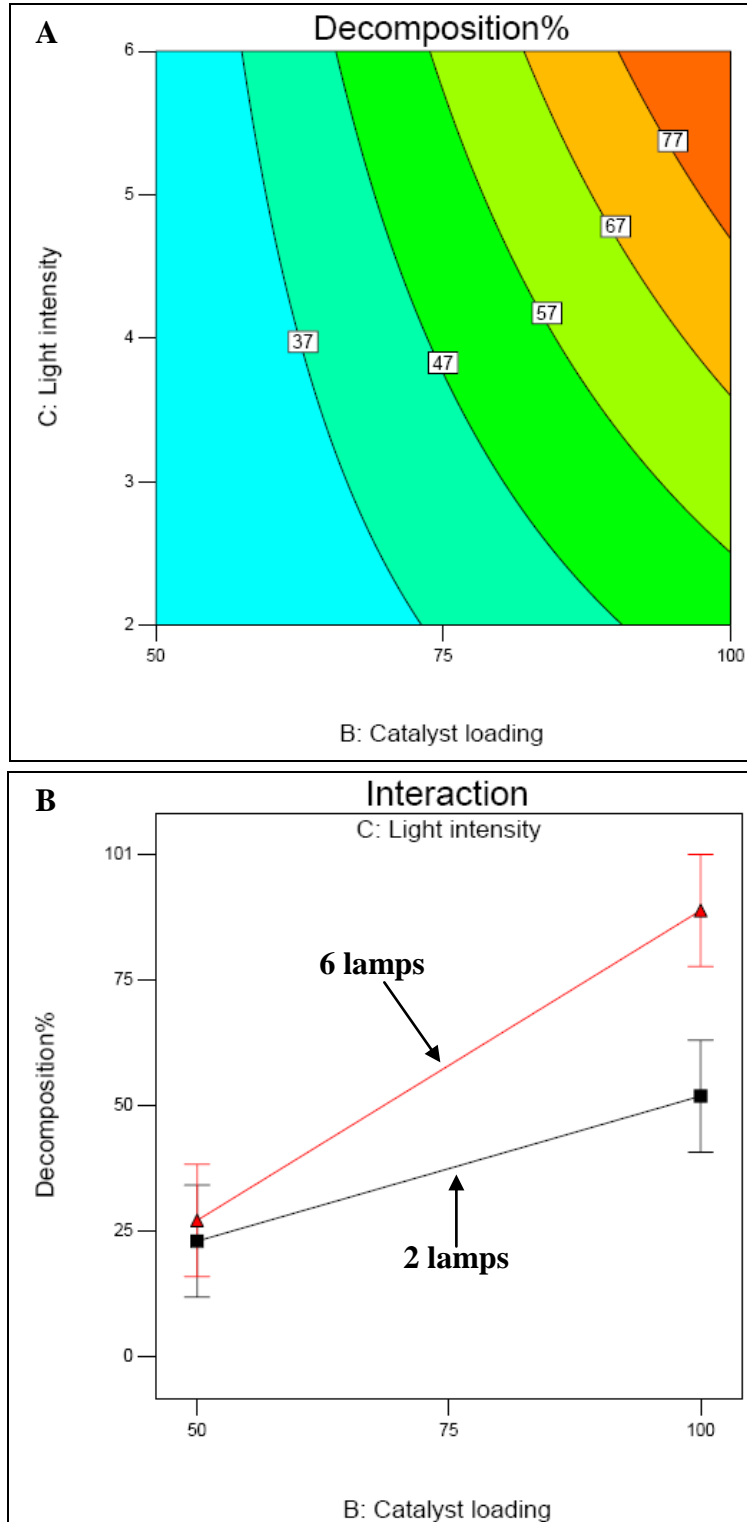


Figure 3-22. Model graphs of synthesized flakes as the function of B and C at constant flow rate (A = 10). A) Contour plot of decomposition% of synthesized flakes B) Interaction plot of response data against factor B for both levels of factor C.

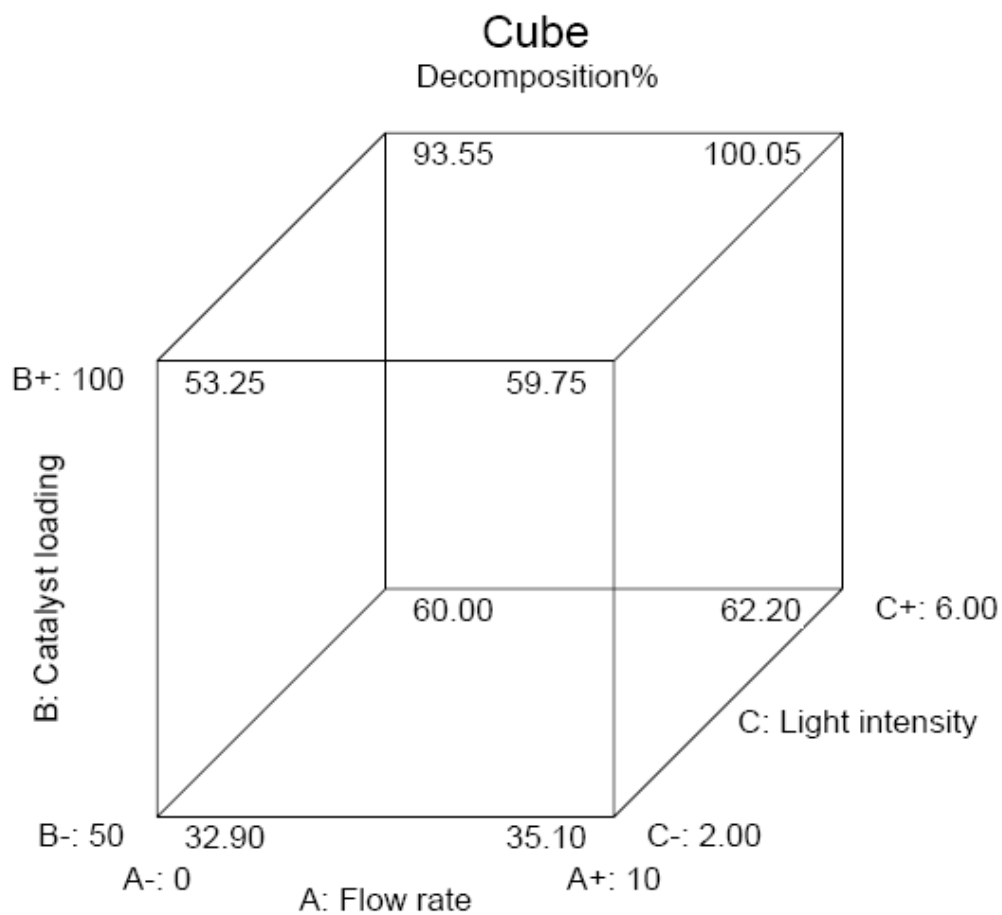


Figure 3-23. Experimental design decomposition% results of calcined flakes photocatalysis.

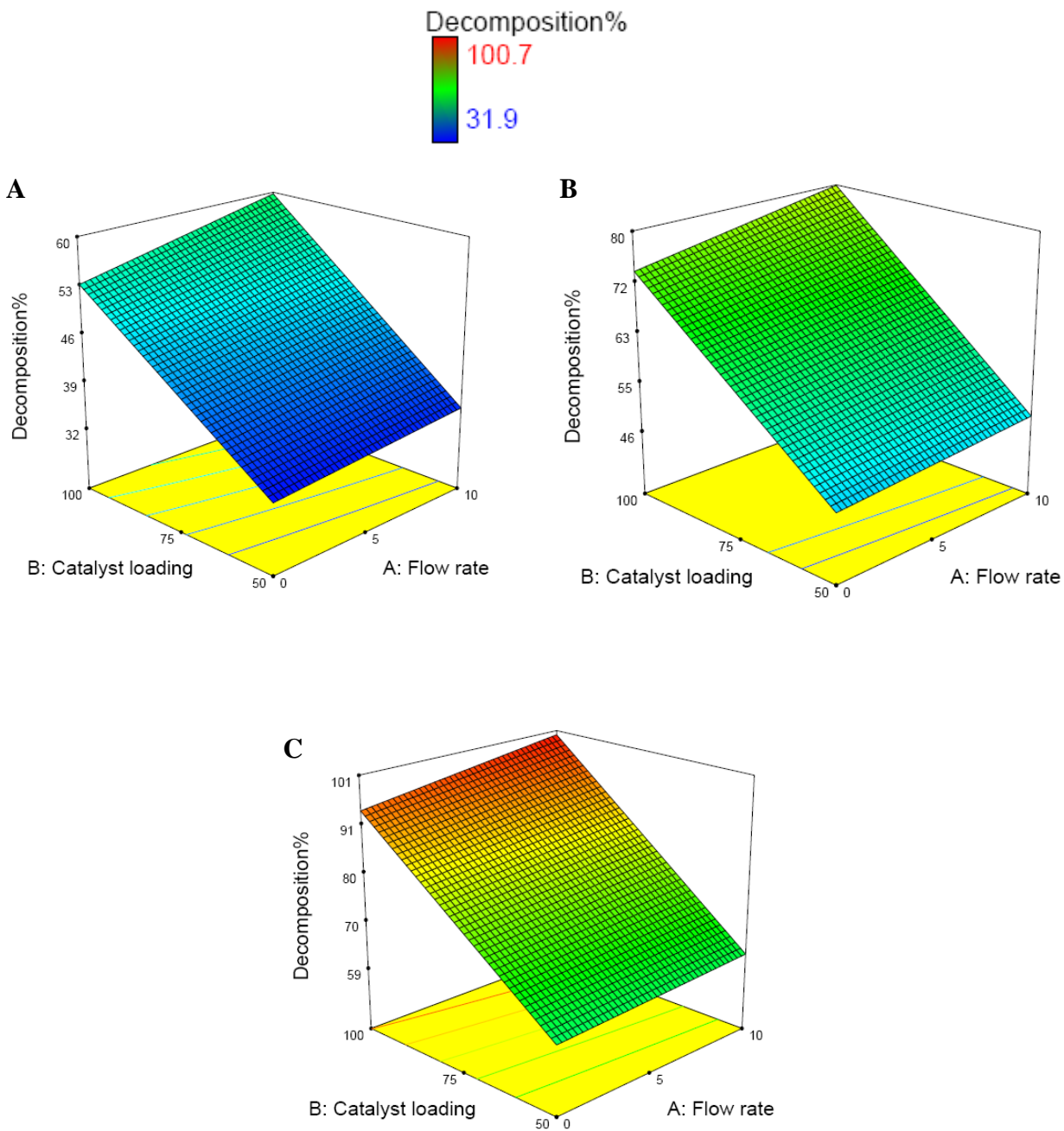


Figure 3-24. The 3D response surface plot of dye decomposition% of calcined flakes as a function of the factor A and B under different light intensity. A) 2. B) 4. C) 6.

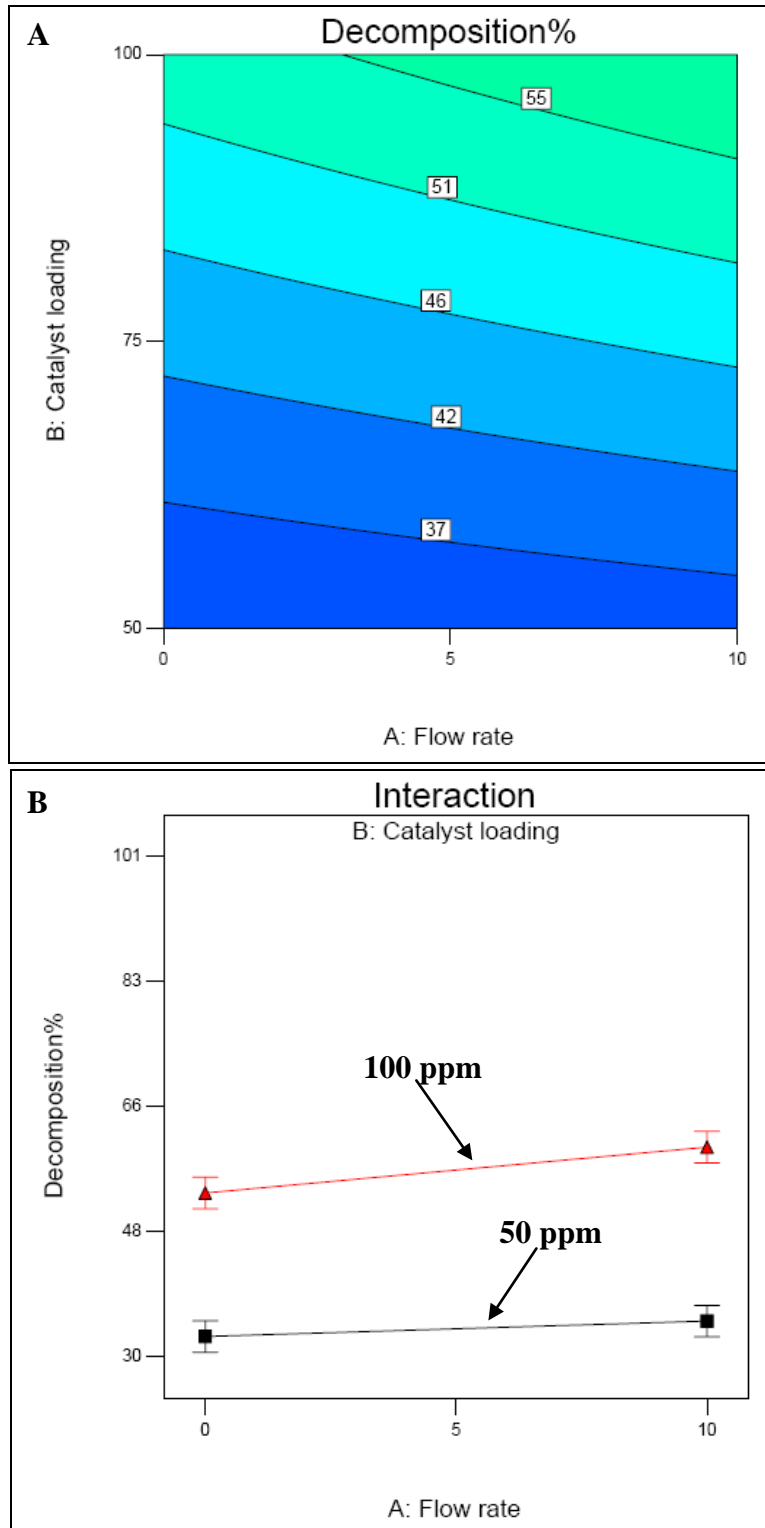


Figure 3-25. Model graphs of calcined flakes as the function of A and B at constant light intensity ($C = 2$). A) Contour plot of decomposition%. B) Interaction plot of response data against factor A for both levels of factor B.

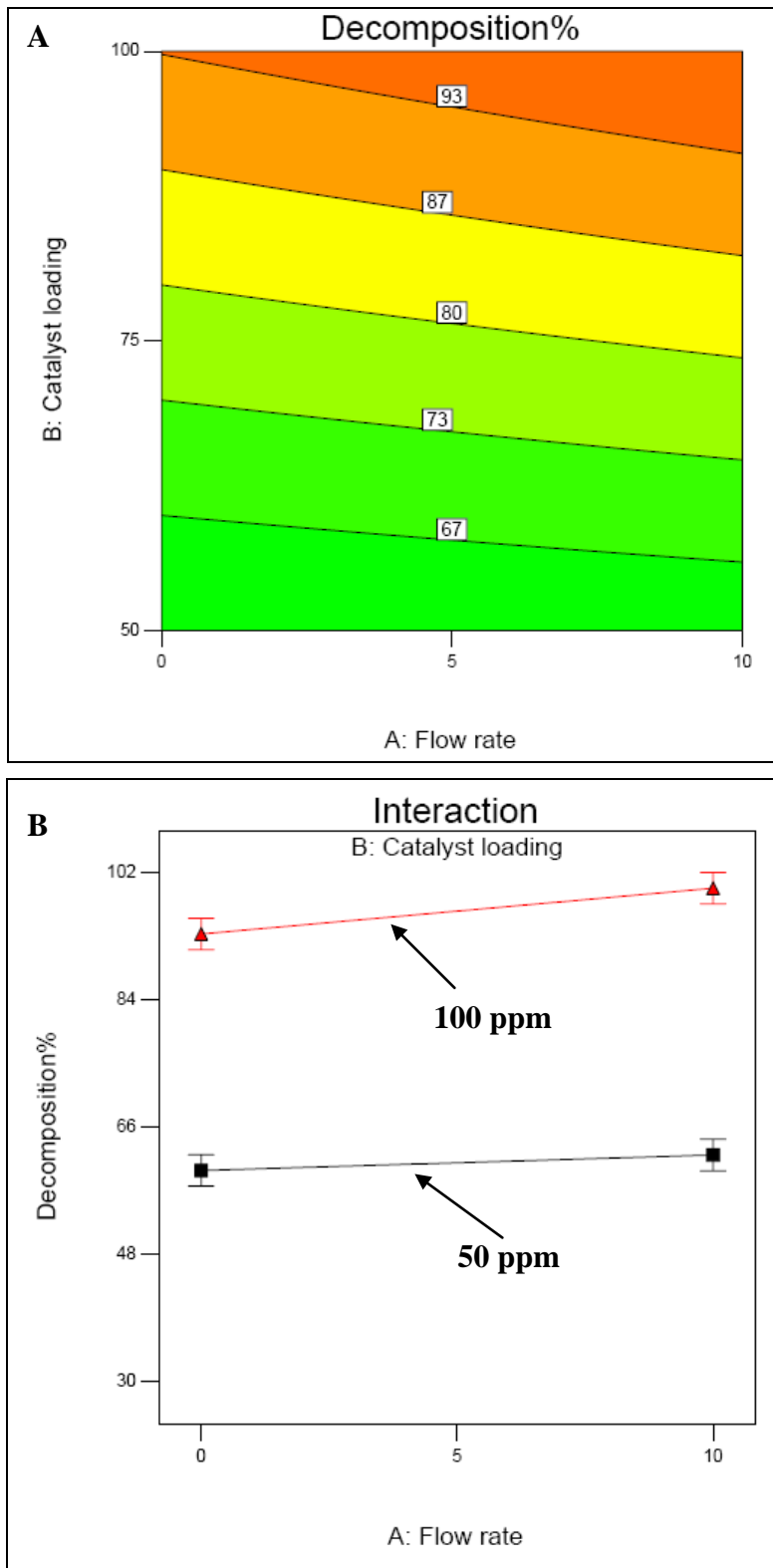


Figure 3-26. Model graphs of calcined flakes as the function of A and B at constant light intensity (C = 6). A) Contour plot of decomposition%. B) Interaction plot of response data against factor A for both levels of factor B.

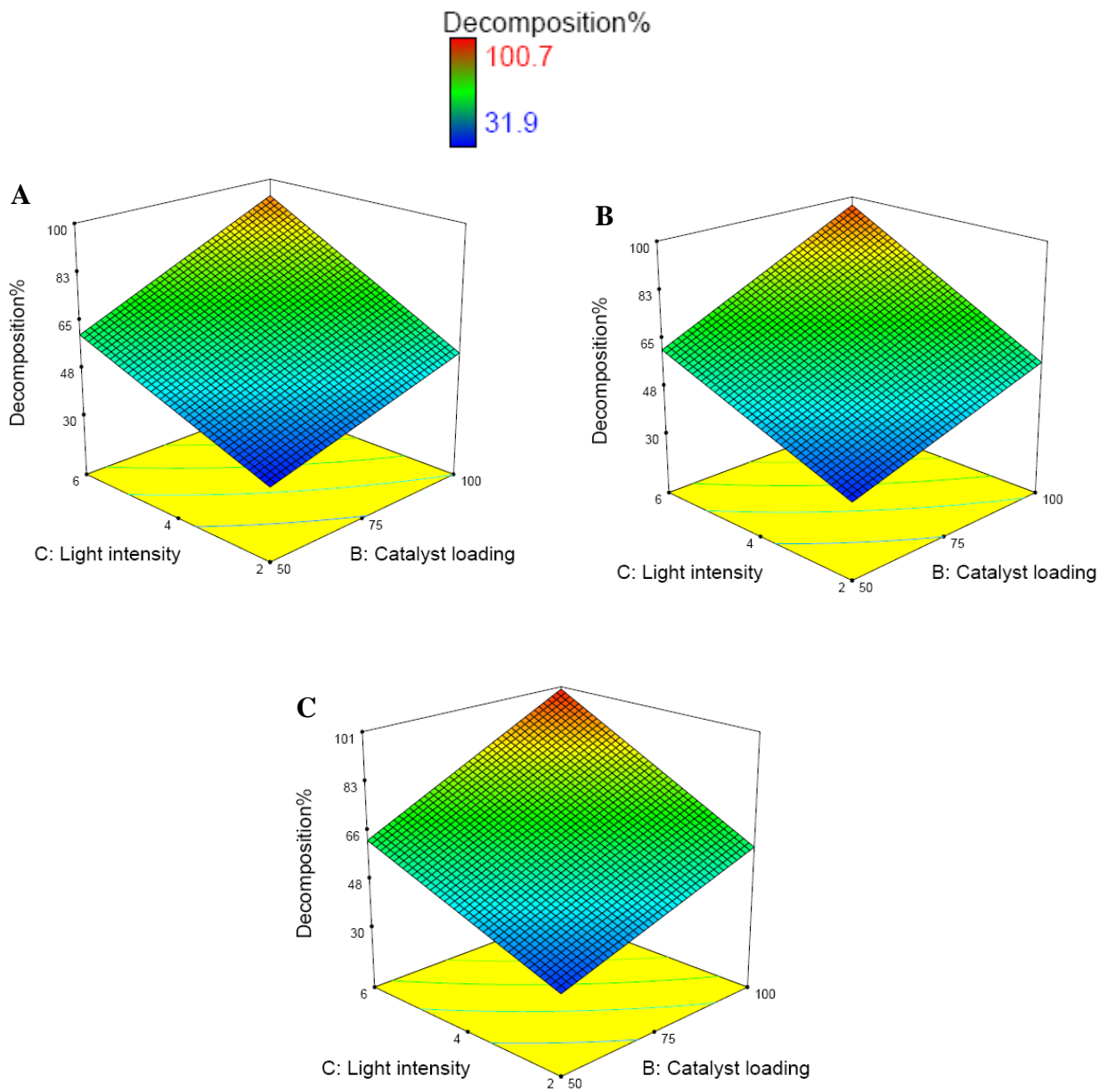


Figure 3-27. The 3D response surface plot of dye decomposition% of calcined flakes as a function of the factor B and C at different aeration rate. A) 0. B) 5. C) 10 ft³/hr.

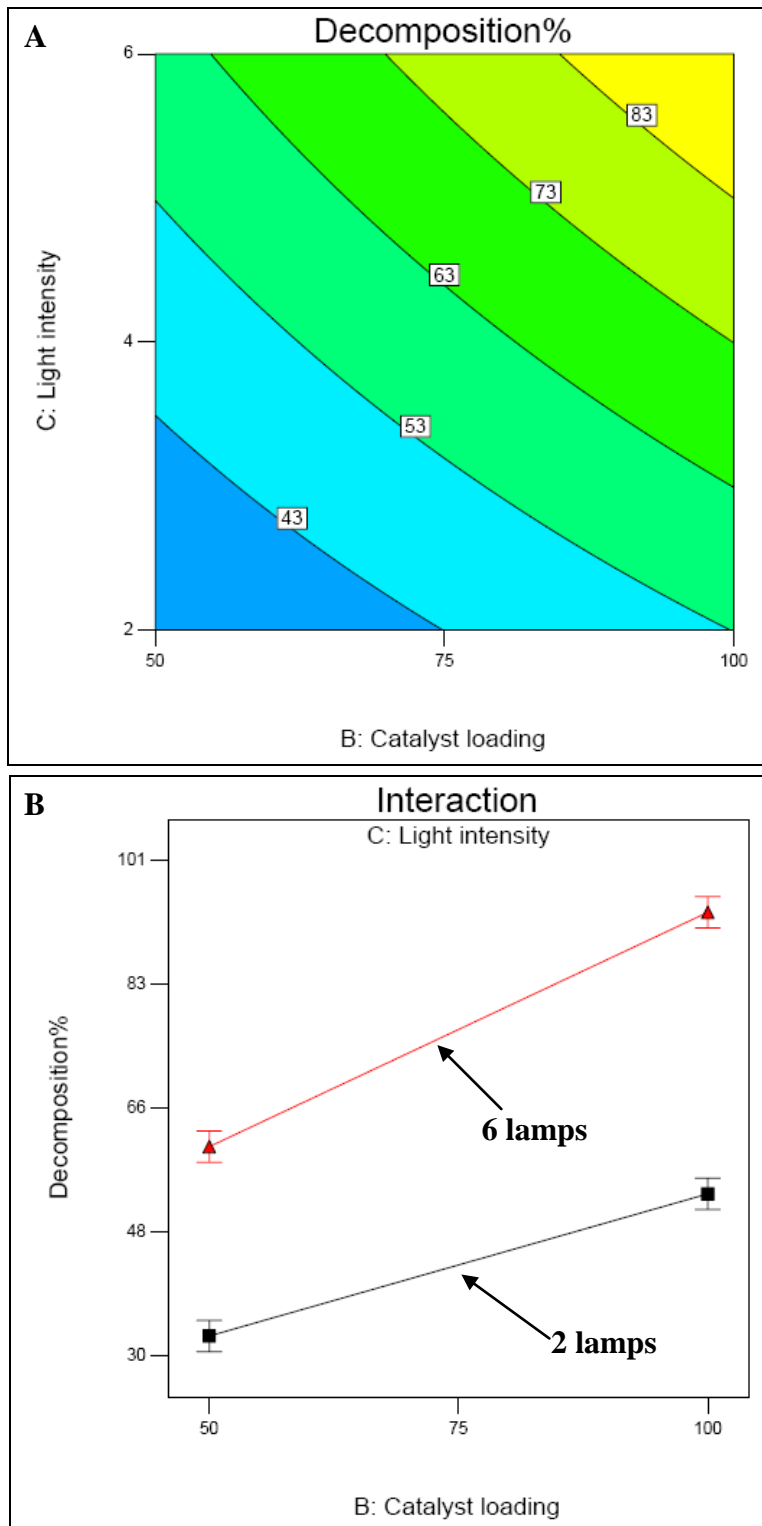


Figure 3-28. Model graphs of calcined flakes as the function of B and C at constant flow rate ($A = 0$). A) Contour plot of decomposition% of calcined flakes. B) Interaction plot of response data against factor B for both levels of factor C.

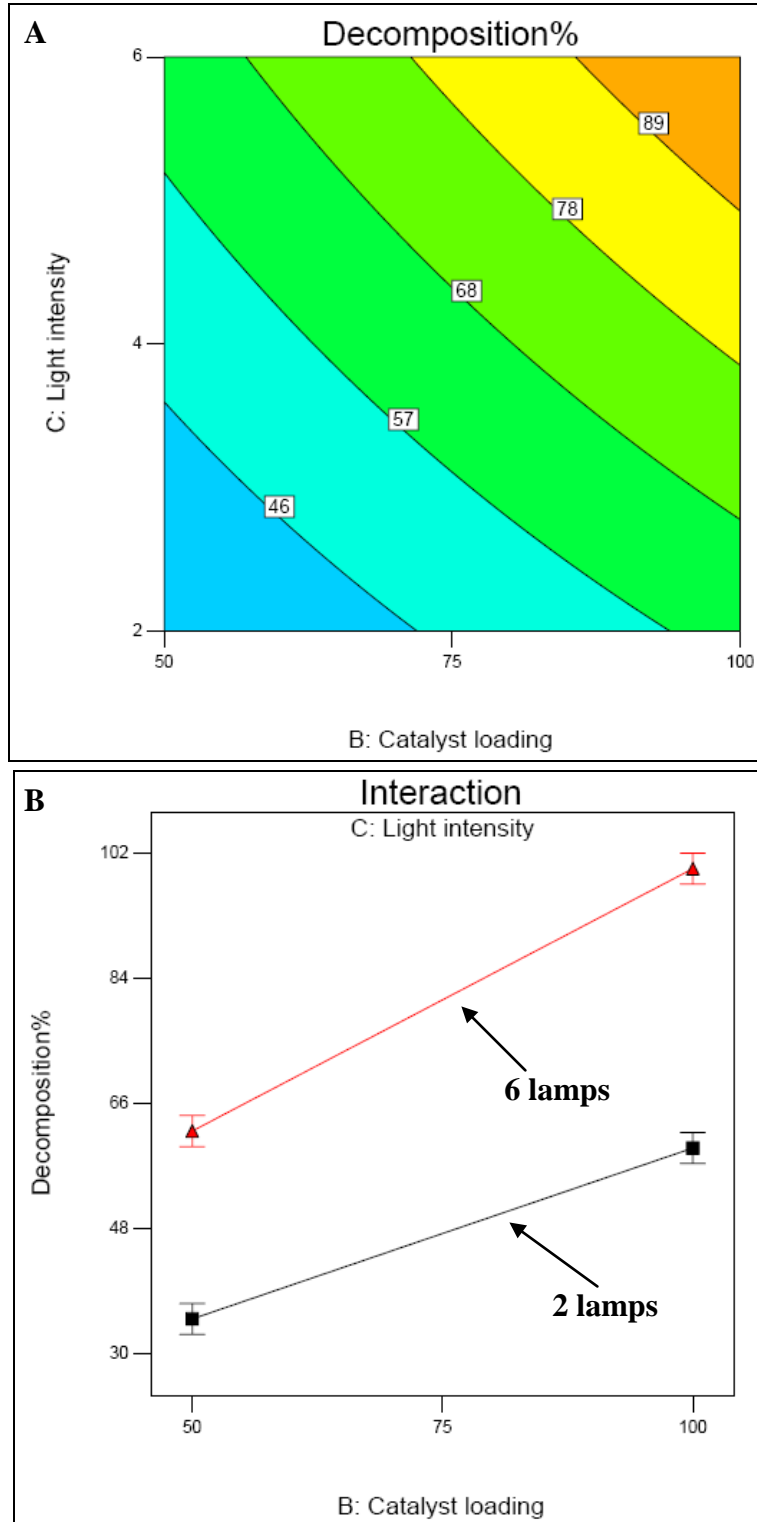


Figure 3-29. Model graphs of calcined flakes as the function of B and C with constant flow rate (A = 10). A) Contour plot of decomposition%. B) Interaction plot of response data against factor B for both levels of factor C.

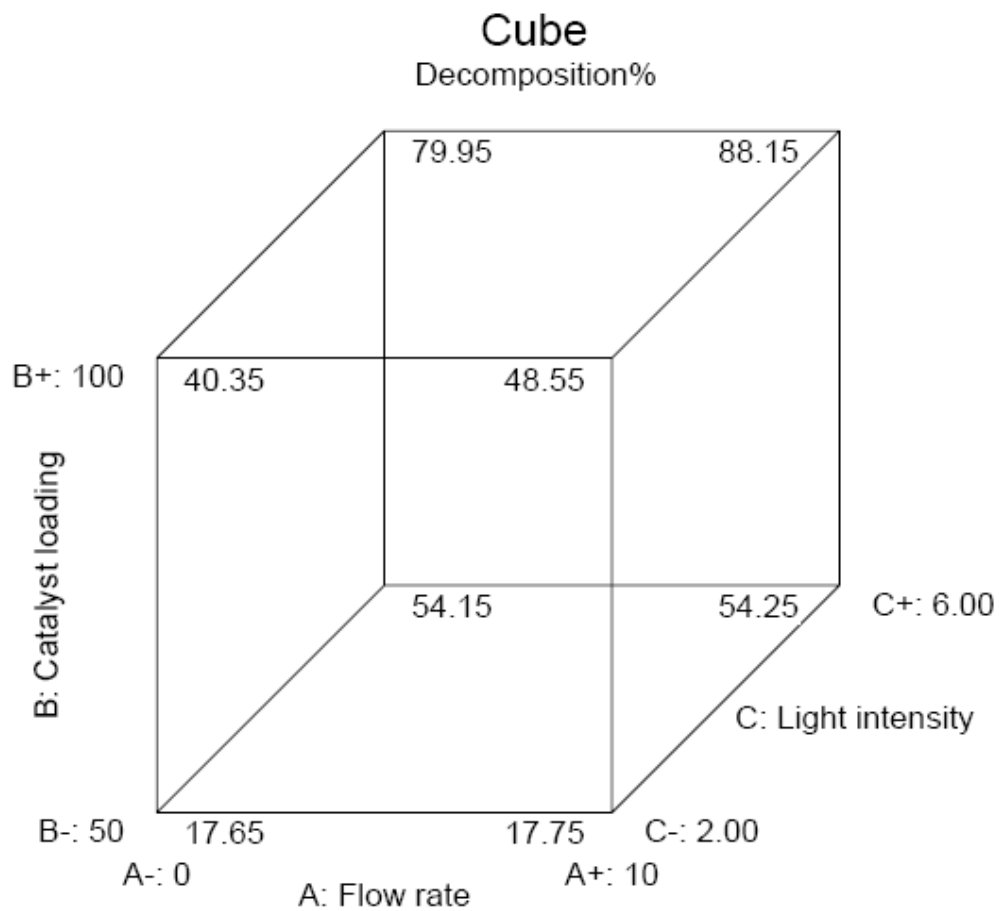


Figure 3-30. Experimental design decomposition% results of P25 photocatalysis.

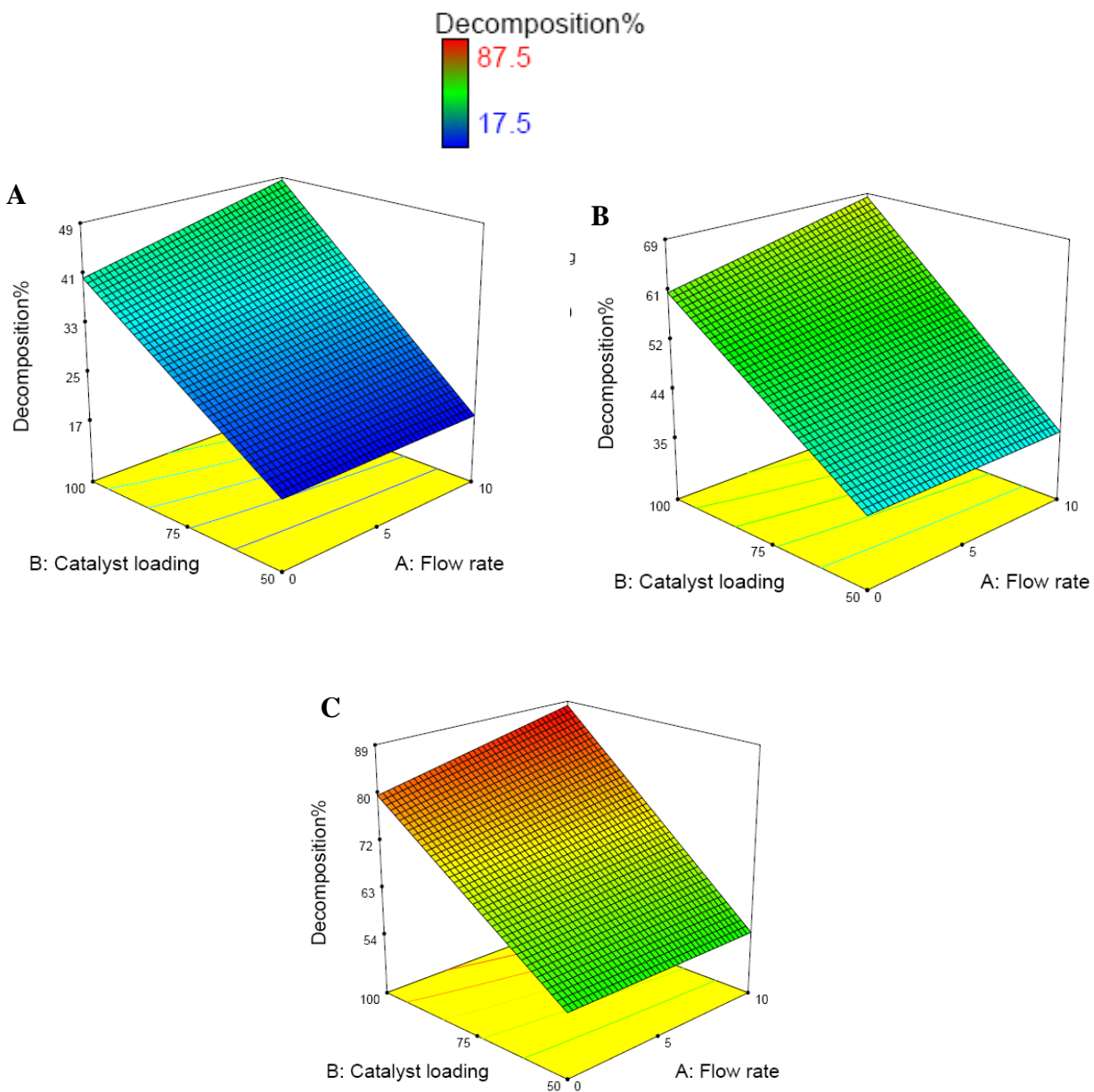


Figure 3-31. The 3D response surface plot of dye decomposition% of P25 as a function of the catalyst concentration and Flow rate under different light intensity. A) 2. B) 4. C) 6.

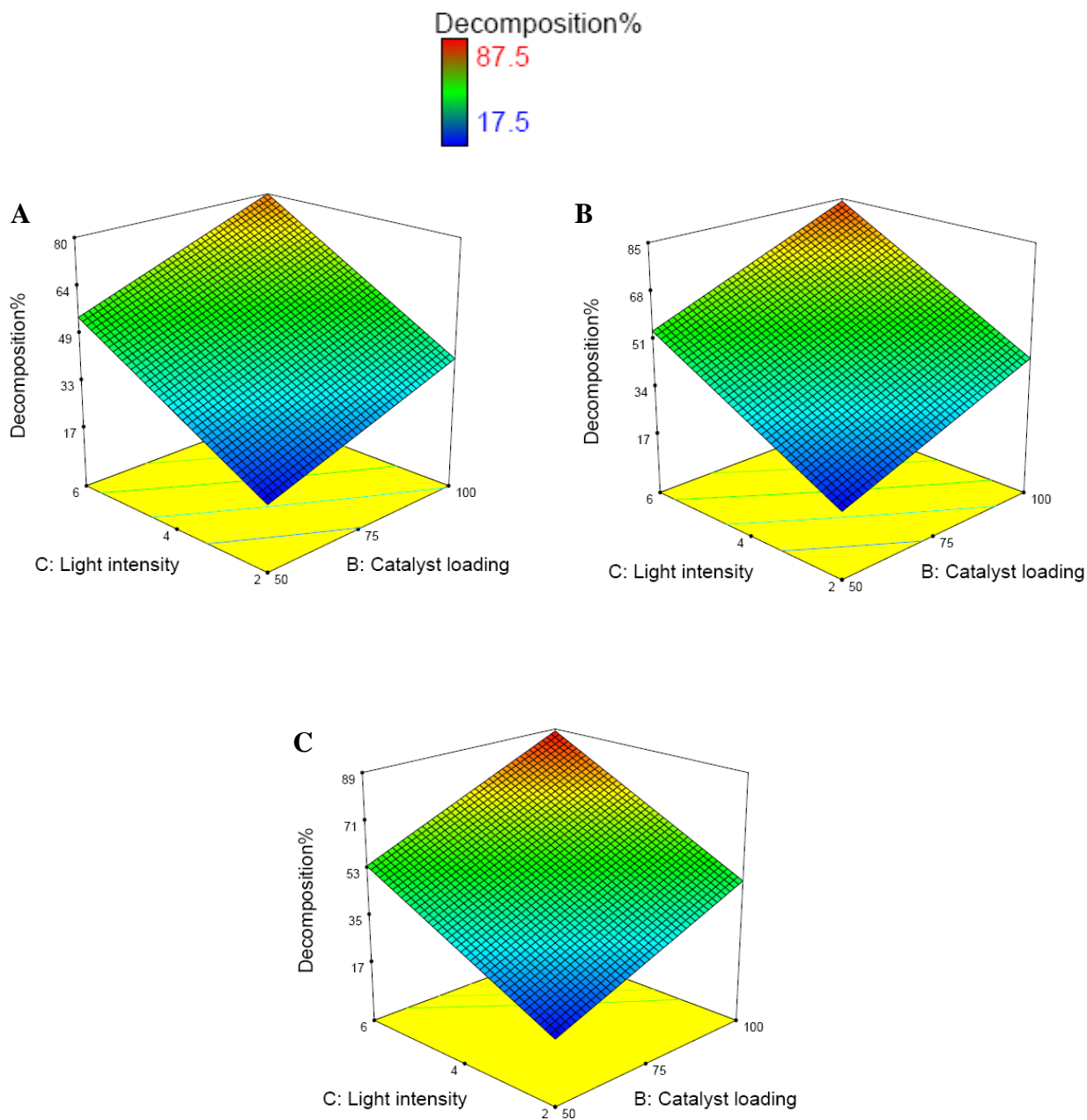


Figure 3-32. The 3D response surface plot of dye decomposition% of P25 as a function of the catalyst concentration and light intensity at different aeration rate. A) 0. B) 5. C) 10 ft³/hr.

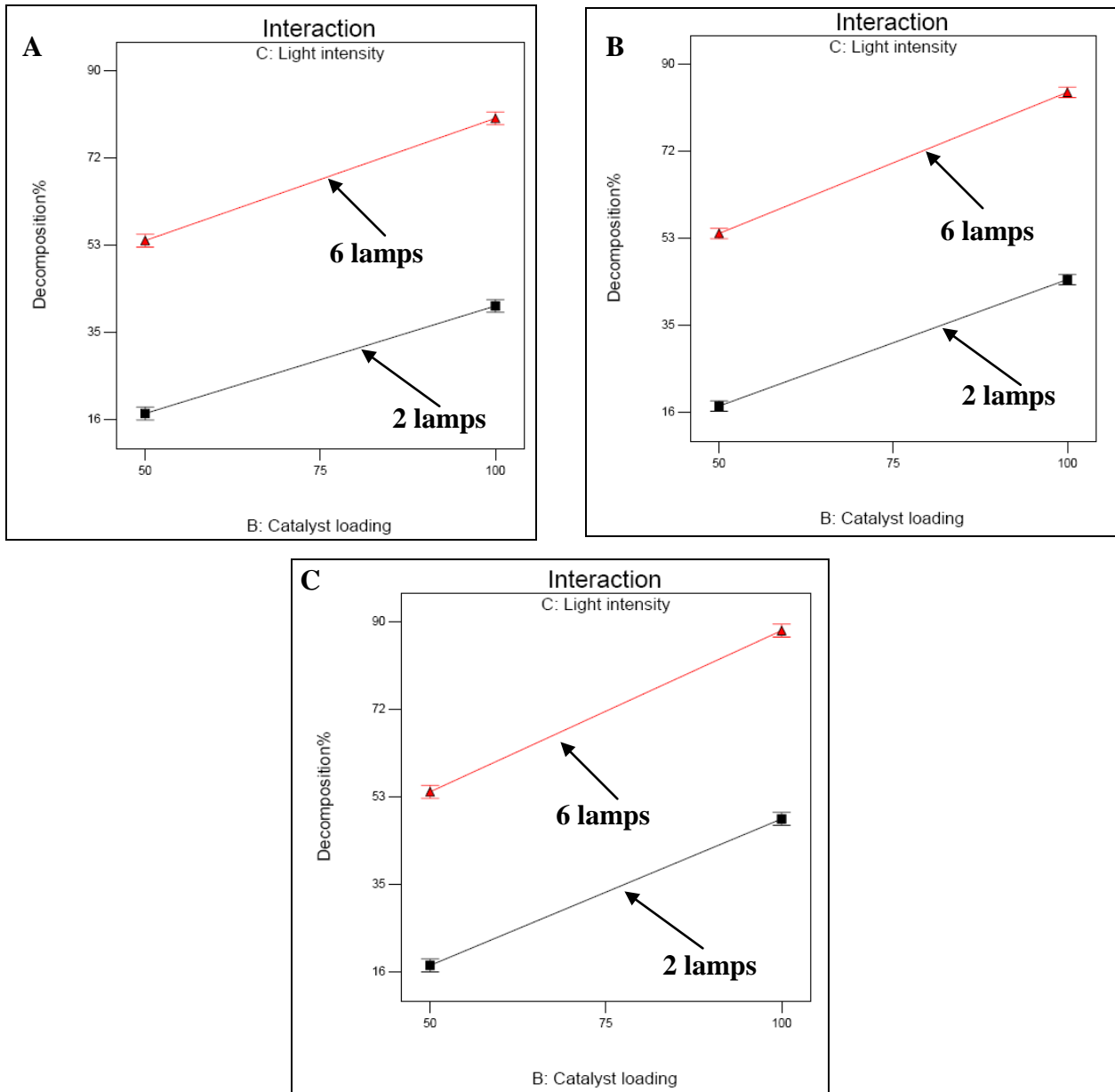


Figure 3-33. Interaction plot of response data against factor B for both levels of factor C at different aeration rate for P25. A) 0. B) 5. C) 10 ft³/hr.

CHAPTER 4
TRANSITION METAL DOPING OF TITANIA PARTICIELS AS VISIBLE
PHOTOCATALYSTS

Synthesis of Vanadium Doped Titania Flakes

Vanadium doped titania flakes were prepared by adding vanadium alkoxide (vanadium isopropoxide) to the precursor used to produce titania nanoflakes. According to the desired molar ratio of Vanadium/Titanium, the appropriate amount of vanadia precursor was mixed in the oil phase and vigorously stirred by a magnetic stirrer. The oil phase mixture for making vanadium doped samples looks more yellow than the precursor for making titania flakes an intrinsic indicator that it's optical properties are different. After two hours mixing, there were no individual particles or separate phases existing in the final mixture which indicates vanadium isopropoxide homogeneously dissolves in titanium isopropoxide and the hydrocarbon solvent. The same synthesis procedure for making titania flakes was used for making vanadium doped flakes. After cleaning and colleting the products, synthesized vanadium doped flakes in water appeared yellowish except for the 1 atomic% doped sample (Figure 4-1) which implied these samples may absorb visible light and therefore have distinct color change compared to pure titania flakes. After solvent exchanging with isopropanol alcohol, the nanoflakes were dried by a supercritical fluid drying process [111]. The following heat treatments were performed as the same manner in the programmable electric furnace. After calcinations, the yellow color became more pronounced for the calcined samples compared to the non-annealed samples (Figure 4-2).

Characterization of Vanadium Doped TiO₂ Flakes

Vanadium doping of titania has been reported as one of the most effective ways to extend the absorption edge of photocatalyst into the visible light range. Many researchers have investigated the optimum doping level of vanadium in TiO₂ with diverse results [137-141, 149].

The optimum doping concentration of vanadium has generally been reported as between < 1 atomic% to 5 atomic% depending to the synthesis method and the types of vanadium precursors. In order to study the effect of vanadium concentration on visible photocatalysis, vanadium doped titania flakes with three doping levels (1, 5, and 10 atomic%) were synthesized using the modified surface hydrolysis method. Like pure titania nanoflakes, the significant pearlescence occurred indicated a large percentage of high aspect ratio particles (Figure 4-1 and 4-2). Therefore, we could expect the majority of the vanadium doped samples were flakes. The low magnification optical microscopic (OM) images of series vanadium doped samples indicated flat particles with major dimension in micrometer range (Figure 4-3 and 4-4). The strong interference color could be correlated to very thin minor dimension. The flakes were further treated by calcination at 400 °C for 2 hours. The surface morphology of series synthesized and calcined vanadium doped titania flakes was investigated using SEM images, shown from Figure 4-5 to 4-8. The major diameter of the series vanadium doped flakes was found to be of the order of 1-10 μm (Figure 4-5 A to 4-8 A)), and the thickness of these flakes was approximately 40 nm (Figure 4-5 B to 4-8 B). Aggregation was not apparent when comparing these treated flakes with those obtained directly from synthesis. Moreover, the thickness of the calcined samples did not change with heat treatment. Both the synthesized and calcined vanadium doped flakes were transparent under the SEM. Vanadium was detected by Energy Dispersive X-ray Spectroscopy (EDX) coupled with the SEM images within the vanadium doped flakes (Figure 4-5 C and 4-8 C). The results showed that vanadium was successfully doped into titanium dioxide lattice using the current synthesis method up to 10 atomic% doping level. The silicon signal in the EDX spectra was from the flat silicon wafer substrate for depositing the flakes. Further chemical element mapping scanning of titanium, oxygen and vanadium signals are shown in Figures 4-5 D to 4-8 D. Vanadium existed mostly along the fringes of the flakes instead of evenly dispersing within

the whole particle. This is reasonable when considering the relatively low doping level of vanadium in samples.

Particle size distributions of the synthesized and calcined vanadium doped flakes were measured using laser diffraction (Figure 4-9). The measured major dimension of the flakes was similar to the dimensions obtained from the SEM images. The particle diameter statistics for series vanadium doped flakes are shown in Table 4-1. Unlike undoped titania samples, vanadium doped flakes have smaller diameters after synthesis. This may be attributed to the higher hydrolysis rate of vanadium precursor compared to that of titanium alkoxide. After heat treatment, the diameter does not decrease as much as the annealed titania samples. It has been reported that thermal stability of vanadium doped titania particles decreases as vanadium content increases [133,134]. Crystal structure changes of the vanadium doped flakes were identified by powder XRD (Figure 4-10 A). The XRD patterns of the synthesized and calcined vanadium doped flakes are found to correspond to the anatase phase. There is no indication of the presence of other titania phases such as rutile or brookite, and there are no vanadium oxides or vanadium pentaoxides detected. These results indicate that vanadium is evenly dispersed throughout the flakes most likely as a lattice substitution. Therefore, a vanadium doped flakes with single phase of anatase structure were successfully synthesized by this modified surface hydrolysis method. A slight shift of the (101) peak position from 25.67° of both undoped and 1 atomic% vanadium doped sample to 25.35° of 10 atomic% doped sample was observed using the slow scanning technique at the scanning rate of $0.01^\circ/\text{step}$ (Figure 4-10 B). This phenomenon suggested the larger lattice distortion caused by substitution of more vanadium ions into titanium position in titania, also observed by other researchers [107,135,136]. The average grain size of vanadium doped flakes was calculated by the Scherrer equation (equation 3-1). The grain size was determined from 8.7 to 10.2 nm for calcined 1 and 10 atomic% doped flakes respectively (Table

4-2). The crystallite size of vanadium doped flakes increases with increasing the doped vanadium concentration. The possible reason of this result is that vanadium is well known as a catalyst to facilitate the anatase phase transformation [106,108,133,134,137]. But the grain size of vanadium doped flakes is still within the range of optimum size for photocatalysis which is about 10-15 nm, therefore, excellent performance of photocatalysis might be expected using the vanadium doped flakes [114-116]. Apart from the crystallinity and grain size, specific surface area is one of the most important parameters which strongly influences the photocatalysis. Since the photocatalytic reaction mainly occurs at the surface of catalysts, materials possessing higher surface area are usually expected to be more photocatalytically active. According to the results of nitrogen sorption measurements shown in Table 4-3, there is a decrease in the specific surface area of catalysts with increasing the amount of vanadium doping. The diminution of specific surface area could be related to the raise of grain size when adding more vanadium in the synthesis, and corresponded well to the results of grain size calculation from the XRD measurements (Table 4-2). Similar results have been demonstrated for Manganese, Iron, and Vanadium doping by other investigators [100,138]. Degussa P25 was also used as our benchmark for visible photocatalysis comparison since some researchers claimed that it could decompose organic species under visible light irradiation [67,126]. All calcined vanadium doped flakes have ~3 times higher surface area than P25 (Table 4-3). The surface potential of the series calcined vanadium doped flakes were measured using the electrophoretic technology (Brookhaven Zetaplus), as shown in the Figure 4-11 A. The IEPs of the series calcined vanadium doped flakes shifted toward lower pH values with increasing vanadium concentration (Figure 4-11 B). Di Paola et al. observed the same behavior and found the surface Bronsted acid sites formed at the surface of the titania sample when adding appreciable amount of Mo, V, and W using the Fourier Transform Infrared Spectroscopy (FTIR) [139]. A similar trend was previously

observed for doped titania samples consisting of acidic oxides (Mo and V) and suggests that those oxides significantly increase the surface acidity by developing surface Bronsted acid sites [140]. From the dye adsorbing aspect, series vanadium doped samples had more negatively charges than P25 which could favor the dye loading at surface and hence the overall degradation efficiency (Figure 4-11 B). Therefore, both the surface properties of photocatalyst and photocatalytic efficiency could be manipulated by altering the amount of vanadium doping.

The optical properties of the vanadium doped flakes were determined by taking diffuse reflectance spectrum from the UV-Visible spectrometer coupled with an integration sphere (Figure 4-12). There is a clear “red shift” for calcined vanadium doped flakes when comparing to undoped titania flakes. The photoresponse extended into the visible region (400-700nm) with vanadium doping. And the extension of absorption edges is attributed to the charge transfer transition from the d-orbital of vanadium atom to the conduction band of titania. The band gap of vanadium doped flakes could be calculated from the diffuse reflectance spectrum which is listed in Table 4-4. Comparing to previous studies of vanadium doped titania [94,106,141-143], the same trend is shown in the shift of absorption band edge with increasing amount of vanadium dopant. Furthermore, a modified method was used to accurately measure the true absorption of photocatalyst particles in water in order to mimic the realistic of photocatalytic process (Figure 4-13) [123]. The range of band gap of the vanadium doped flakes is from 3.33 to 2.61 eV according to the amount of vanadium in samples (Table 4-4). Higher vanadium doping level of vanadium doped flakes tends to increase the optical absorption in the visible range. However, the absorption behavior seems to be changed when the doping level reached 10 atomic% (Figure 4-13 C). This phenomenon may be attributed to the chemical state of vanadium cations in the titania lattice. The absorption band in the visible light regime may be correlated to the generation of impurity levels created by both V^{5+} and V^{4+} states, which will be shown in the following X-

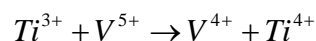
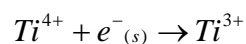
ray Photoelectron Spectrometer (XPS) spectrum (Figure 4-14). It has been reported that the absorption band of V^{5+} and V^{4+} cations were shown above and below 550nm respectively in the substitutional sites in anatase phasic titania [108,110,144]. Hence, the absorption band shifted the range of shorter wavelength when V^{5+} exists predominantly in the lattice site of titania (Figure 4-14 B). Except for the influence of optical absorption, the chemical state of vanadium cations also plays an important role in the visible light photocatalysis and will be discussed in the following section. In order to correlate the amount of dopant to the change of optical properties of vanadium doped flakes, the inductively coupled plasma mass spectrometry (ICP-MS) was used to analyze the concentration of vanadium in the catalyst. The results of absolute molar ratio of V/Ti were slightly lower than the nominal molar ratio which was directly calculated from the initial concentration of precursor (Table 4-4). These differences may be attributed to the error of volume measurement for initial precursor or difference in hydrolysis and condensation rate between titania and vanadia precursor and loss of vanadium during washing. The chemical state of vanadium species may have a stronger influence in visible light photocatalysis [106,141,145,146]. Therefore, detailed XPS spectra has been taken and discussed in the following section.

XPS Spectra of Series Vanadium Doped Flakes

The core level titanium 2p spectra for series vanadium doped samples (form 0 to 10 atomic% doping level) were shown in figure 4-15 A. Two distinct peaks at 458.5 and 464.2 eV were observed and recognized as Ti 2p_{3/2} and Ti 2p_{1/2} core electrons respectively for the pure titania sample [147-149]. When taking the spectra for the vanadium doped samples under the same conditions (the samples were prepared on the same mass basis), these two peaks shifted slightly with increasing amount of vanadium dopant. The binding energy of the titanium core electrons moved toward to higher energy about 0.4-0.5 eV for 1-10 atomic% vanadium doped

samples. An assumption of decreased electron charge density around Ti^{4+} due to vanadium doping could be drawn from these positive shift in binding energy of titanium signal [141]. Beside, an asymmetric part appearing near the Ti $2p_{3/2}$ peak, especially for higher vanadium doped sample (Figure 4-15 B), suggested a low energy shoulder corresponded to Ti^{3+} ion. The lower chemical state of Ti^{3+} ions occurs in vanadium doped samples were also reported by Robba *et al.* [150]. The interaction between dopant (vanadium) and matrix (titanium dioxide) explained why lower state titanium species were forming. In order to get more understanding of this result, a series of vanadium spectra were also taken from different samples (Figure 4-14). A wide range of V $2p_{2/3}$ peak from 517 to 522 eV for all samples were identified as V^{4+} and V^{5+} states respectively [106,146,150-157]. A increment of vanadium chemical state from +4 to +5 when adding more vanadium was observed (Figure 4-14 A) and has also been reported by many other researchers [106,141,145,146]. Therefore, the positive shifting of titanium 2p peak is reasonable because of changing of chemical state of vanadium. When the oxidation state of vanadium increased, the local electron density around the Ti^{4+} ion have to decrease at the same time to balance the total charge of material. Above is also evidence of vanadium ions incorporating into titania matrix instead of forming separate vanadia species. It should be noted that the intensity of V $2p_{2/3}$ signal did not change proportionally to the content of vanadium, which implied the discrepancy of vanadium concentration at surface and in bulk (Table 4-4). There are two important issues that should be addressed here: one is the formation of V^{4+} respected to the vanadium doping level and the other is the simultaneously positive shifting of titanium and vanadium signal for all vanadium doped samples. In the study of $\text{V}_2\text{O}_5/\text{TiO}_2$ catalysts, Trifiro *et al.* observed the same trend of change of chemical state of vanadium and proposed a scenario based on reduction of V^{5+} during annealing process [158]. Hermann *et al.* also reported the generation of tetravalent vanadium cations after calcined at 450 °C in the titania

matrix [159]. Both studies suggested the formation and incorporation of V^{4+} ions in the TiO_2 lattice were related to the dehydroxylation process. The possible mechanism could be demonstrated by the following reactions.



A high concentration of hydroxyl group was usually generated after the water based sol-gel method and therefore facilitated the above reduction reaction of pentavalent vanadium cations. However, the surface hydroxyl group detected by the XPS spectrometer for all vanadium samples (Figure 4-16) was roughly the same because of the similar synthesis process and specific surface area (Table 4-3). When the amount of vanadium dopant increased, more and more pentavalent ions were detected by the XPS spectrometer as a result of the depletion of surface hydroxyl group. Accordingly, the V^{5+} signal becomes stronger and stronger and predominate in the titania lattice when vanadium content is beyond 5 atomic%. As a result, lower chemical state of titanium species, Ti^{3+} , should appear owing to the coexistence of vanadium pentavalent cations and a weak shoulder that did present in all of the samples except for 1 atomic% vanadium doped flakes (Figure 4-15 B).

Experiment Apparatus

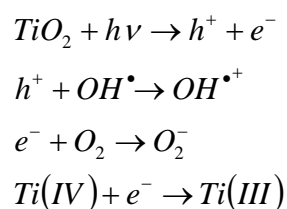
Dye decomposition experiments with vanadium doped samples were performed in a visible-light Pyrex reactor. The light source was a 300 W Xe-arc lamp (Varian Eimac Division, Light R-300) equipped with a power supply (Varian Eimac Division, model PS 300). For differentiating photocatalytic efficiency of visible and UV, a UV cutoff filter (< 400 nm) was placed between the light source and the dye solutions. 150 ml dye solutions were made with the same concentration used in the UV degradation experiments (50 μ M) and illuminated under

visible light without adding photocatalysts as the background. An Erlenmeyer flask contained dye solution with TiO₂ particles was placed inside the visible light reactor and continuously agitated by a magnetic stirrer. House air was delivered through a glass tube for investigating the aeration process. The amount/volume of input air flow was controlled by a rotary flow meter.

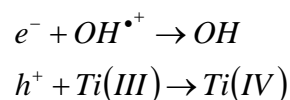
Photocatalytic Degradation of Dye Molecules under Visible Light Illumination

The photocatalytic activity of vanadium doped titania flakes under visible light irradiation was measured by the destruction of the dye molecules (methylene blue) in water with the above set-up. The following calculations of degradation rate were obtained by the experiment results after background subtraction following the same procedure of UV degradation tests in the previous chapter, vanadium doped titania flakes with three different vanadium doping levels were added to the reactor for studying the photocatalytic efficiency under only visible light irradiation. Figure 4-17 compares the photocatalytic activity of three vanadium doped samples by decomposition of the methylene blue dye solution under pure visible light illumination. Degussa P25 was also used as a reference material since some researcher claimed that it possesses some visible photocatalytic ability [67,126]. It was observed that calcined 1 atomic% vanadium doped titania flakes exhibited the highest photocatalytic efficiency on the degradation of methylene blue among three samples. Degussa P25 did not show any visible photocatalysis capability in this research. The Langmuir-Hinshelwood (L-H) model was again used to analyze the kinetics of dye degradation with visible light photocatalysis [16,20,127-131]. The linear transform of degradation curve was plotted as $-\ln(C/C_0)$ versus irradiation time and the rate constants were calculated from the slopes of Figure 4-19. The rate constants are shown in Table 4-5. The reaction with added turbulence presented a pseudo first order reaction and much higher efficiency especially for the flake systems (Figure 4-18).

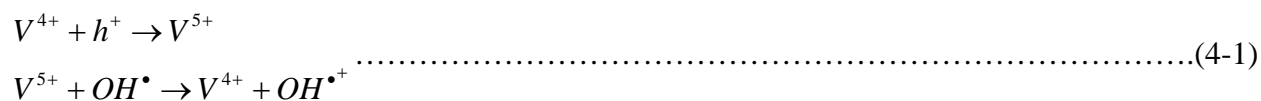
From the preliminary results, the amount of vanadium in the doped samples seemed to be the most important parameter for the visible light photocatalysis. Moreover, the vanadium concentration was also directly related to the chemical state of vanadium atom in the doped samples (Figure 4-14). Therefore, we expected that there could be a direct relationship between the chemical state of vanadium atom and visible photocatalytic processes. Bhattacharyya et al. proposed a possible mechanism to explain the effect of chemical state of vanadium on photocatalysis [141]. First of all, the common mechanism of titania photocatalysis were investigated by the laser flash photolysis method and illustrated as the following reactions:



And the main electron-hole pairs recombination processes were described as the followings:



At this moment, the nature of chemical state of vanadium ion played a role in the efficiency of the visible photocatalysis. The V^{4+} ions could be oxidized by the photogenerated holes and thus not only affect the charge transfer processes but also inhibit the undesired recombination reactions (equation 4-1).



Furthermore, the combination of above reactions leads to the formation of hydroxyl radical and then the following oxidation reaction in the common photocatalytic reaction. Accordingly, we could expect that the presence of V^{4+} ions could benefit the visible photocatalysis process. When

the vanadium species presented predominantly as the pentavalent ions in the doped sample, some of the tetravalent titanium ions must be reduced to trivalent titanium ions to maintain the charge balance of the system. This was also consistent with the results of XPS spectra in the Figure 4-15 B, a small shoulder represented Ti^{3+} ions for the 10 atomic% vanadium doped samples which had the highest concentration of V^{5+} ions (Figure 4-14 A). And the presence of trivalent titanium ions could promote the detrimental recombination process. Consequently, the higher the pentavalent vanadium ions presented in the sample, then lower the overall photocatalytic efficiency would be (Figure 4-20).

Statistical Design of Experiments

From the results of preliminary experiments (Figure 4-17 and 4-18), catalyst loading, and aeration process were determined to significantly affect the visible photocatalytic efficiency. Furthermore, the concentration of doped transition metal seemed to be one of the most important parameters. Therefore, the statistics design of experiments was again performed by using the Design Expert “7” software.

The investigated parameters in the design of experiments were A: bubbling flow rate (ft^3/hr), B: mass concentration of photocatalysts (ppm), and C: atomic concentration of vanadium (atomic %). A full 2^3 factorial design with three center points was used to obtain the developed model and estimated the experiment error. The detail of design of experiments is shown in Table 4-6. The results of visible photocatalysis with series vanadium doped flakes are shown as a 3D representation of design space (Figure 4-21). The best results for vanadium doped titania flakes could be seen using high level of catalyst loading, and flow rate but low level of vanadium doping. The complete degradation of dye could be found in the space which indicates that 1 atomic% vanadium doped flakes have the highest photocatalytic activity among the range of

concentration investigated in this research. The software generated model for vanadium doped titania flakes is described by equation 4-2.

$$\text{Dye degradation\%} = 50.05 + 3.84A (\text{Flow rate}) + 9.01B (\text{Catalyst loading}) - 32.81C (\text{Vanadium concentration}) - 1.44AB - 6.61BC \dots \dots \dots (4-2)$$

No doubt there is no obvious interaction between flow rate and vanadium concentration of sample and therefore no AC interaction term in this model. When the surface response of data is considered as the function of factor B and C; the surface was relatively flat, which suggested that there is only a small interaction between these two parameters (Figure 4-22). And the prompt increase occurred when factor C decreased, which indicated that the vanadium concentration is the most important parameter in the visible light degradation of dye solution. The amount of catalyst only contributed to limited enhancement when the vanadium doping was at the lower level regardless of the flow rate (Figure 4-23 and 4-24). The detailed argument of vanadium concentration was given in the previous section (Please see the preliminary part). Figure 4-25 shows the 3D surface response plot of series vanadium doped samples as the function of factor A and B. It is apparent that the amount of vanadium in the doped sample is the most significant parameter and inversely proportional to the dye decomposition percentage. Figure 4-26 A represents the contour plot with respect to the factor A and B, and Figure 4-26 B shows the response of 1 atomic% vanadium doped sample against factor A for different level of factor B. Increasing flow rate gives moderate improvement of overall efficiency for both different levels of catalyst loading. A similar trend is shown when the same plots were presented for 5 atomic% vanadium doped sample (Figure 4-27). However, the high vanadium doped sample does not follow the same track owing to the severe charge carrier recombination effect (Figure 4-28). In short, calcined 1 atomic% vanadium doped sample always had the highest performance within the whole investigation region. From the results of characterization, vanadium doped flakes with

three doping levels possessed very similar physical properties not only with each other but also with calcined undoped sample. Therefore, we could conclude that vanadium concentration of sample is the most important parameter for visible light photocatalysis from statistical perspective. The optimum doping level of vanadium doped flakes is identified as 1 atomic% within the investigated range of this study for vanadium doped flakes.

Table 4-1. Particle diameter statistics for series synthesized and calcined vanadium doped flakes.

Sample		D ₁₀ (μm)	D ₅₀ (μm)	D ₉₀ (μm)	Median (μm)	Standard Deviation (μm)
1 atomic% vanadium	Synthesized flakes	2.3	12.2	24.7	10.0	10.2
	Calcined flakes	1.3	7.8	16.3	6.3	6.3
5 atomic% vanadium	Synthesized flakes	2.2	10.1	24.3	7.5	10.7
	Calcined flakes	1.8	8.8	19.0	6.8	7.5
10 atomic% vanadium	Synthesized flakes	0.3	7.5	17.3	5.7	6.6
	Calcined flakes	0.2	4.2	9.7	3.3	3.6

Table 4-2. Grain size calculation by the Scherer equation for series calcined vanadium doped nanoflakes.

Sample	B (degree)	θ_B (degree)	d (nm)
1 atomic% vanadium doped flakes	1.04	25.63	8.7
5 atomic% vanadium doped flakes	0.93	25.51	9.2
10 atomic% vanadium doped flakes	0.80	25.35	10.2

Table 4-3. Physisorption measurements of P25, and series calcined vanadium doped titania nanoflakes.

Sample	Specific surface area (m^2/g)	Specific pore volume (cm^3/g)
Calcined 1 atomic% vanadium doped flakes	156	0.492
Calcined 5 atomic% vanadium doped flakes	152	0.487
Calcined 10 atomic% vanadium doped flakes	132	0.467
P25	49	—

Table 4-4. V/Ti molar ratio and band gap energy of series vanadium doped samples.

Expected V/Ti (atomic%)	V/Ti in bulk (atomic %)		Band gap (eV)
	Expected ¹	Measred ²	
0	0	0	3.33
1	1	0.92	2.91
5	5	4.82	2.73
10	10	9.79	2.61

Table 4-5. Pseudo-first order rate constants of methylene blue under visible photocatalytic degradation.

With bubbling treatment	
Sample	k_{pseudo} (10^{-4} min^{-1})
P25	3
Calcined 1 atomic% vanadium doped flakes	115
Calcined 5 atomic% vanadium doped flakes	70
Calcined 10 atomic% vanadium doped flakes	27

Table 4-6. The 2^3 factorial design used to investigate the most important factors for visible light photocatalysis.

Factor 1 A: Bubbling flow rate (ft^3/hour)	Factor 2 B: Catalyst loading (ppm)	Factor 3 C: Vanadium concentration (atomic%)
- (0)	- (50)	- (1)
- (0)	- (50)	- (1)
- (0)	+ (100)	- (1)
- (0)	+ (100)	- (1)
+ (10)	- (50)	+ (10)
+ (10)	- (50)	+ (10)
+ (10)	+ (100)	+ (10)
+ (10)	+ (100)	+ (10)

*Center point: A (flow rate): 5; B (catalyst loading): 75; C (vanadium concentration): 5

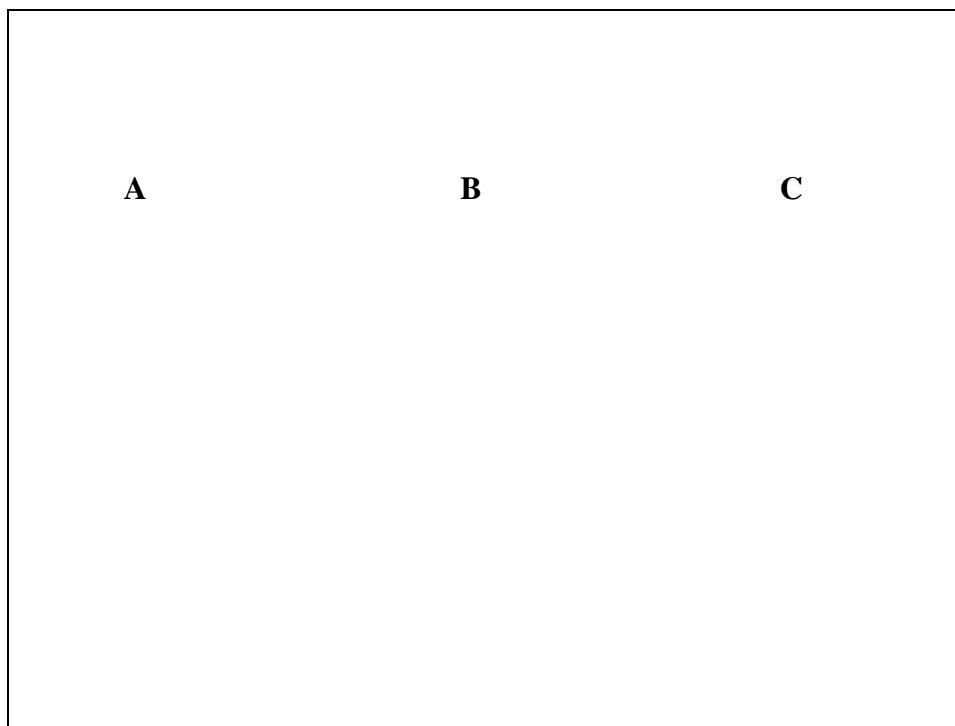


Figure 4-1. Photographs of synthesized vanadium doped titanium dioxide flakes. A) 1. B) 5. C) 10 atomic% vanadium (note the pearlescence of the samples).

A **B** **C**

Figure 4-2. Photographs of calcined vanadium doped titanium dioxide flakes. A) 1. B) 5. C) 10 atomic% vanadium (note the pearlescence of the samples).

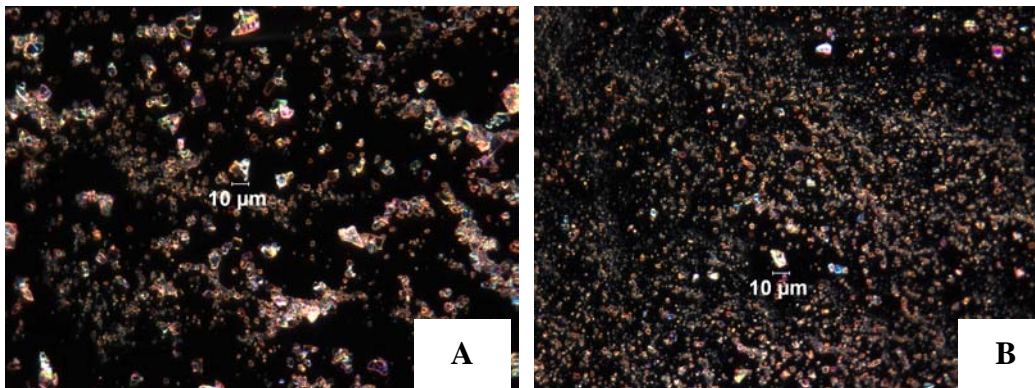


Figure 4-3. Optical micrographs of vanadium doped titanium dioxide flakes. A) synthesized. B) calcined 5 atomic% vanadium doped flakes.

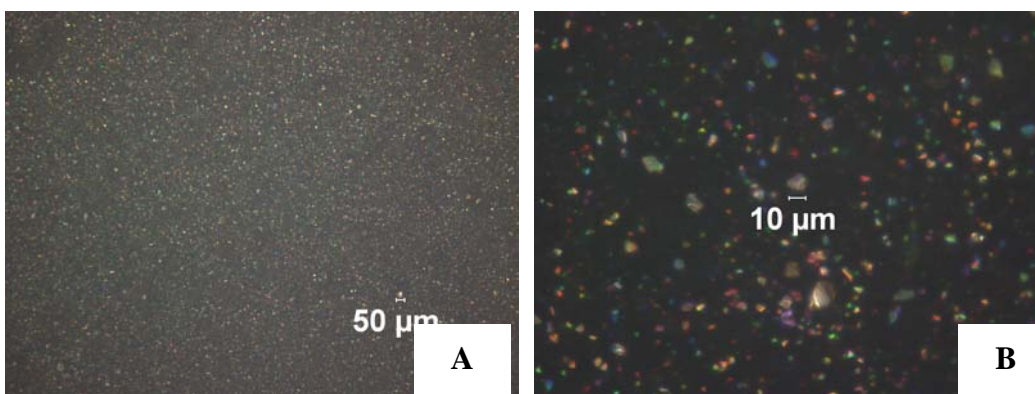


Figure 4-4. Optical micrographs of calcined vanadium doped flakes. A) 1. B) 10 atomic% vanadium.

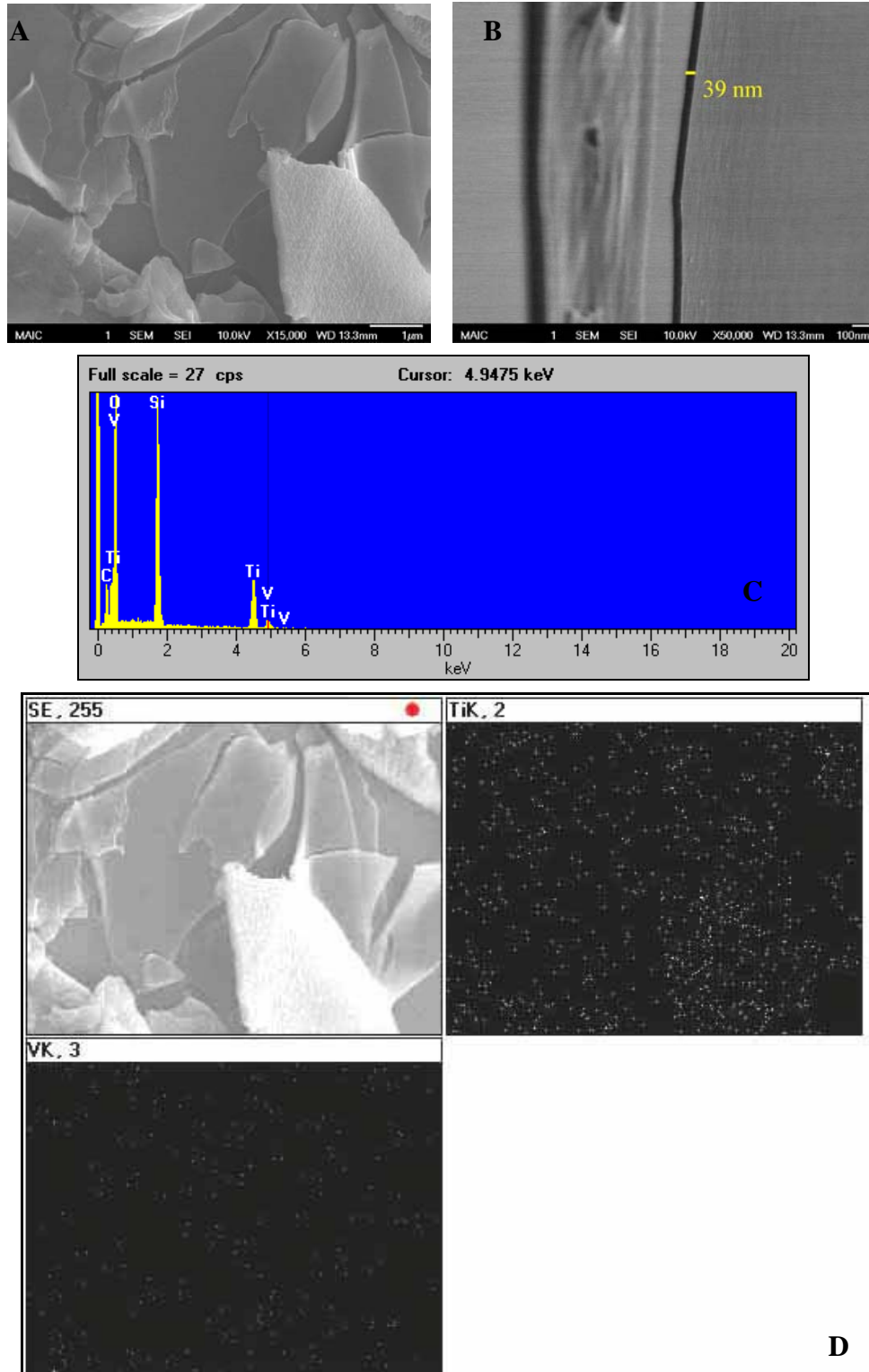


Figure 4-5. SEM images of synthesized 5 atomic% vanadium doped titania nanoflakes. A) surface morphology. B) thickness. C) EDX. D) mapping.

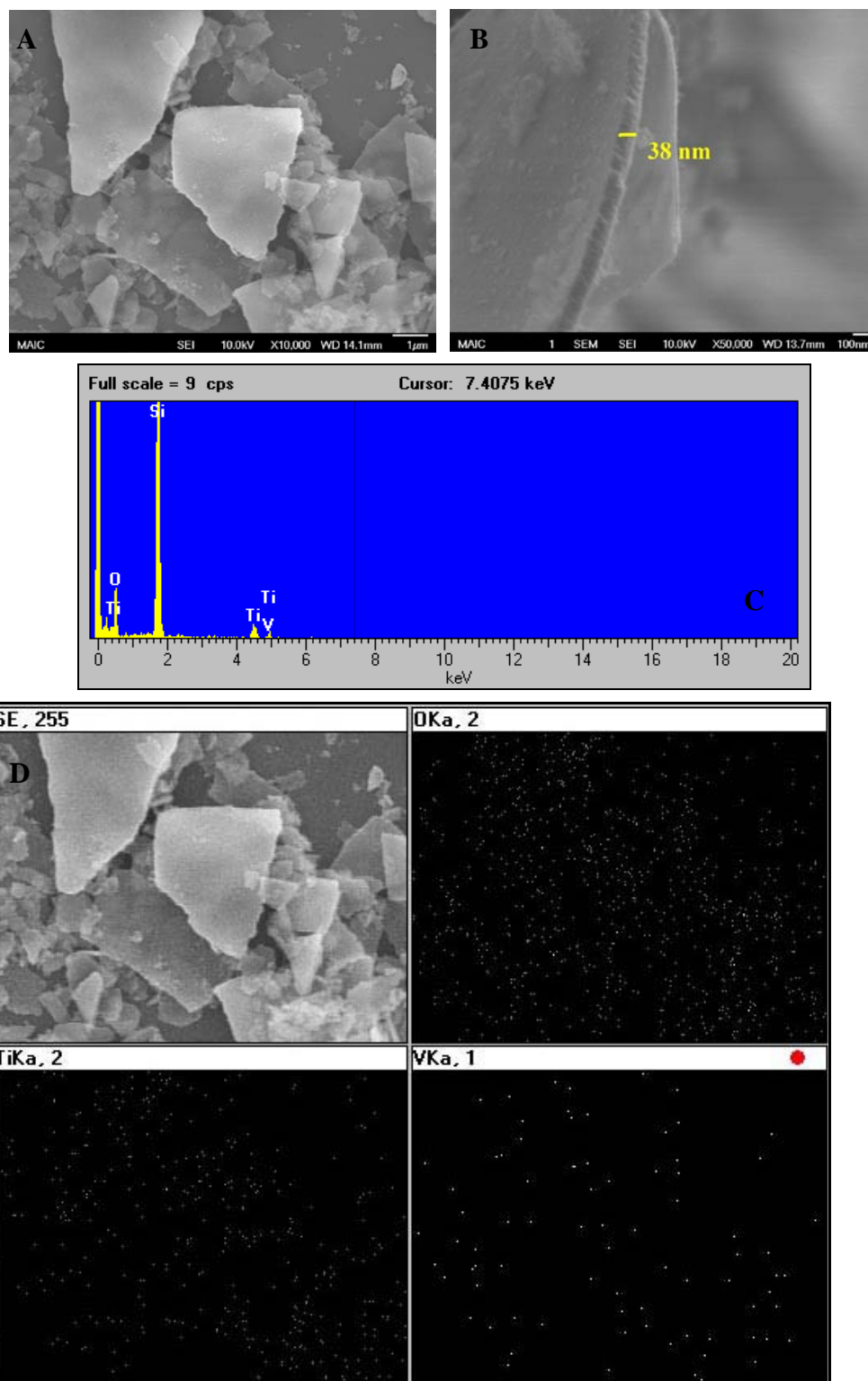


Figure 4-6. SEM images of calcined 5 atmoic% vanadium doped titania nanoflakes. A) surface morphology. B) thickness. C) EDX. D) mapping.

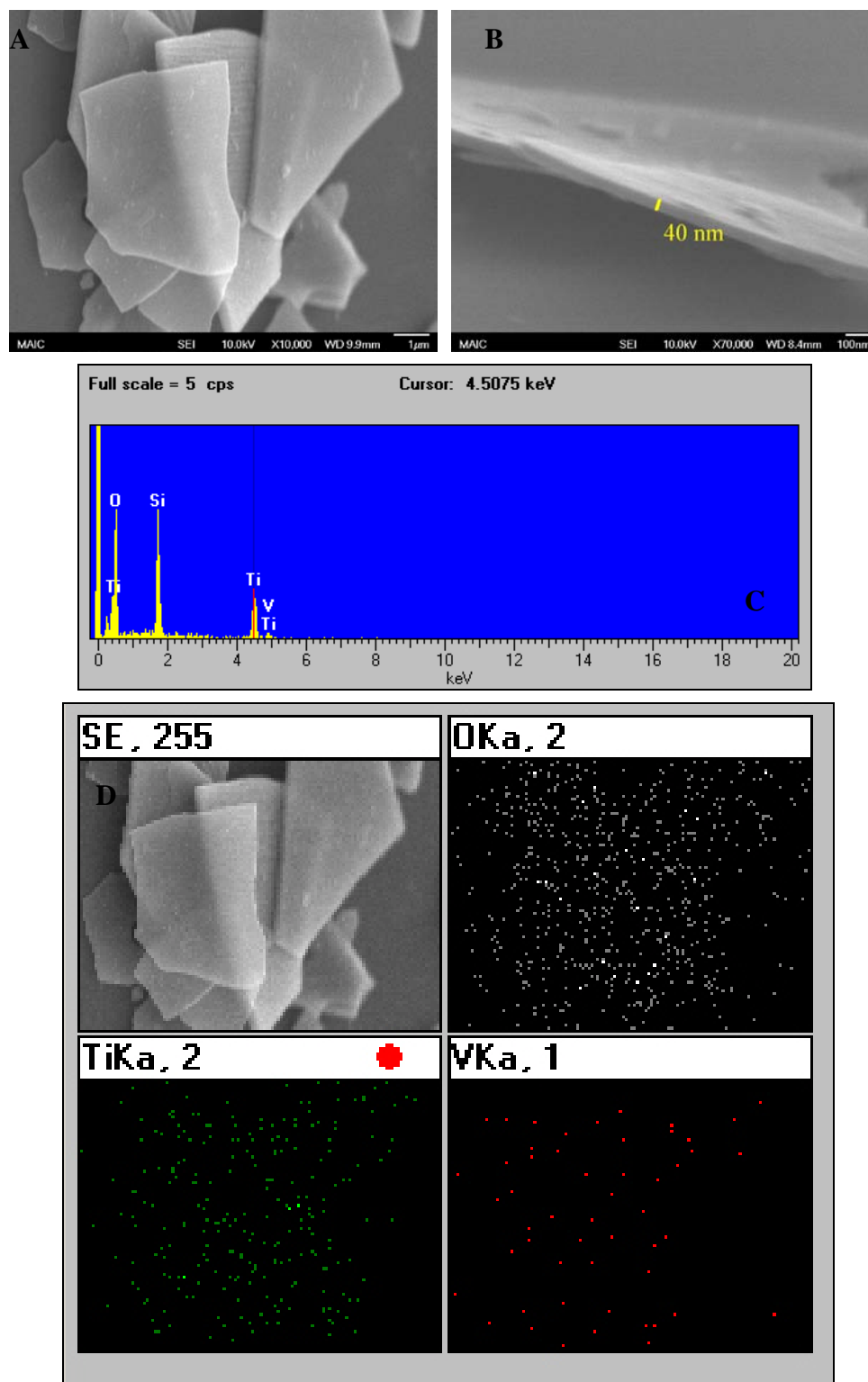


Figure 4-7. SEM images of calcined 1 atomic% vanadium doped titania nanoflakes. A) surface morphology. B) thickness. C) EDX. D) mapping.

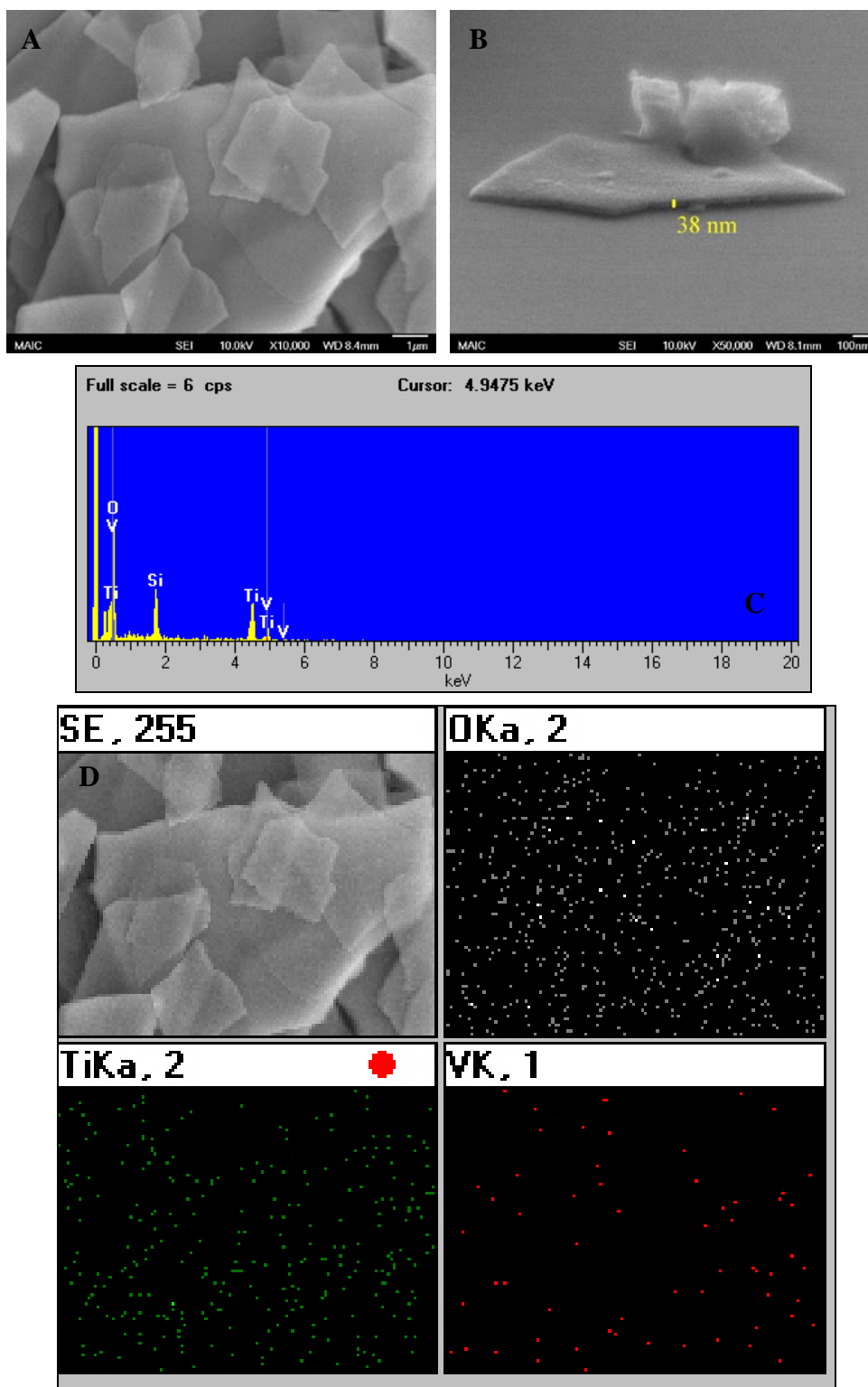


Figure 4-8. SEM images of calcined 10 atomic% vanadium doped titania nanoflakes. A) surface morphology. B) thickness. C) EDX. D) mapping.

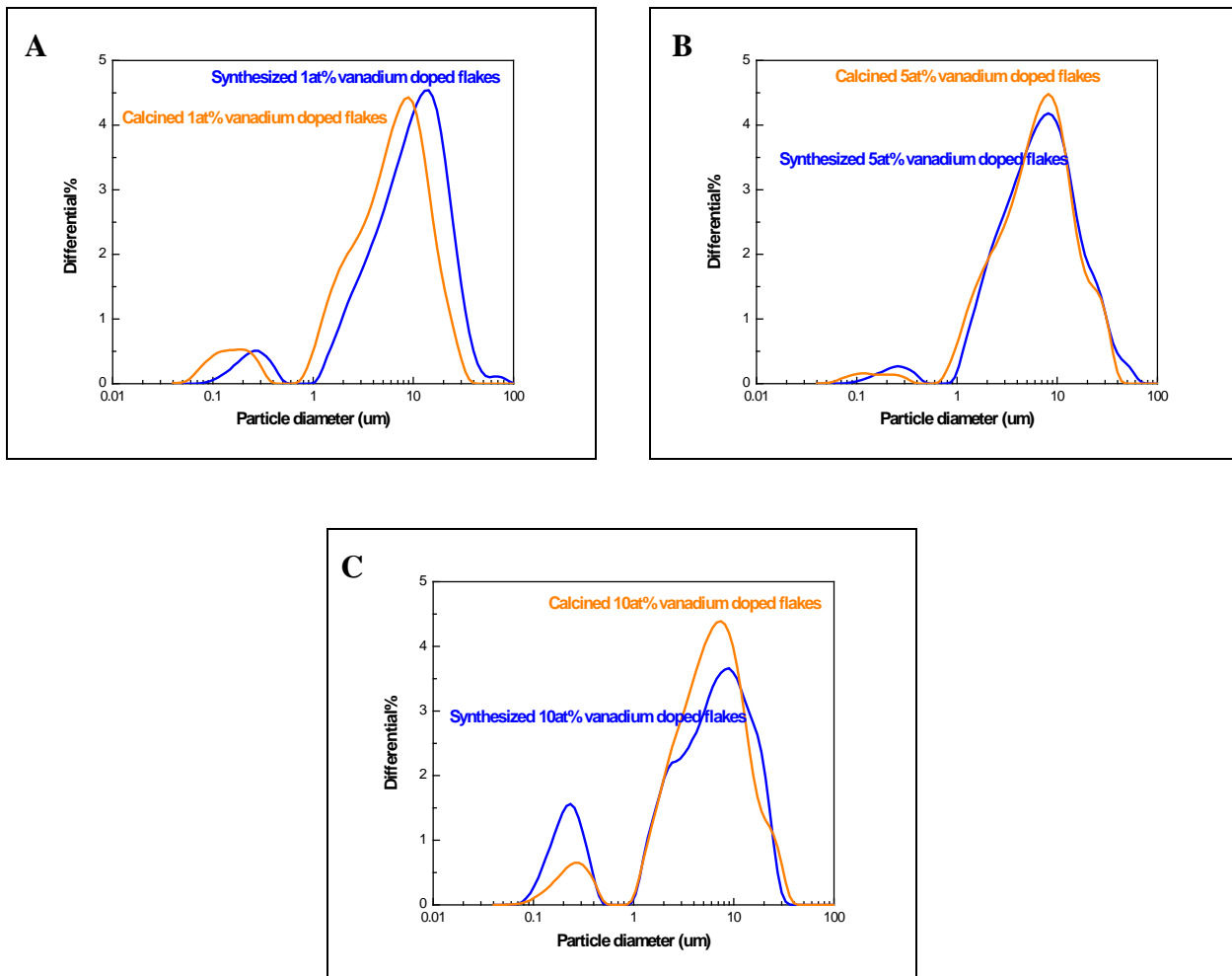


Figure 4-9. Volume based particle size distribution for synthesized and calcined vanadium doped flakes. A) 1. B) 5. C) 10 atomic% vanadium.

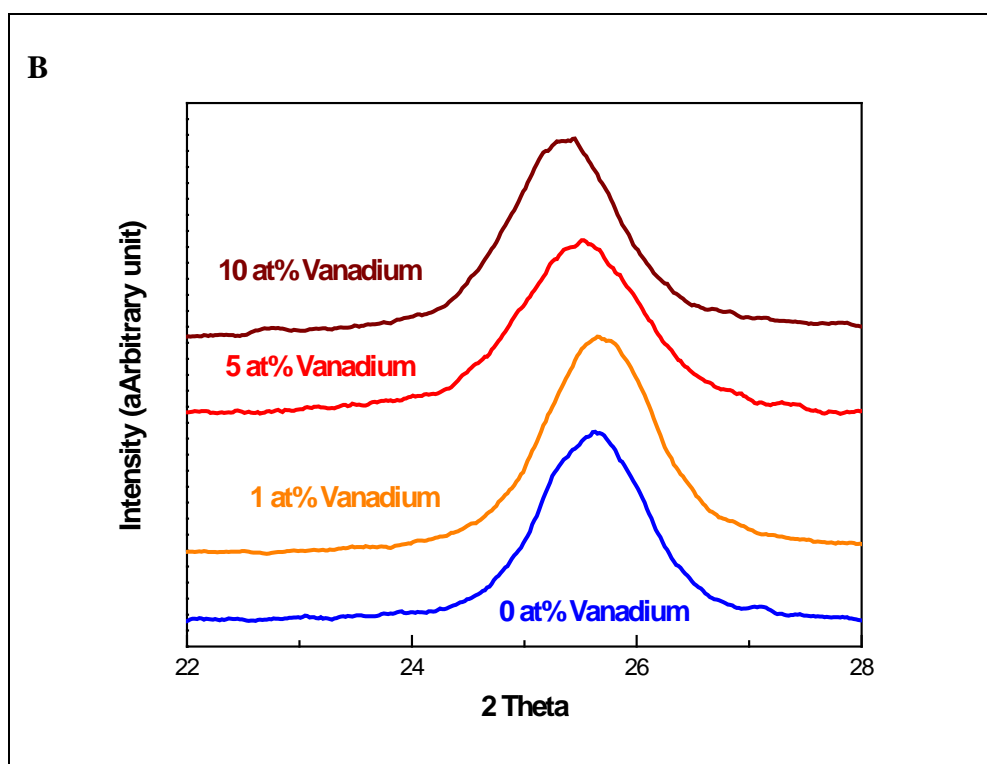
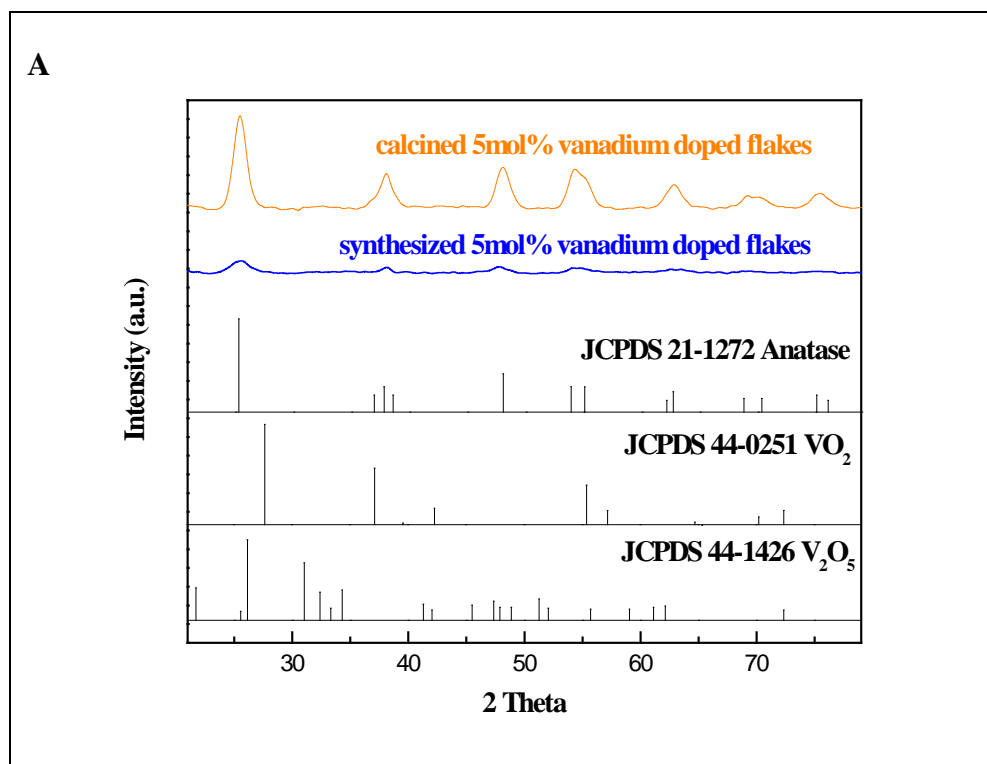


Figure 4-10. XRD patterns of vanadium doped flakes. A) 5 atomic% vanadium. B) Anatase (101) peak for series calcined vanadium doped flakes (at slow scanning mode: 0.01 °/step).

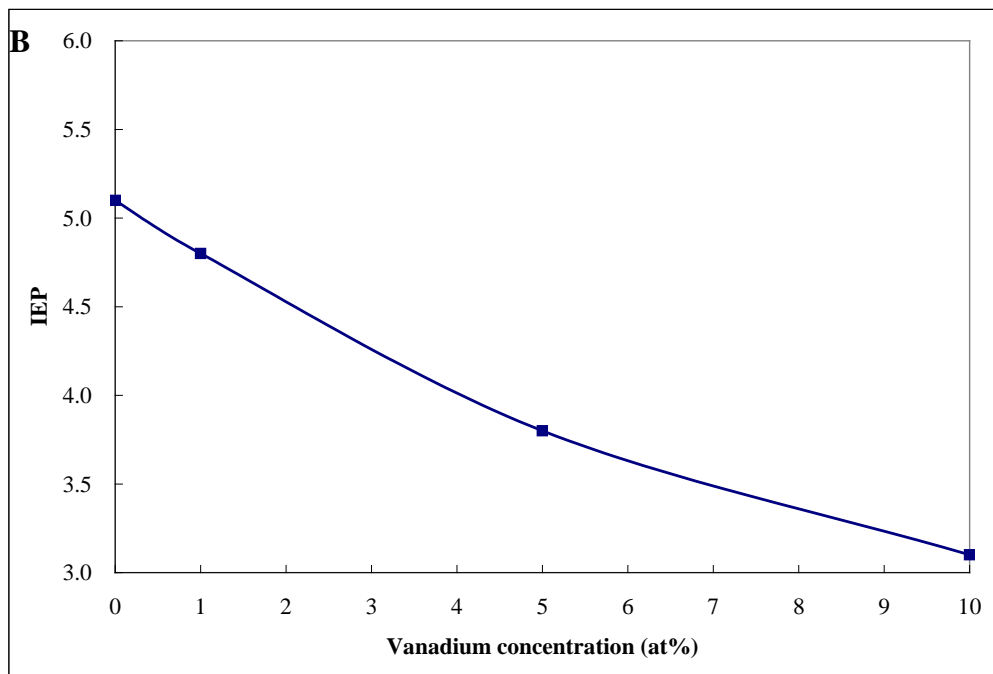
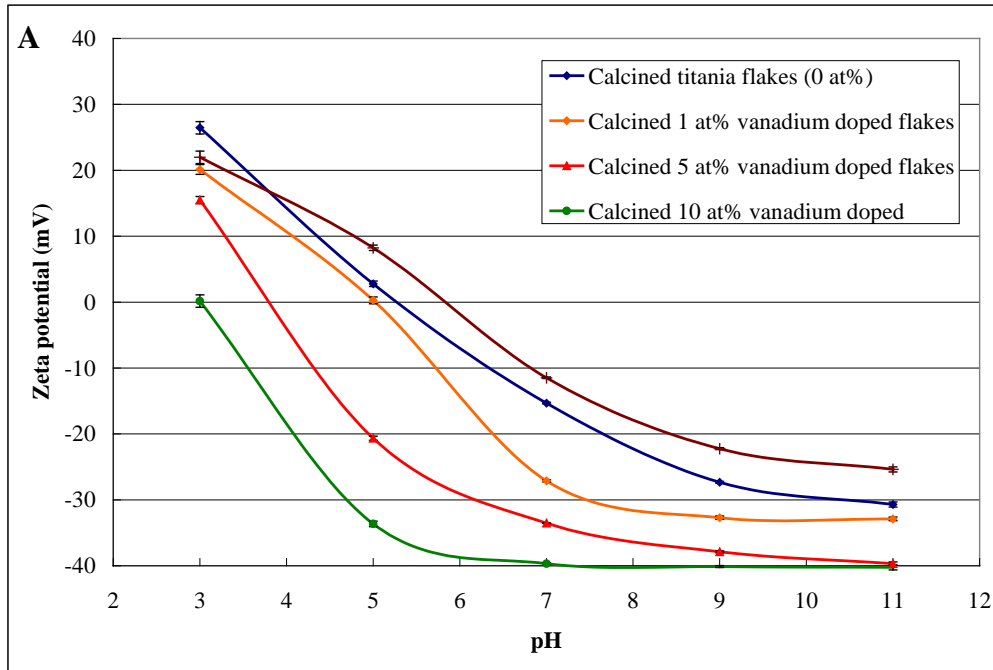


Figure 4-11. Zeta potential of the vanadium doped flakes as the function of pH. A) 0, 1, 5, 10 atomic% vanadium B) The IEP versus the amount of vanadium in the series vanadium doped flakes.

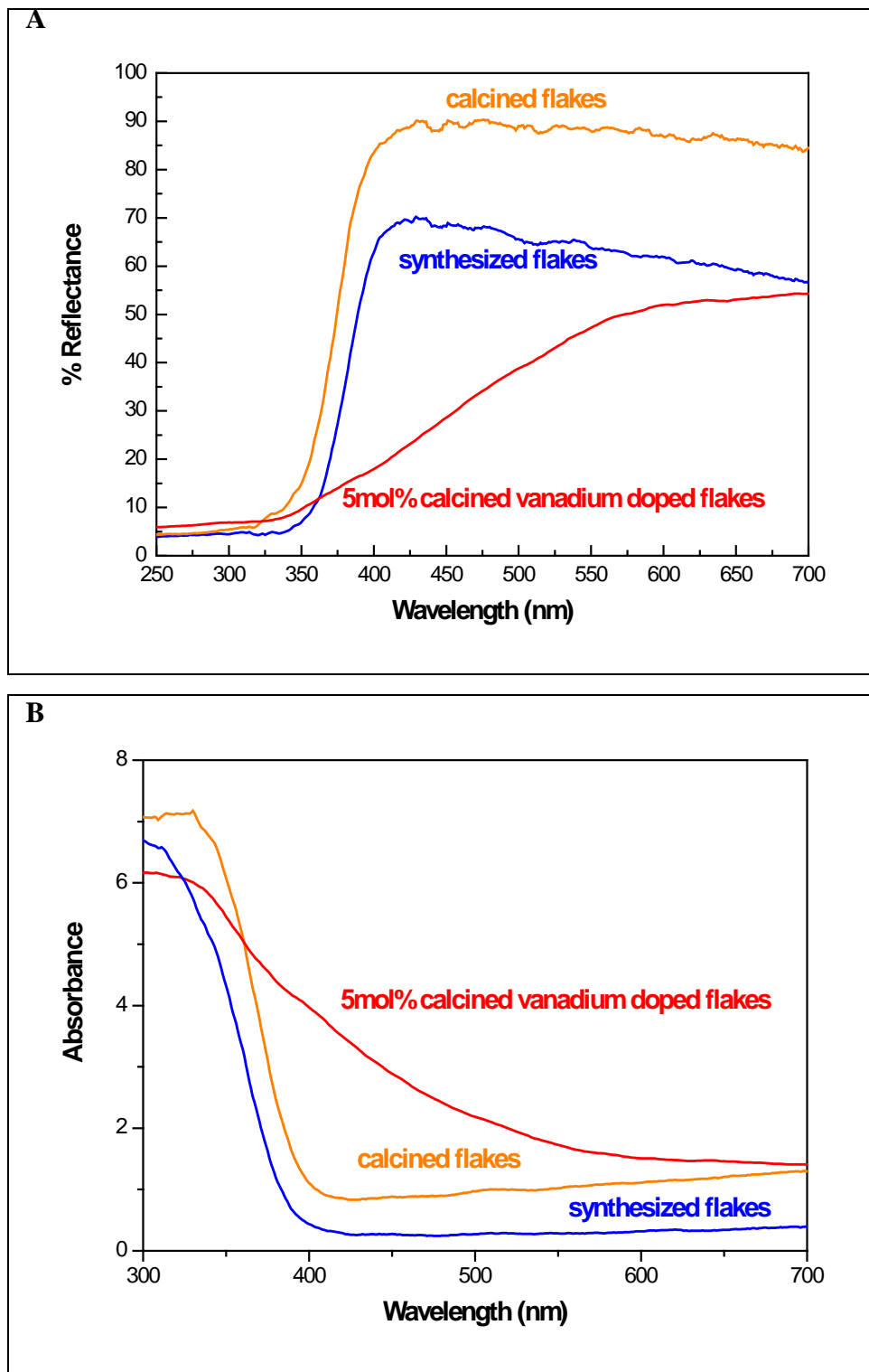


Figure 4-12. Diffuse reflectance spectra of vanadium doped titania flakes. A) 5 atomic% vanadium. B) the absorbance spectra for synthesized and calcined vanadium doped titania flakes.

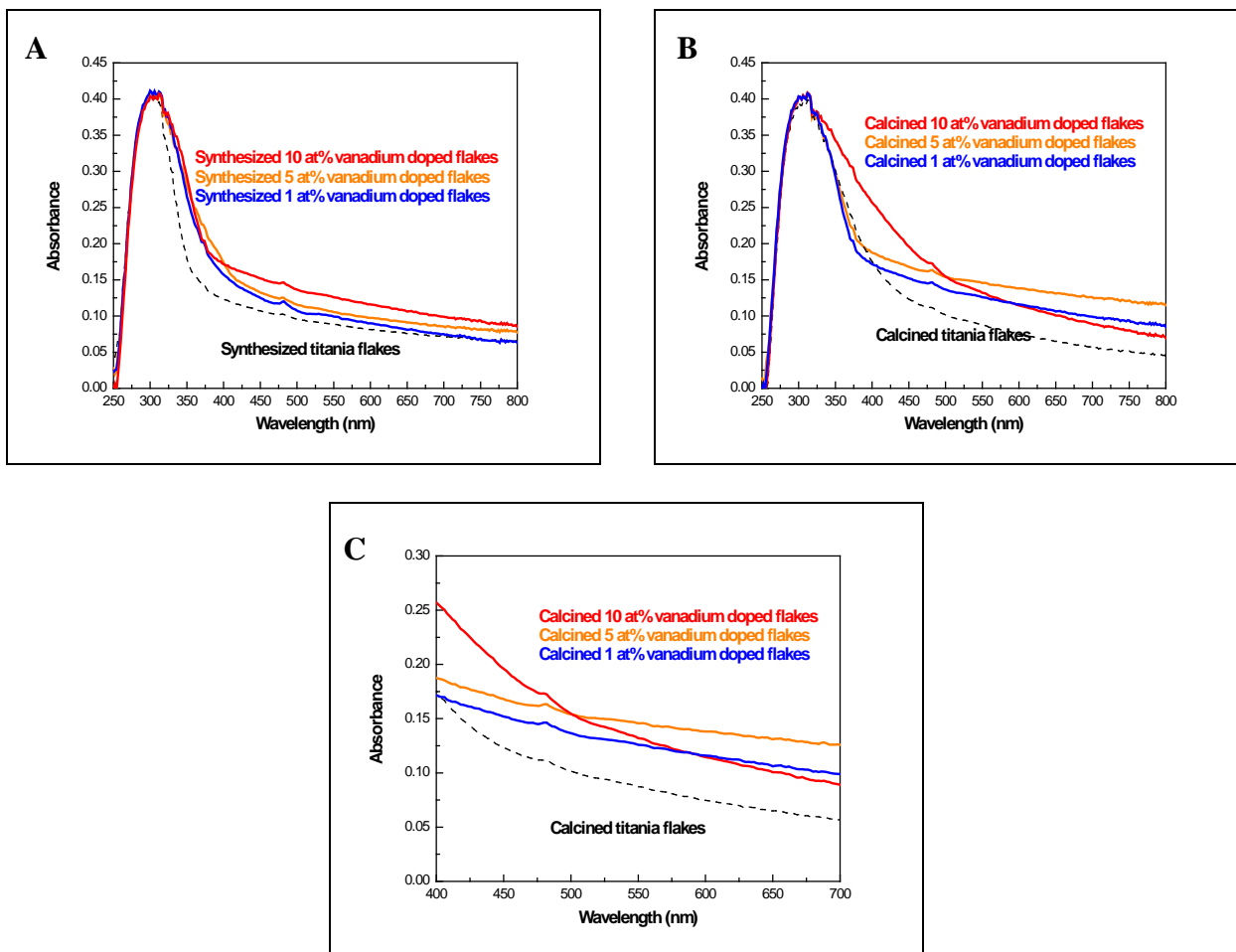


Figure 4-13. The true absorption spectra of vanadium doped flakes. A) series synthesized vanadium doped flakes. B) series calcined vanadium doped flakes. C) photoresponse of series vanadium doped flakes in the visible range.

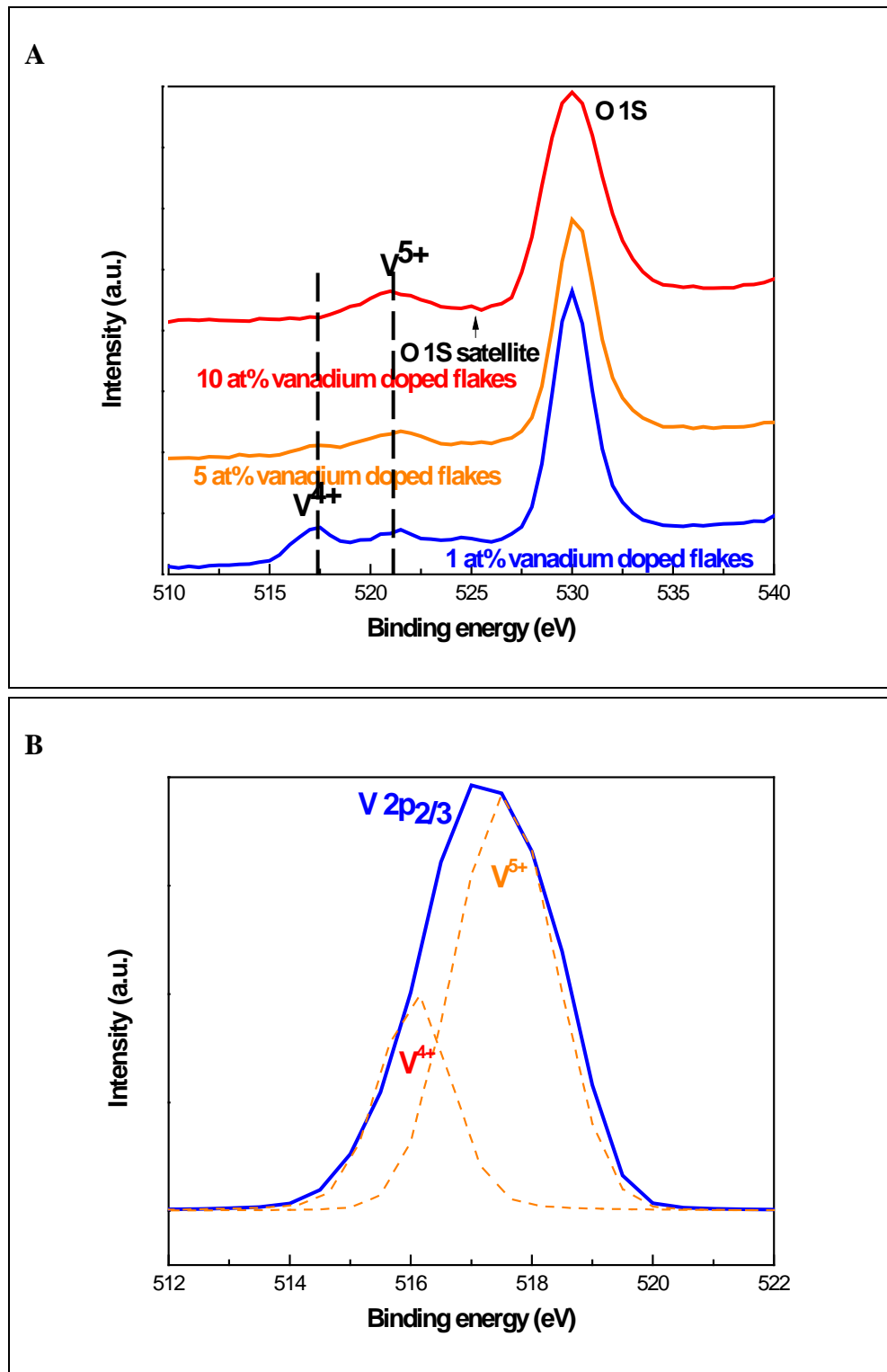


Figure 4-14. XPS spectra of vanadium doped flakes. A) O 1s and V 2p_{3/2} peaks for series vanadium doped flakes (b) V 2p_{3/2} peak of 10 atomic% vanadium doped flakes.

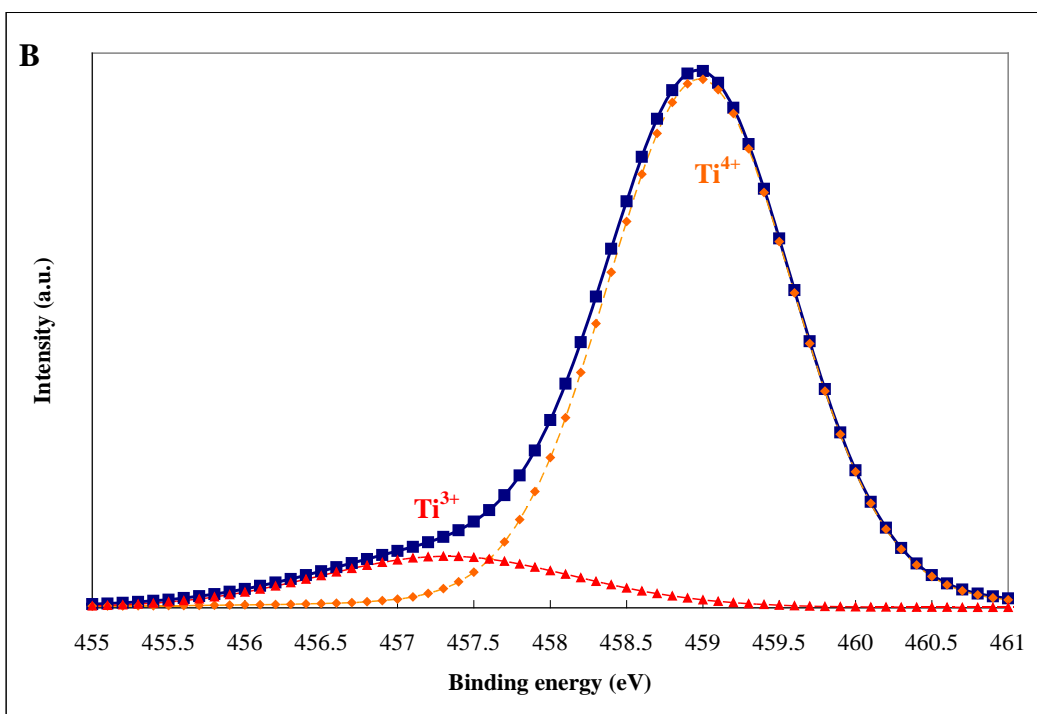
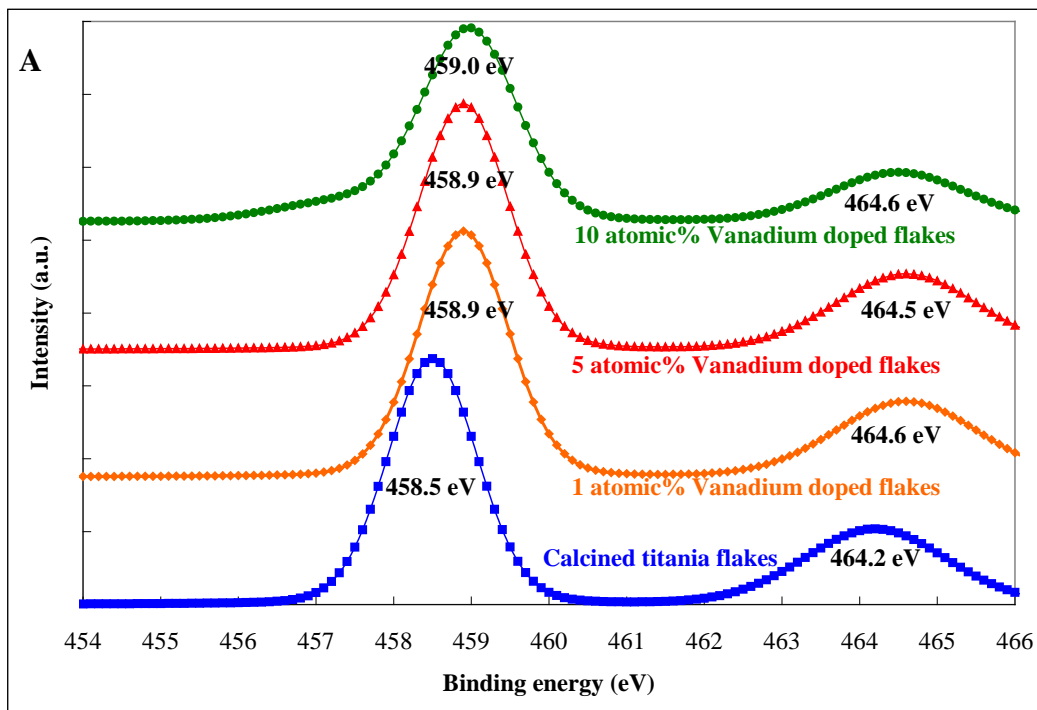


Figure 4-15. XPS spectra of Ti 2p_{3/2} and Ti 2p_{1/2} peaks for vanadium doped flakes. A) series vanadium doped flakes. B) Ti 2p_{3/2} peak of 10 atomic% vanadium doped flakes.

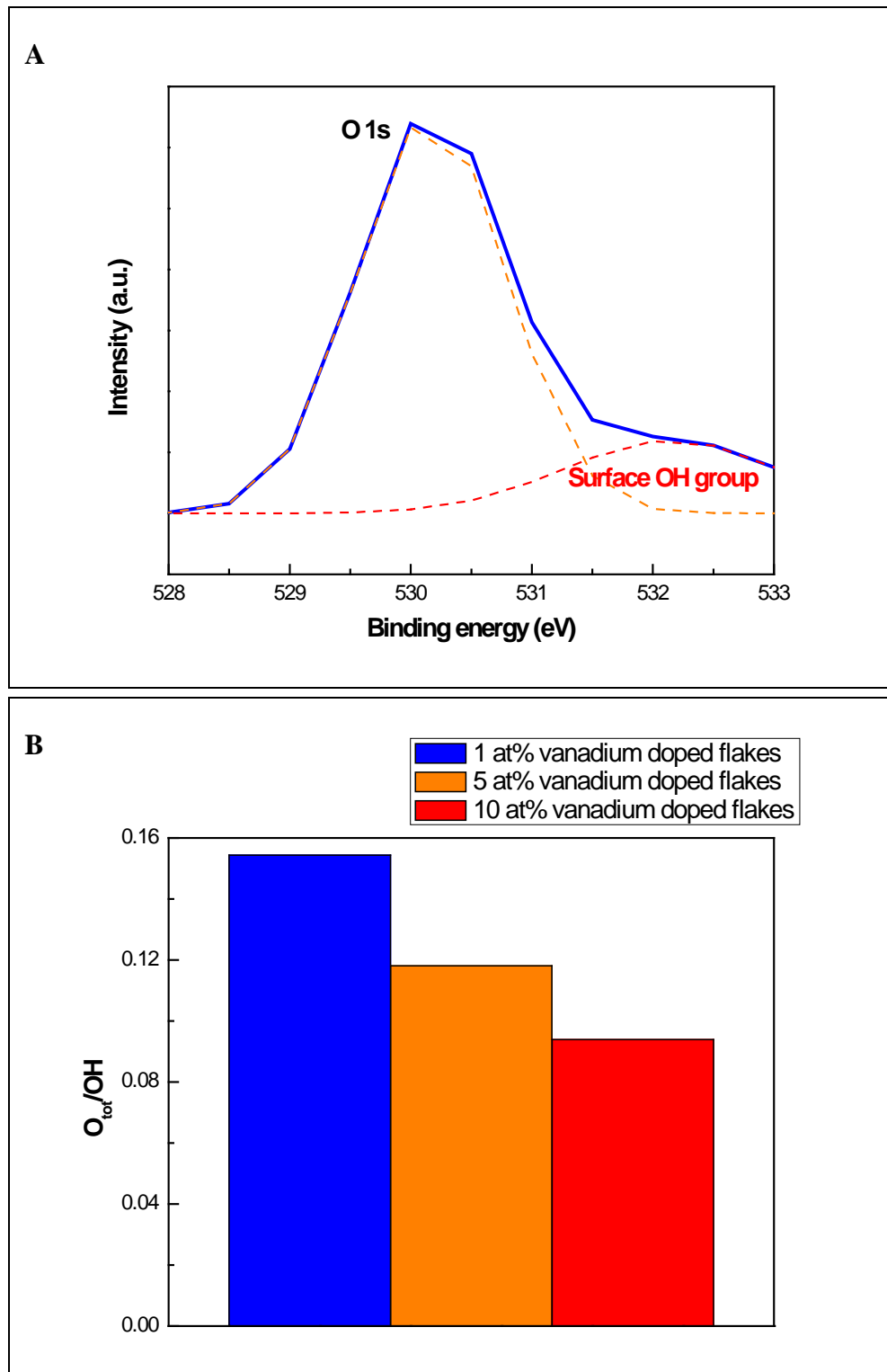


Figure 4-16. XPS spectra of O 1s peak fitting. A) 1 atomic% vanadium doped flakes. B) Surface ratio of OH/O_{tot} XPS signal for series vanadium doped flakes.

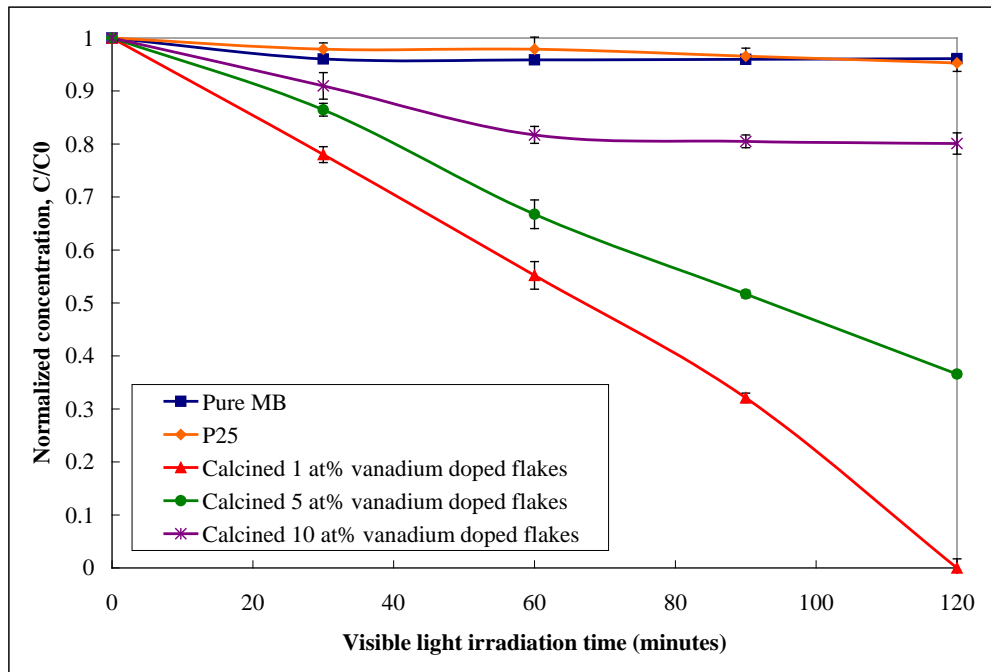


Figure 4-17. Visible photocatalytic decomposition of methylene blue by using vanadium doped titania flakes with three vanadium doping levels under bubbling condition.

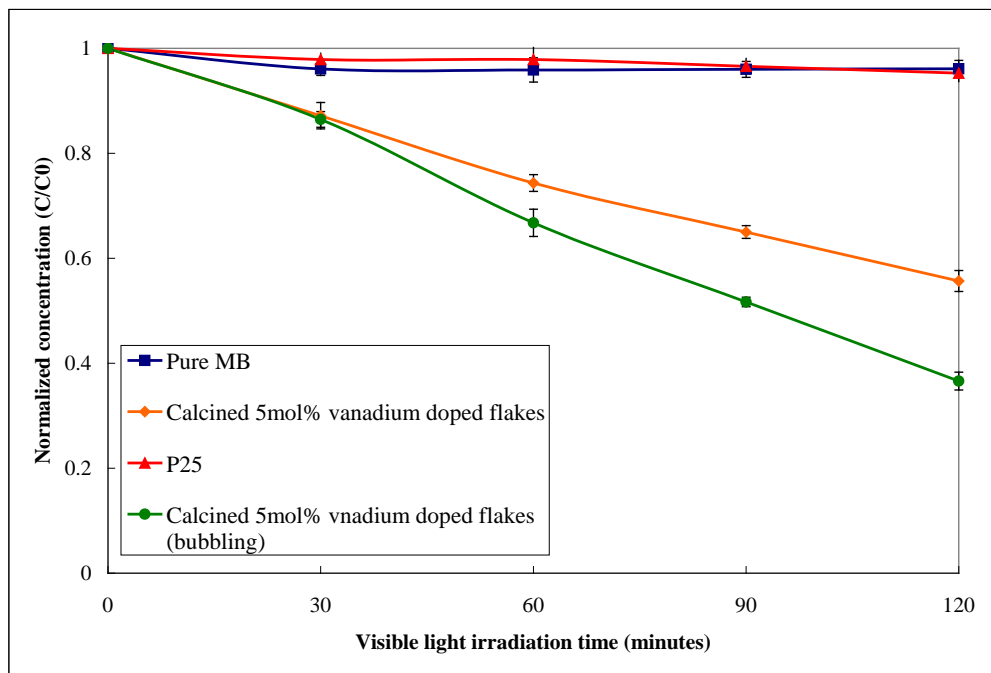


Figure 4-18. Linear transforms $-\ln(C/C_0)$ vs. time for methylene blue decomposition for vanadium doped titania flakes with three vanadium doping levels under bubbling.

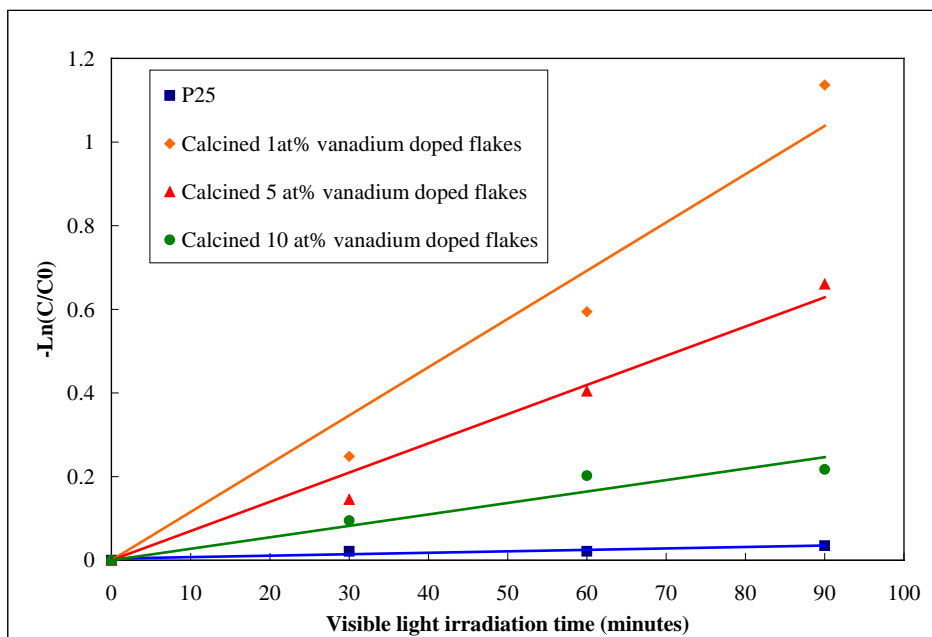


Figure 4-19. Linear transforms $-\ln(C/C_0)$ vs. time for methylene blue decomposition for vanadium doped titania flakes with three vanadium doping levels under bubbling condition. (Note the difference in scales of the normalized concentrations).

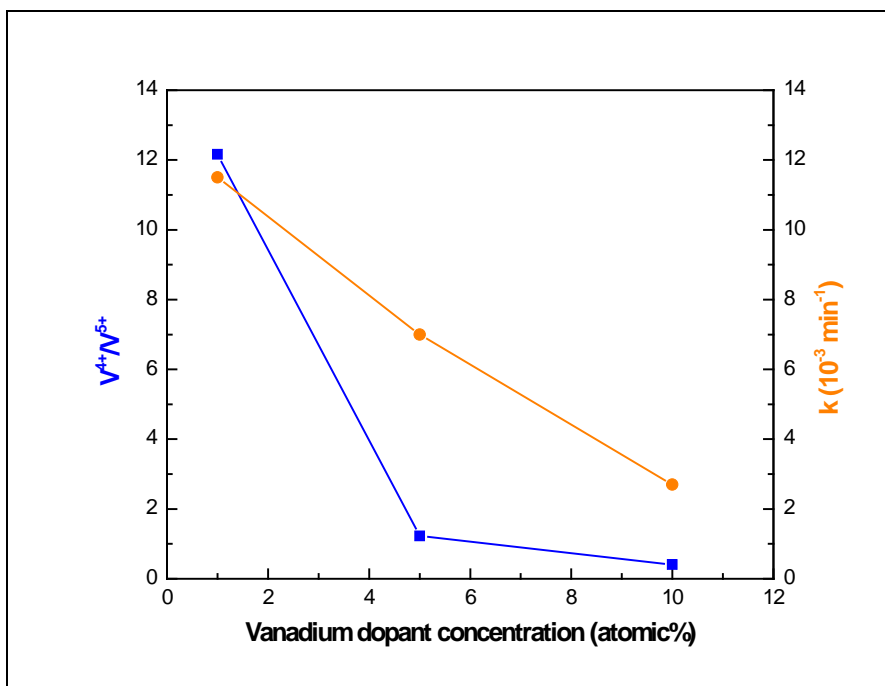


Figure 4-20. Comparison of the ratio of V^{4+}/V^{5+} and photocatalytic reaction rate for series vanadium doped flakes.

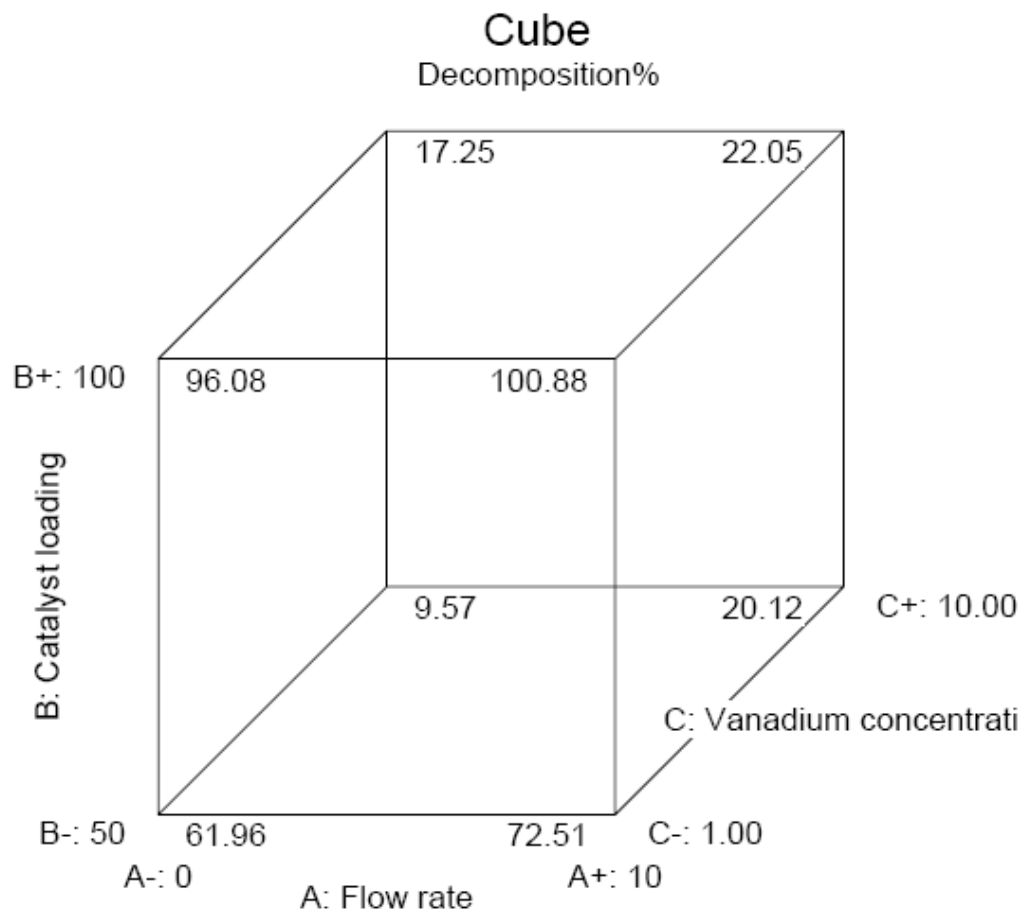


Figure 4-21. Experimental design visible light decomposition% results of vanadium doped titania flakes photocatalysis with three different doping levels.

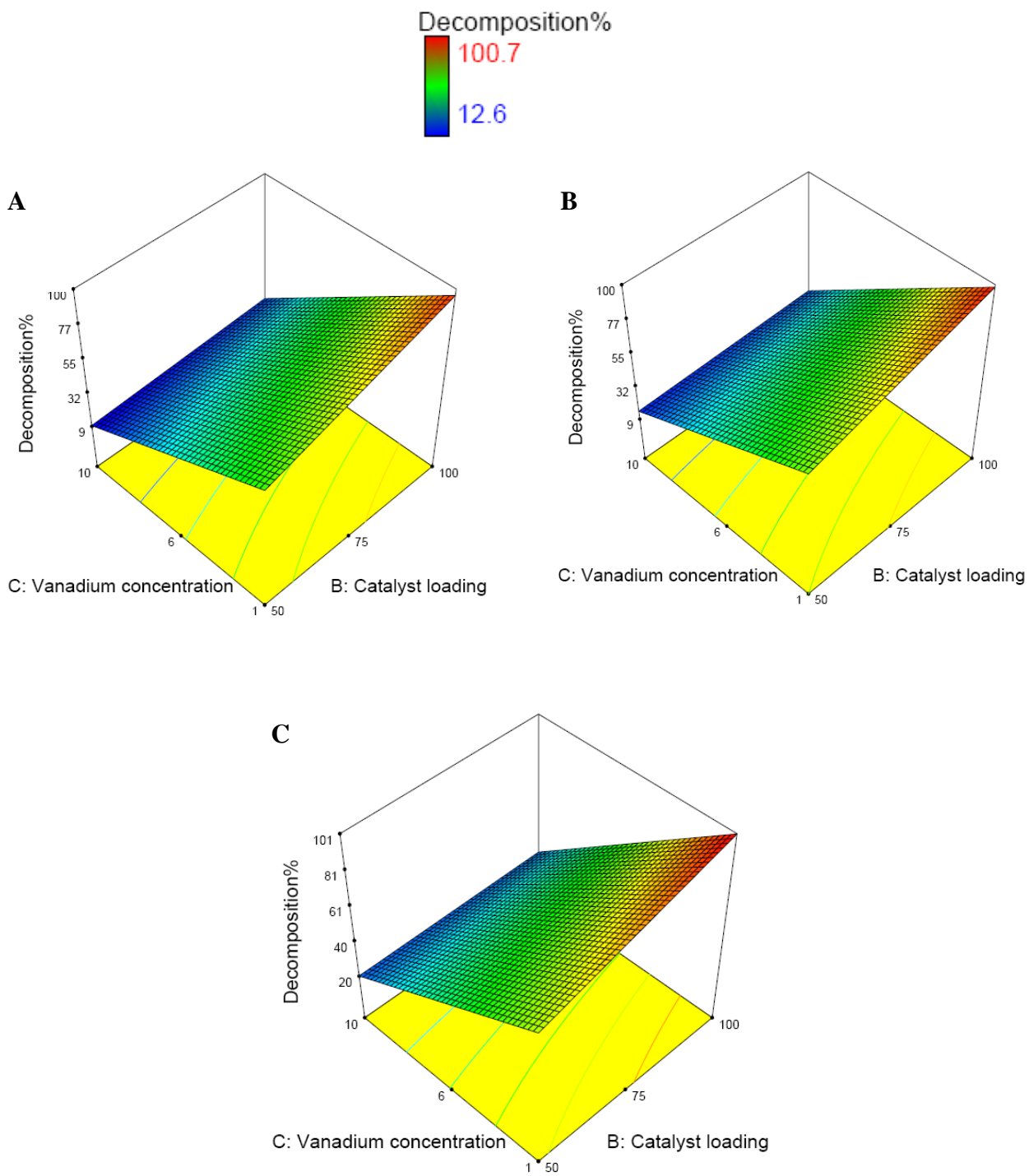


Figure 4-22. The 3D response surface plot of dye decomposition% of series calcined vanadium doped flakes as the factor A and B under different aeration rate. A) 0. B) 5. C) 10 ft^3/hr .

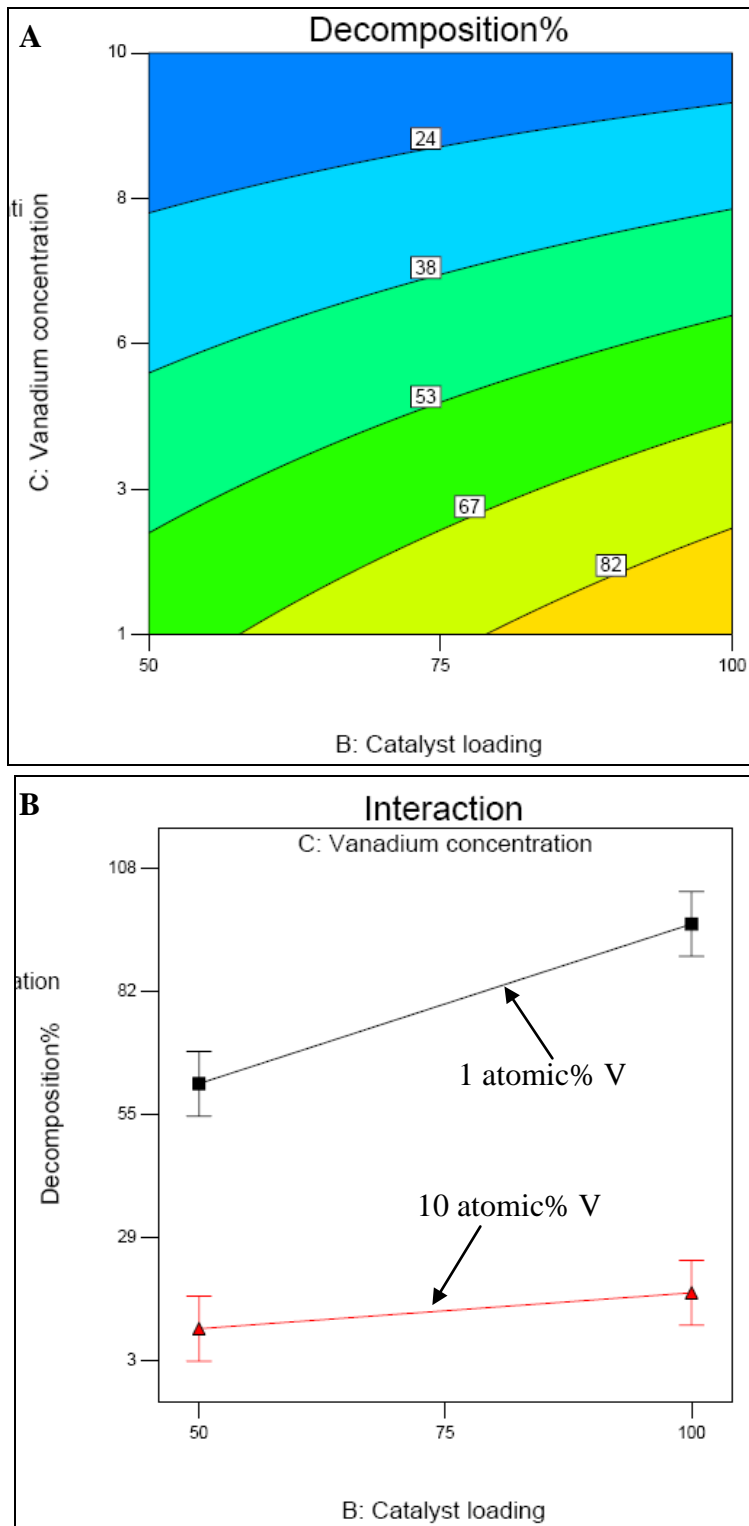


Figure 4-23. Model graphs of series vanadium doped flakes as the function of B and C at constant aeration rate (A = 0). A) Contour plot of decomposition% of series vanadium doped flakes. B) Interaction plot of response data against factor B for both levels of factor C.

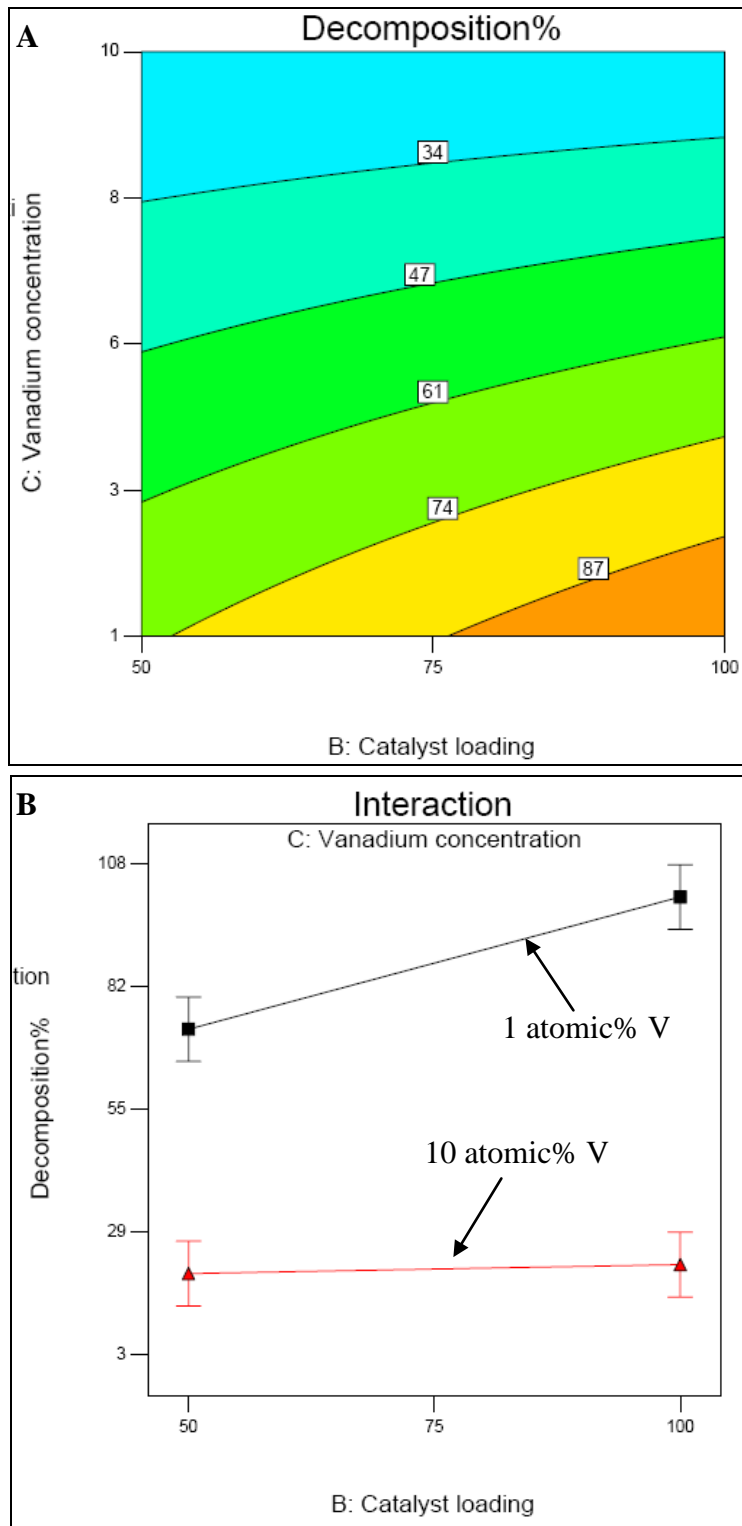


Figure 4-24. Model graphs of series vanadium doped flakes as the function of B and C at constant aeration rate (A =10). A) Contour plot of decomposition% of series vanadium doped flakes. B) Interaction plot of response data against factor B for both levels of factor C.

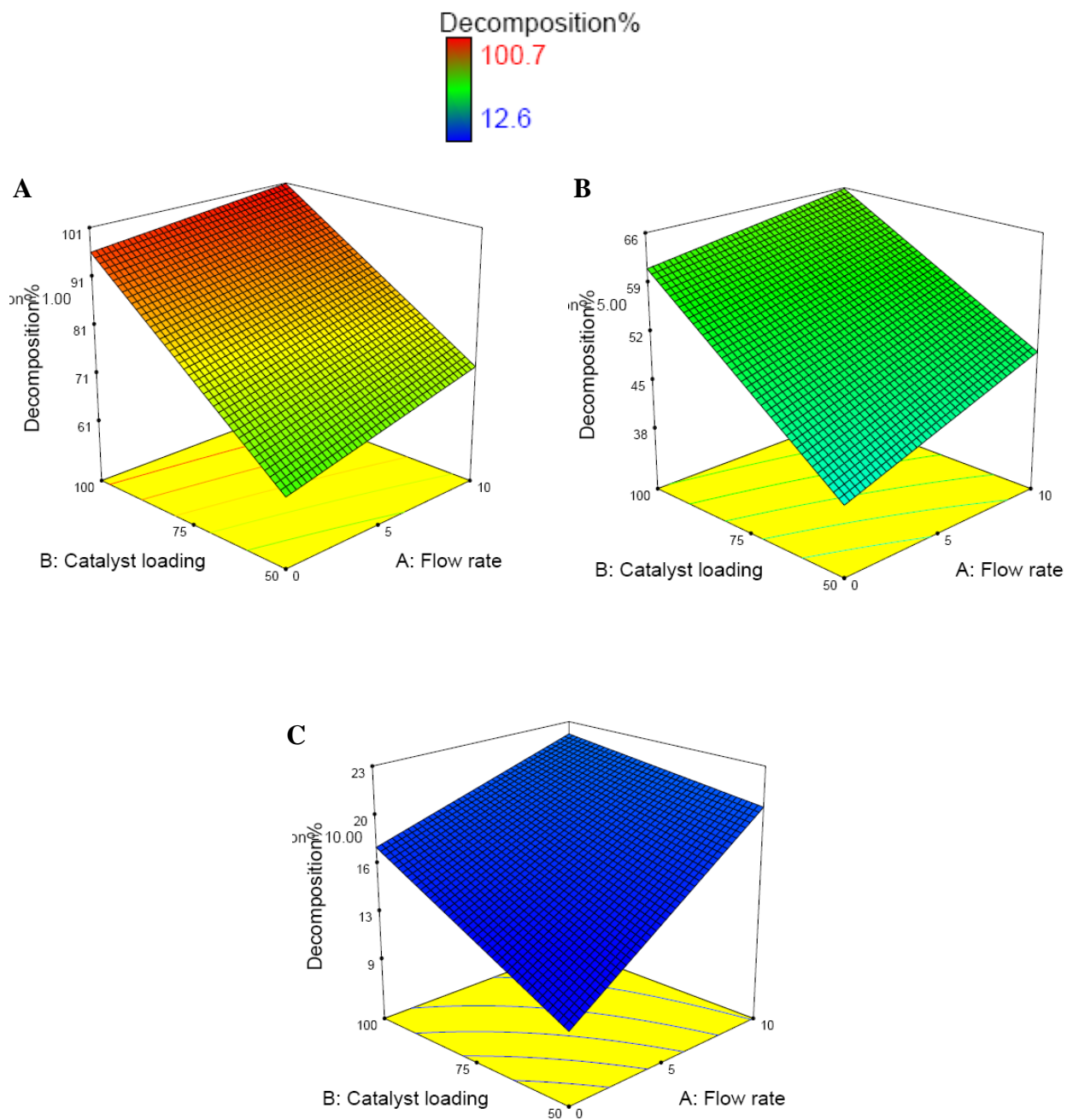


Figure 4-25. The 3D response surface plot of dye decomposition% of series calcined vanadium doped flakes as the factor B and C. A) 1. B) 5. C) 10 atomic% vanadium.

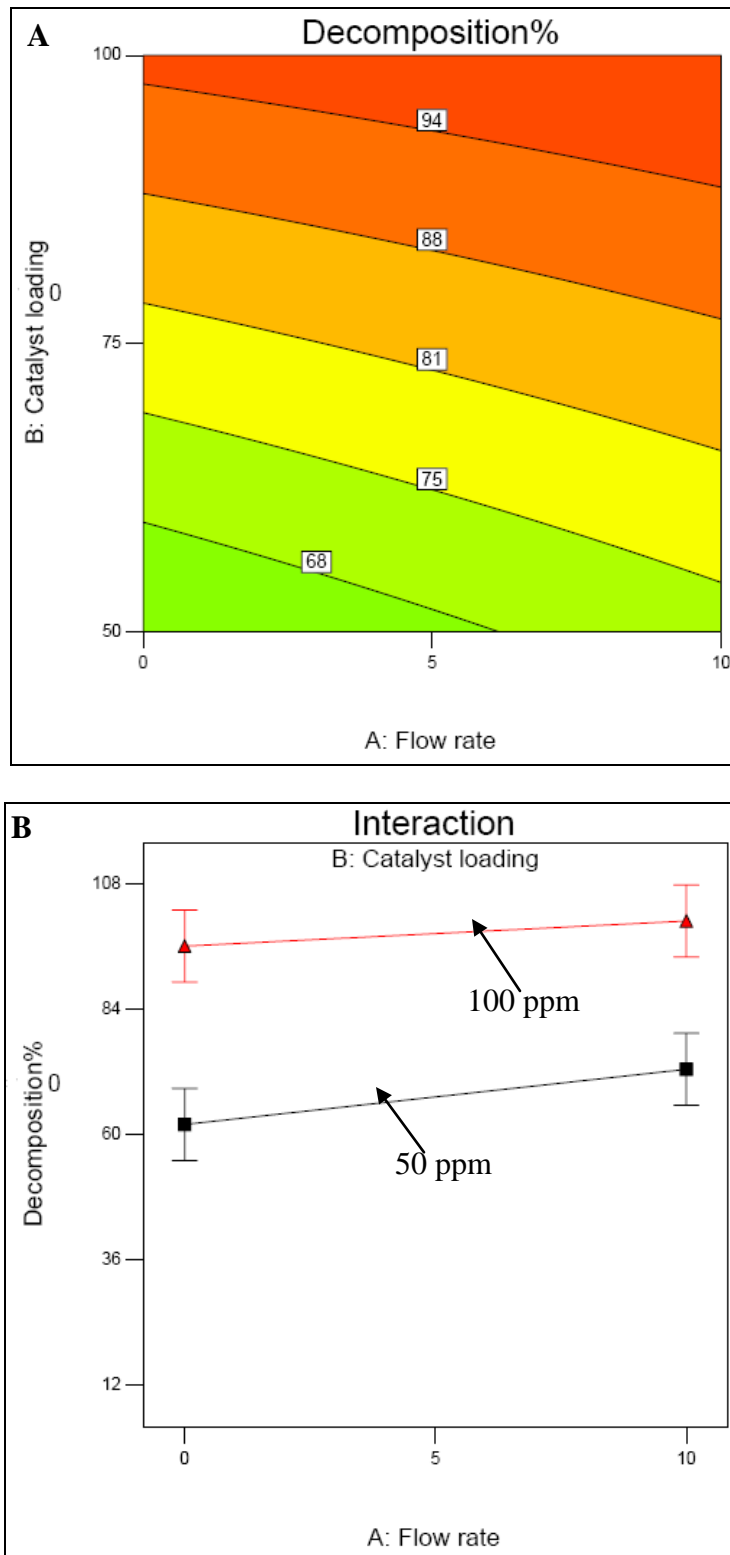


Figure 4-26. Model graphs of calcined 1 atomic% vanadium doped flakes as the function of A and B. A) Contour plot of decomposition%. B) Interaction plot of response data against factor A for both levels of factor B.

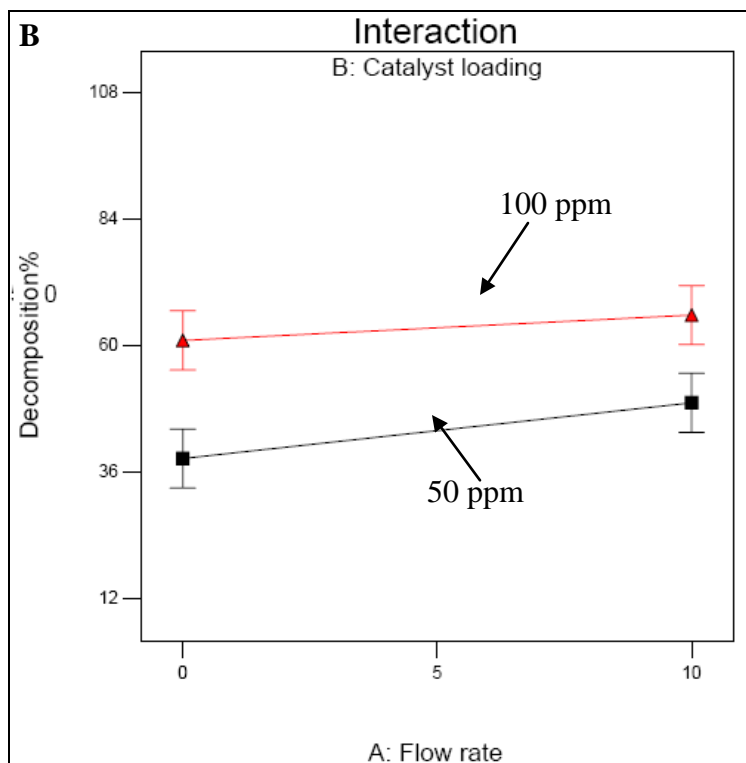
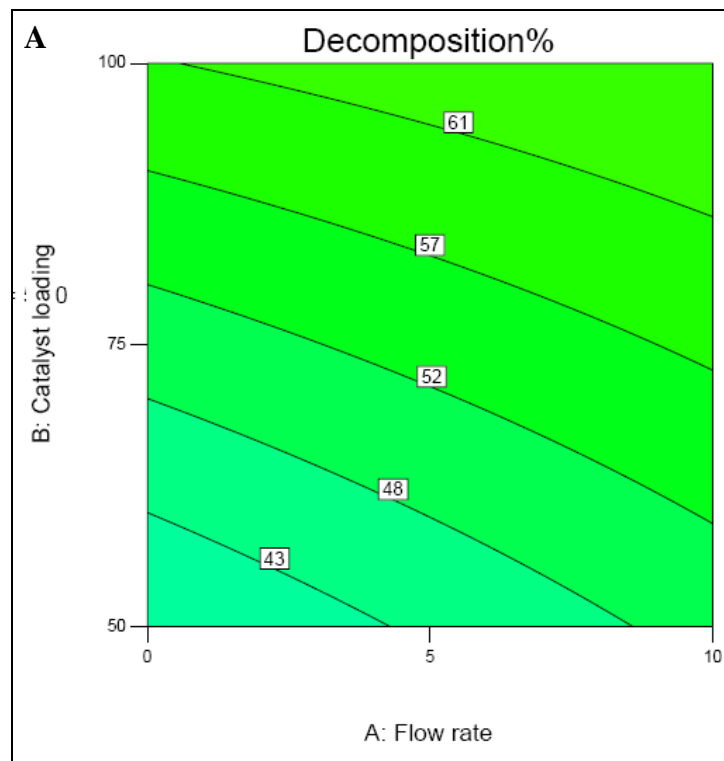


Figure 4-27. Model graphs of calcined 5 atomic% vanadium doped flakes as the function of A and B. A) Contour plot of decomposition%. B) Interaction plot of response data against factor A for both levels of factor B.

CHAPTER 5 TITANIA NANOFILAKES BASED DYE-SENSITIZED SOLAR CELLS

Introduction

Dye-sensitized solar cells (DSSCs) are the member of the group of thin film solar cells. The basic components of the DSSCs are a wide bang gap semiconductor film on the conducting glass substrate surrounding between the sensitizer and the electrolyte. In 1991 O'Regan and Gratzel invented a nanoporous electrode and made the remarkable breakthrough of energy conversion efficiency up to ~ 7% [160]. The currently highest efficiency of this type of cell is ~ 11% [161]. The advantages of DSSCs are as follows: (1) Cost-effective manufacture due to the usage of low-cost material compared to conventional solar cell (2) Flexible or light-weight products without extra protection are possible (3) Relatively insensitive to impurities (4) Wide range for operation (5) Non-vacuum and low temperature manufacture via continuous processes (for instance, doctor blade, spraying coating, or screen printing) [162].

Conventional solar cells employ a p-n junction to absorb light and generate electron-hole pairs. At the same time, the photoexcited electrons have to separate from positive charged holes before they transfer into the outer circuit to generate electricity. Therefore, the quality of single crystal silicon film that commonly used in the conventional product has to be extremely pure in order to overcome the undesired recombination. The high cost of making defect-free silicon is the main obstacle for large scale solar energy application. DSSCs have different operational features compared to the conventional solar cell and will be discussed in the following section.

Basic Principles and Components of DSSCs

Schematic diagram of the DSSCs is shown in Figure 5-1 [163]. The detail photoconversion process could be described as the following steps (Figure 5-2) [164]:

1. When incident photon with suitable energy absorbed by the dye molecules (S), an electron were excited from the highest occupied molecular orbital (HOMO) to lowest unoccupied molecular orbital (LUMO).
2. The electronically excited dye (S^*) injected an electron into the conduction band of the wide band gap semiconductor film (the most common material is TiO_2) within a very short time period (typically occurs in several picoseconds) [162].
3. The electrons diffused through the semiconductor film and transported to the external circuit.
4. The liquid electrolyte (iodide complex) reduced the dye cation (S^+) to the neutral state for future light absorption.
5. The oxidized electrolyte (I_3^-) reached to the catalytic platinum layer at the counter electrode and then reduced back to I^- .

It is worthy to note that there is no permanent chemical transformation in the cell when generating electricity. Unlike the conventional solar cell, DSSCs have more common features with the photosynthesis process in the natural world. For example, the chlorophyll is a common green pigment found in many plants. It serves the same function as the sensitizer in DSSCs which absorb light and transfer energy to the positive and negative charge carriers. Therefore, the main difference between DSSCs and conventional solar cell is light absorption that occurs away from the place where charge carriers separated. It obviously benefits the initial charge separation. More detail discussion of operation principles can be found in other review papers [165-167].

The Energetic Aspect of DSSCs

The energetics of the DSSCs are usually described as the relationships between the HOMO/LUMO levels of the dye molecules, the conduction band of the semiconductor and redox potential of the electrolyte (Figure 5-2). In order to function the DSSCs properly, there are several requirements needed to be confirmed. First of all, the LUMO level of the dye must be sufficiently higher than the conduction band of the semiconductor for efficient electron injection. Then the redox potential of the electrolyte should be lower than the HOMO level of the dye for

successful reduction of excited dye. Finally, the charge carrier injection process must be sufficiently faster than the de-excitation step of the photon activated dye molecules in order to collect electrons.

The typical current voltage (I-V) curve of a solar cell is shown in Figure 5-3. In order to introduce the photoenergy conversion efficiency, several important parameters will be carefully described in the following:

1. Short-circuit current (I_{sc}): The current flows through in a solar cell of no resistance (or voltage across the cell is zero). It is the maximum current that could be generated and drawn from a solar cell at certain intensity of light.
2. Open-circuit voltage (V_{oc}): In contrast, the voltage developed by a solar cell of very large external resistance (or current is zero). It is also the maximum voltage available from a cell.
3. Fill factor (FF): The ratio of the maximum power available along the whole I-V curve divided by the product of I_{sc} and V_{oc} (equation 5-1). Higher the fill factor, better the cell perform.

$$FF = \frac{I_M \times V_M}{I_{sc} \times V_{oc}} \dots\dots\dots(5-1)$$

where I_M is the maximum current density; V_M is the maximum voltage.

4. Solar energy conversion efficiency (η): Any energy conversion efficiency could be defined as the ratio of the energy output to the input energy. Therefore, it could be described as the ratio of output electricity generated by the solar cell to the available solar power (equation 5-2). This efficiency is the most commonly used property when comparing to different solar cells.

$$\eta(\%) = \frac{P_{out}}{P_{in}} \times 100\% = \frac{P_M}{P_{in}} \times 100\% = \frac{I_{sc} (mA/cm^2) \times V_{oc} (V) \times FF}{P_{in} (mW/cm^2)} \times 100\% \dots\dots\dots(5-2)$$

where P_{out} is the output energy; P_{in} is the input energy which is the available solar power in this case; P_M is the maximum power point.

Experiment

The titania pastes were prepared by adding 5 volume% of acetic acid solution as stabilizer into 15 wt% of water based titania slurry with three different samples (Degussa P25, synthesized and calcined titania flakes). In order to reduce aggregation, the above slurries were dispersed

using the programmable ultrasonicator (MISONIX Sonicator 3000 cup horns type) at 100 W for 15 minutes. The photoelectrodes for DSSCs were made by depositing the titania pastes on the transparent indium tin oxide (ITO) coated conducting glass (sheet resistance $< 30 \Omega/\text{square}$) using the doctor-blade method. Before pasting the titania film, there were two additional cleaning steps for the ITO glass. The glass sheet was degreased in a sonication assisted acetone bath and then washed thoroughly with high purity water (nanopure) and isopropanol respectively. After drying the film in air at ambient temperature, the photoelectrode was annealed at $450 \text{ }^\circ\text{C}$ for 1 hour and then cooled. The sintered photoanode was immersed in the ruthenium dye solution (0.3 mM) for 24 hours to completely load the sensitizer. The stained photoelectrode was then rinsed with acetonitrile to remove the excess dye molecule, and assembled with the platinized counter electrode made by platinum coating from the ion beam coater (Gatan model 681 ion beam coater).

The morphology of sintered titania photoanodes and platinum coated counter electrodes were investigated by SEM. The liquid electrolyte consisted of 0.05 M iodine, 0.1 M lithium iodide, and 0.5 M tert-butyl pyridine in acetonitrile was added to the interspace between working and counter electrodes via capillary action. The photovoltaic performance of the DSSCs was determined by the Keithley 4200 source meter with a solar simulator (Oriel sol 1A TH) which provided the standard AM 1.5 illumination.

Photoelectrodes Characterization

The basic physical properties (such as particle size distribution, thickness, specific surface area etc.) of synthesized and calcined titania flakes were shown in the Chapter 3. The microstructure and thickness of electrodes were measured by the SEM technique. The diffuse reflectance spectra of the titania films were investigated by the UV-Visible spectrometer equipped with an integrating sphere within the wavelength of 400-700 nm. The dye absorption

test was studied by adding 50 mg of titania samples in 20 ml 0.3 mM N719 solution at room temperature for 24 hours to mimic the real dye absorption behavior at the titania surface. After separating the solid and dye molecules by centrifugation, the concentration of residual dye solution was determined by the UV-Visible spectrometer.

Photovoltaic Measurements

The photocurrent-voltage (I-V) characteristics of the cells were measured under illumination of simulated AM 1.5 irradiation (100 mW/cm^2) provide by a solar simulator (Oriel sol 1A TH) calibrated with a standard crystalline silicon solar cell. The photovoltaic performance such as short-circuit current (I_{sc}), open-circuit voltage (V_{oc}), of the DSSCs were recorded with the Keithley model 4200 digital source meter; then fill factor (FF), and energy conversion efficiency (η) were calculated based on the above results with the corresponding area of the titania film.

Assembling DSSCs using High Aspect Ratio Titania Particles

Typical photoelectrodes in the DSSCs or Gratzel cells were made by pasting a layer of titania nanoparticles on an indium tin oxide (ITO) glass or a fluorine-doped tin oxide (FTO) glass substrate [164-167]. Those nanoparticles were synthesized by a hydrothermal process in a batch manner using titanium alkoxide as titania precursor. The shape of nanoparticles is nearly spherical with the primary size of 15 nm and moderate specific surface area of about $100 \text{ m}^2/\text{g}$. We developed a novel method to fabricate high aspect ratio titania flakes with higher specific surface area ($150\text{-}330 \text{ m}^2/\text{g}$) and similar size in one dimension (40 nm thickness) in a continuous process. Therefore, we expected several advantages of using titania nanoflakes as an alternative materials in DSSCs. First of all, higher specific surface area tends to absorb more dye molecules and is expected to generate more electricity under the same irradiation condition. In the mean time, the electron diffusion path does not increase too much because one dimension of flakes

(thickness) still remains in the nanometer range. Furthermore, the morphology of film has been proved to be significantly affected the electron transport in the DSSCs [168]. The most important parameter is the number of interconnect between neighboring particles in the electron diffusion path. It was found that the higher the area of overlapping, the faster the electron transportation. For a nanoparticles film, the average number of neighboring particles (or being called coordinated particles) was calculated to be more than two. However, there is significantly larger number of coordinated particles when using calcined titania flakes as the starting materials. Due to the smaller grain size (~ 10 nm) and higher surface area, each flakes have much higher contact points with the adjacent flakes compared to the P25 film (Figure 5-4). Therefore, the photoexcited electron has higher probability to diffuse through the calcined flakes film and then into the outer circuit owing to the much higher contact area between each flake. Finally, the continuous synthesis allows us to scale up the titania flakes production to larger quantity comparing to the low productive batch process.

Characterization of Titania Photoelectrodes

After doctor blading and sintering, the photoelectrodes made from Degussa P25 nanoparticles usually showed some cracks on the ITO glass substrate (Figure 5-5). It was difficult to maintain the integrity of the semiconductor film when using P25 nanoparticles as titania precursor. The possible explanation is related to the difficulty of nanoparticles dispersion especially in the high solid loading condition (15 wt%). If the starting slurry for making titania film could not reach the appropriate dispersion in the main solvent (for example, water), the following agglomeration or coagulation must occur during drying and heat treatment steps and therefore film cracking could be easily observed. However, there were no cracks on the photoanodes made from calcined titania flakes (Figure 5-6). Because of the nature of these high aspect ratio flakes, the better dispersion could be easily achieved under the same process

condition. Two dimensions of these high aspect ratio particles are still in micron range. Therefore, titania flakes could be easily dispersed by the conventional dispersion techniques such as sonication, surfactant or electrostatic stabilization. And the integrity of semiconductor film could be easily preserved even after drying and the following sintering processes.

The surface morphology of sintered photoelectrodes made from calcined titania flakes were observed by SEM. Figure 5-7 showed the top views of the P25 based photoelectrodes. A continuously cracking film with many titania chunks could be observed from the low magnification SEM images (Figure 5-7 A and B). The result indicated that appropriate dispersion did not achieve in the current process condition and severe shrinkage occurred during the drying and sintering steps. Under higher magnification, the P25 based photoanode consisted of 30-40 nm interconnected nanoparticles layer (Figure 5-7 C). The film thickness is about 28 μm calculated from the cross section of the photoelectrode. In contrast, a crack-free surface film with high roughness and high porosity could be observed from the top views of SEM images for calcined flakes based photoelectrodes (Figure 5-9). The thickness of titania film is measured by taking the side view of titania film and determined to be about 20-25 μm (Figure 5-10). It is obvious that titania nanoflakes stack above each other and assemble to an integrated layer (Figure 5-10 B). The results indicated that calcined flakes films had much better adhesion than those made from Degussa P25. The relationship between film thickness and the photovoltaic performance of DSSCs will be discussed in the later section. Smooth and continuous platinized cathode deposited by the ion beam coater was shown in Figure 5-11. The thickness of platinum layer was about 40 nm and the quality of the platinum film was determined by the EDX spectrum and mapping technique (Figure 5-11B-D). The result suggested high quality platinum

film, which is essential to the reduction of liquid electrolyte during the photovoltaic process, deposited on the substrate.

The high loading titania slurries were vigorously sonicated in the ultrasonicator for better dispersion. The subsequent change of particle size especially for flakes is important and was determined by the laser diffraction technique. It should be noted again that larger dimension of flakes after sonicating could be measured under volume distribution basis. The results of three slurries are shown in Figure 5-12 and the statistics data are listed in Table 5-1. According to the BET measurements, calcined flakes have much higher surface area and porosity than P25 nanoparticles which have relatively low surface area ($50 \text{ m}^2/\text{g}$) and no porosity (Table 3-3). In general, more visible sensitized dye molecules could be adsorbed by the materials with higher specific surface area and porosity and therefore generated more electricity under the same illumination area. The amount of surface adsorbed dye were determined by immersing titania samples in the dye solution used in the photovoltaic measurement at room temperature for 24 hours. After solid-liquid separation, the residual dye concentration was monitored using the UV-Vis spectrometer and the results are shown in Table 5-2. It is worthy to note that calcined titania flakes have the highest coated dye molecules per unit surface area among these samples. It could be attributed to the preferential adsorption of dye in the small pores at titania surface. The absorption spectrum of the N719 dye was determined by the UV-Vis spectrometer (Figure 5-13). The maximum absorption wavelength of the N719 dye is shown at 538 nm and the absorption range covers the whole visible light spectrum.

Typical photoanodes made from titania nanoparticles in DSSCs were optically transparent with $10 \mu\text{m}$ thickness, implied the loss of a portion of the visible light or sunlight due to transmittance [169-171]. Optical properties, especially light scattering effect, are essential for the

DSSCs to enhance the light absorption capability [169-171]. In order to improve the light-harvesting efficiency and photon to current conversion efficiency, surface modification of titania films were attempted by several methods such as introducing of scattering centers inside or adding smaller particles on the top. The basic idea of these methods is to increase the ability of light scattering of the photoelectrodes. For quantifying the amount of diffusely scattered light from an incident beam on the titania film, the diffuse reflectance spectroscopy were used to measure and compare the photoelectrodes made from P25 nanocrystals and titania flakes (Figure 5-14). P25 films showed high ability of diffuse scattering especially in the range between 400 and 450 nm. However, a prompt decay in the diffuse reflection capabilities was observed while the wavelength increased from 450 to 800 nm. The weaker light scattering for P25 nanoparticles within the higher wavelength regime could be attributed to the smaller particle size (nominally 30-40 nm) compared to the wavelength of visible light. According to the classic Mie theory, the optimum diameter of light scattering center should be about half of the wavelength of incident light [170,171]. For the range of wavelength of interest, the optimum particle size for scattering is around 200-400 nm which is much larger than the nominal diameter of P25 nanoparticles. In contrast, gradually decrease of diffuse reflectance went toward the higher wavelength range for the films composed of synthesized flakes. Moreover, the photoelectrodes made from calcined flakes possessed significantly higher scattering ability within the whole wavelength range under the same process condition (with similar thickness). Both flakes are micrometer sized wide and this dimension is perpendicular to the path of incident light. Therefore, stronger light scattering could be expected due to the comparable particle size of the wavelength of visible light. Furthermore, the scattering of calcined flakes exceeded that of synthesized flakes could be attributed to phase transformation from low refractive index phase (amorphous, $R.I = 1.8$) to

anatase which is a high refractive index phase (R.I. = 2.5) [172,173]. In summary, light absorption and scattering ability of photoanodes could be improved by using titania nanoflakes as the starting materials due to the higher specific surface area and comparable size of visible light wavelength.

Photovoltaic Performance of Titania Photoelectrodes

To study the influence of titania film thickness on the photovoltaic behavior of DSSCs, P25 and calcined flake-based photoelectrodes with three different thicknesses (10, 15, 25 μm) were prepared and compared by their current density-voltage properties (Table 5-3). The 25 μm thick photoanodes made from calcined titania flakes showed a short-circuit current density of 15.5 mA/cm^2 and an power conversion efficiency of 7.4%, whereas the P25 electrodes with similar thickness reached a current density of 2.8 mA/cm^2 and efficiency of 1.3%. The typical I-V curves of P25 and calcined flakes electrodes with different thickness are demonstrated in Figure 5-15. At the comparable film thickness, the photocurrent densities and voltages generated from calcined flake-based cells are higher than those of P25-based cells (Figure 5-16). For illustrating the effect of thickness on the photovoltaic properties of DSSCs, the dependence of J_{sc} and V_{oc} on the thickness of photoanodes for P25 and calcined flakes are shown respectively in Figure 5-17. P25 anodes show no significant change on J_{sc} when increasing the thickness of film comparing to higher increment for calcined flakes (Figure 5-16 A). It is reasonable that efficiency and short-circuit current of cell increase continuously with titania film thickness [174]. Because the higher surface area associated with thicker layer leads to more absorbed dyes at titania surface and thus improve the probability of photoexcited electrons that inject into the conduction band of TiO_2 . Therefore, photogenerated current density increases correspondingly. In contrast, V_{oc} for both materials show the same trend (decrease) respect to the film thickness (Figure 5-16 B). The open-circuit voltage usually decreased with increasing thickness of film

because of higher recombination occurring at more available surface sites [174]. Furthermore, the energy conversion efficiency of DSSCs increased with film thickness could be explained by the competition between short-circuit current, open-circuit voltage and fill factor. The raise of short-circuit current not only compensates but also overcomes the loss of open-circuit which results in improved efficiency of DSSCs. In short, the photon energy conversion efficiency of the DSSCs was improved from 1.2% to 7.4% (about 5 times improvement) when replacing P25 nanoparticles with calcined titania flakes in the photoelectrodes on the same basis of film thickness.

Table 5-1. Particle diameter statistics for P25, synthesized and calcined flakes after ultrasonication.

Sample	D ₁₀ (μm)	D ₅₀ (μm)	D ₉₀ (μm)	Median (μm)	Standard Deviation (μm)
P25	3.9	13.3	19.8	9.8	20.9
Calcined flakes	0.2	3.2	7.5	2.2	6.5
Synthesized flakes	0.5	5.6	14.2	3.8	8.4

Table 5-2. Dye loading and physisorption measurements of P25, synthesized and calcined titania nanoflakes.

Sample	Dye loading ($\mu\text{M}/\text{mg}$)	Specific surface area (m^2/g)	Specific pore volume (cm^3/g)	Average pore diameter (nm)
Synthesized flakes	19.3	323	—	—
Calcined flakes	15.3	151	0.511	7.2
P25	3.1	49	—	—

Table 5-3. Photovoltaic properties of the dye sensitized solar cells assembled by using anodes made from P25 nanoparticles and calcined titania flakes of different thickness.

Sample	P25			Calcined titania flakes		
	10	15	25	10	15	25
Thickness (μm)						
Voltage (V_{oc} , mV)	776	747	737	810	793	785
Current density (I_{sc} , mA/cm^2)	2.6	2.7	2.8	11.9	13.5	15.5
Fill factor (FF)	0.59	0.58	0.59	0.61	0.62	0.61
Efficiency (%)	1.1	1.2	1.3	5.9	6.6	7.4

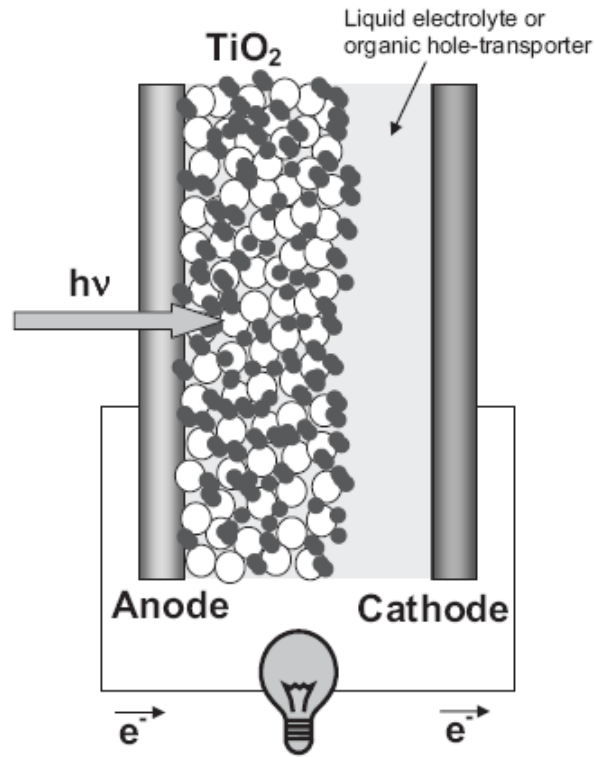


Figure 5-1. Schematic structure of DSSCs [163].

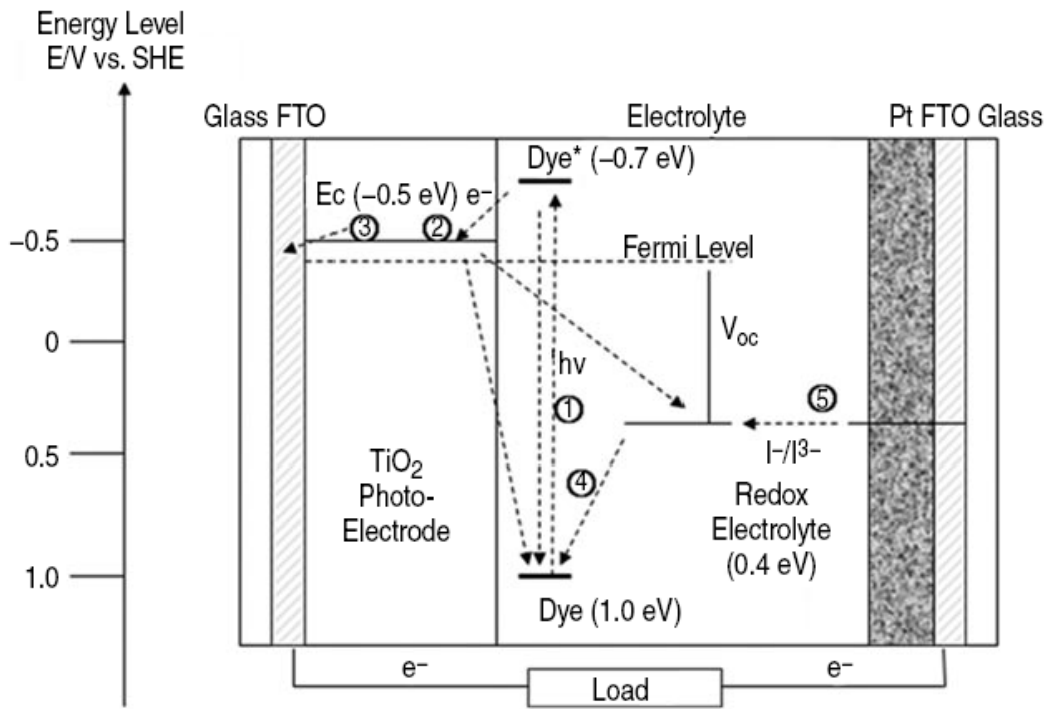


Figure 5-2. Energy levels in the typical DSSCs [164].

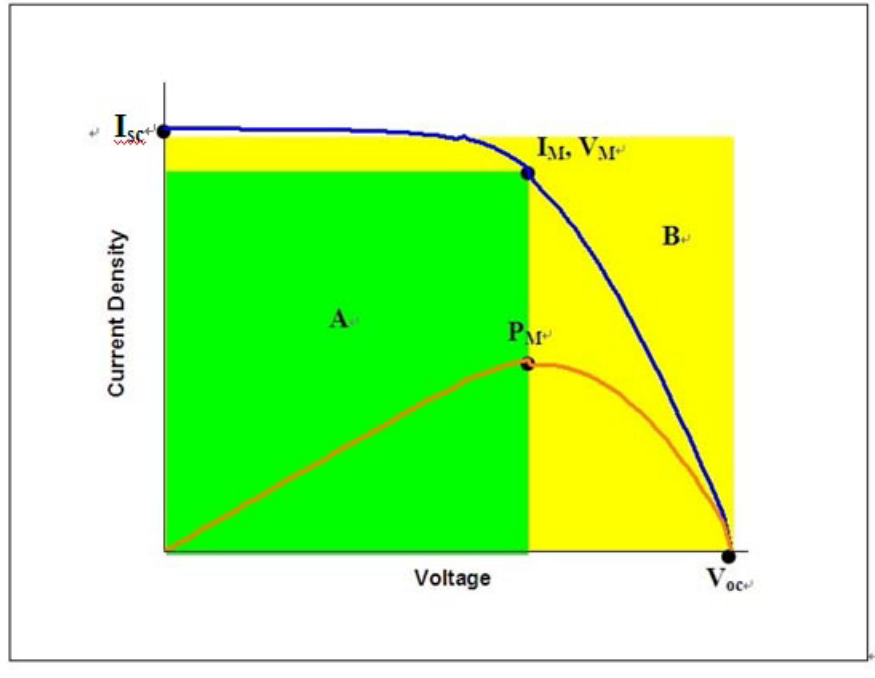


Figure 5-3. Typical I-V curves of the solar cells. (The fill factor, FF, could be calculated by the ratio of the area A to the area B).

A

B

Figure 5-4. Schematic cross sectional view of electron transport through titania layer. A) Degussa P25 nanoparticles. B) calcined titania nanoflakes (two dimensional nanostructures).

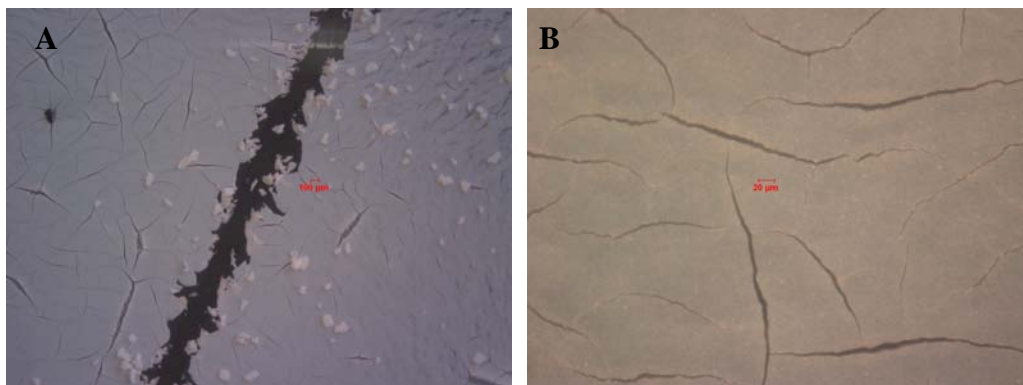


Figure 5-5. Optical micrographs of sintered titania photoelectrodes made from Degussa P25 nanoparticles. A) 5. B) 50 magnifications.

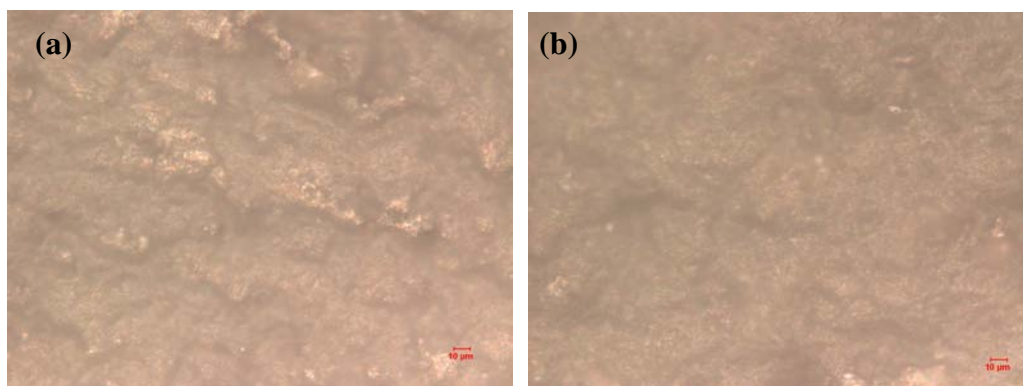


Figure 5-6. Optical micrographs of sintered titania photoelectrodes made from calcined titania flakes. A) 5. B) 50 magnifications.

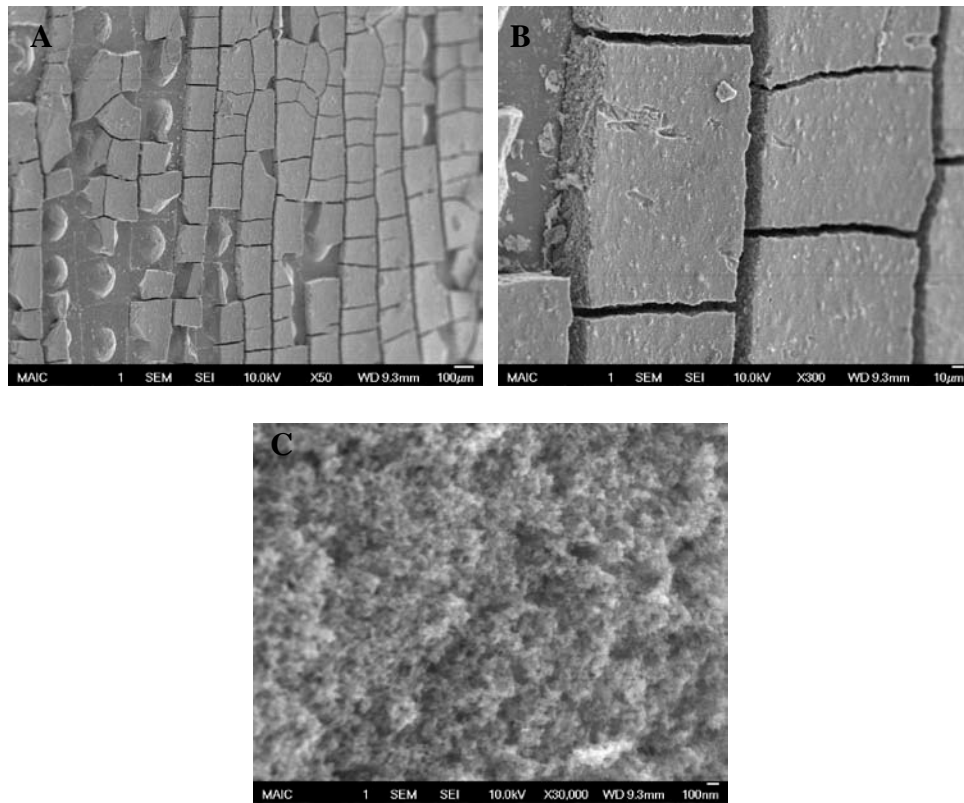


Figure 5-7. SEM micrographs of sintered photoelectrodes made from P25 nanoparticles under different magnifications.

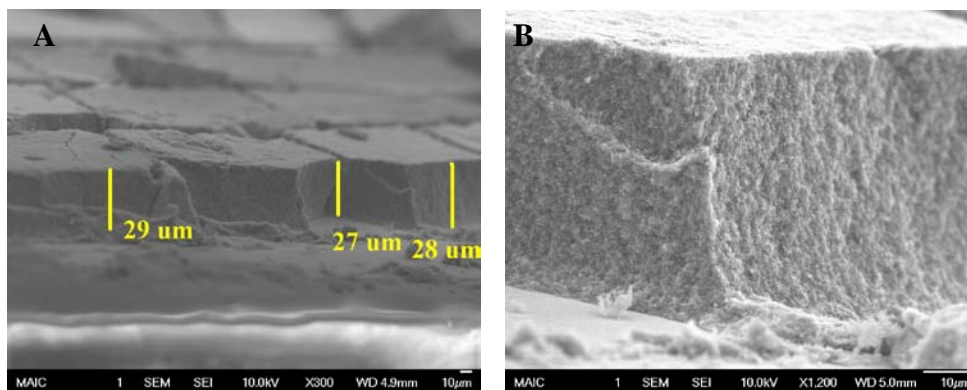


Figure 5-8. Cross section of sintered photoelectrodes made from P25 nanoparticles under different magnifications.

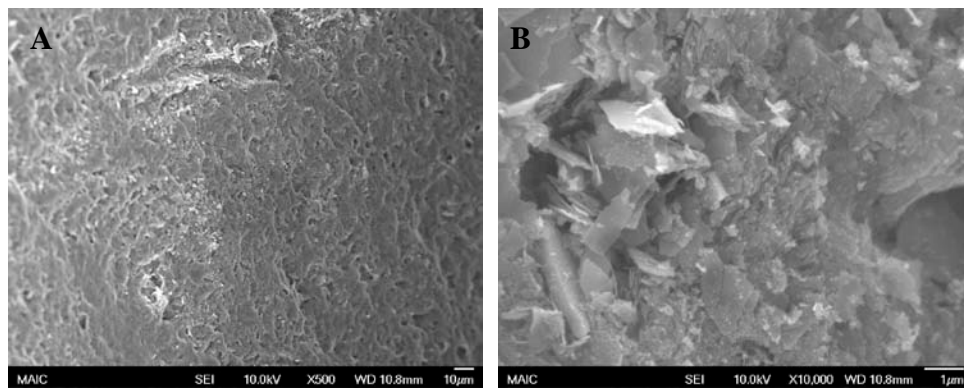


Figure 5-9. SEM micrographs of sintered photoelectrodes made from calcined titania flakes under different magnifications.

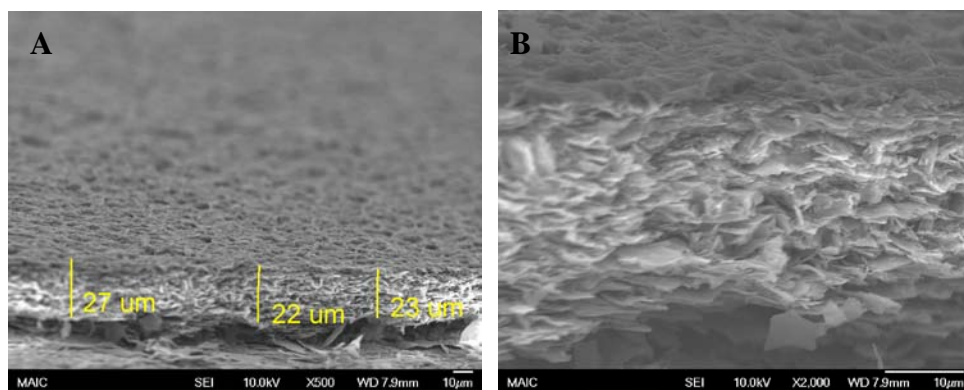


Figure 5-10. Cross section of sintered photoelectrodes made from calcined titania flakes under different magnifications.

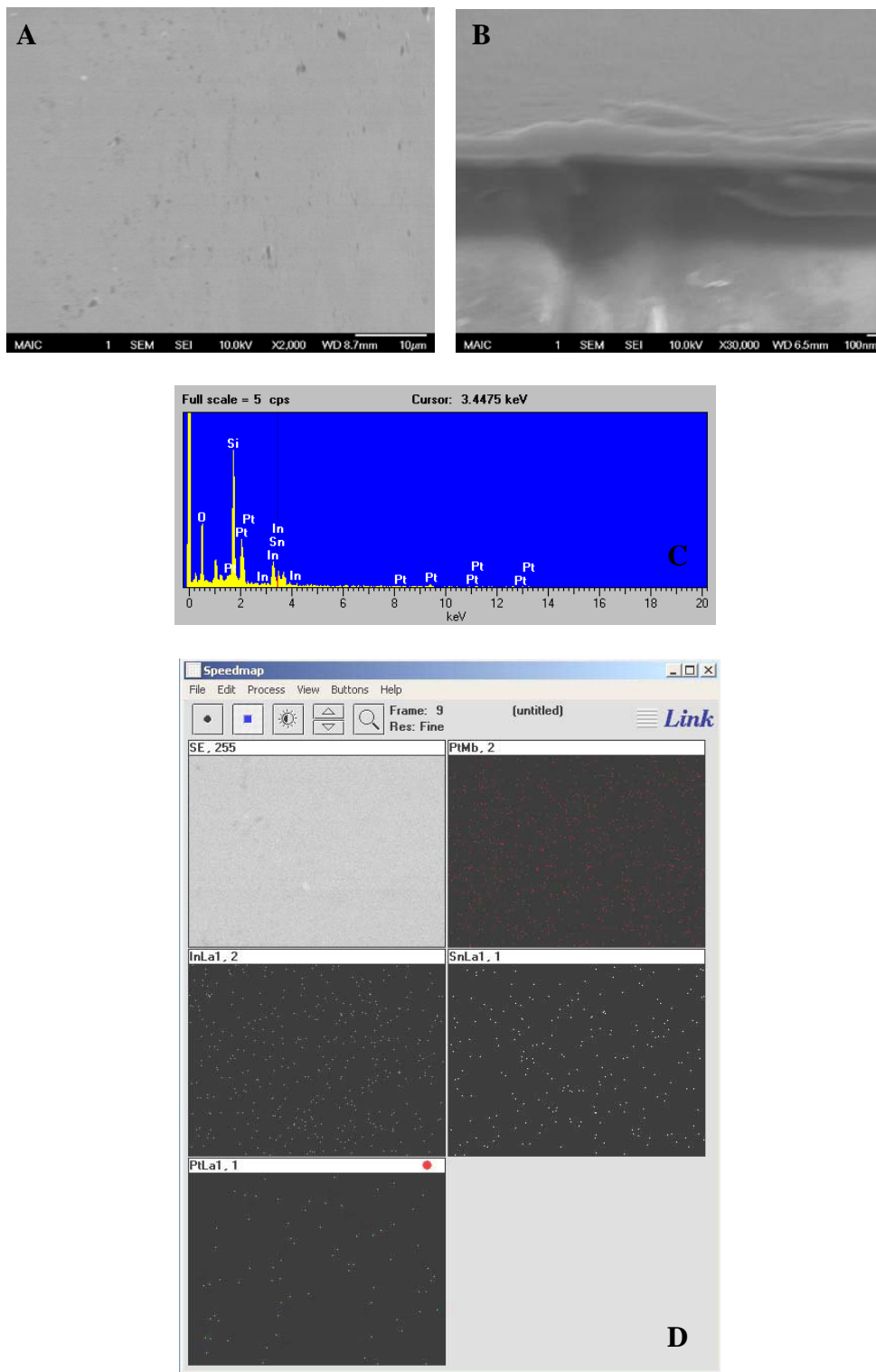


Figure 5-11. SEM images of platinum counterelectrode. A) surface morphology. B) thickness. C) EDX. D) mapping.

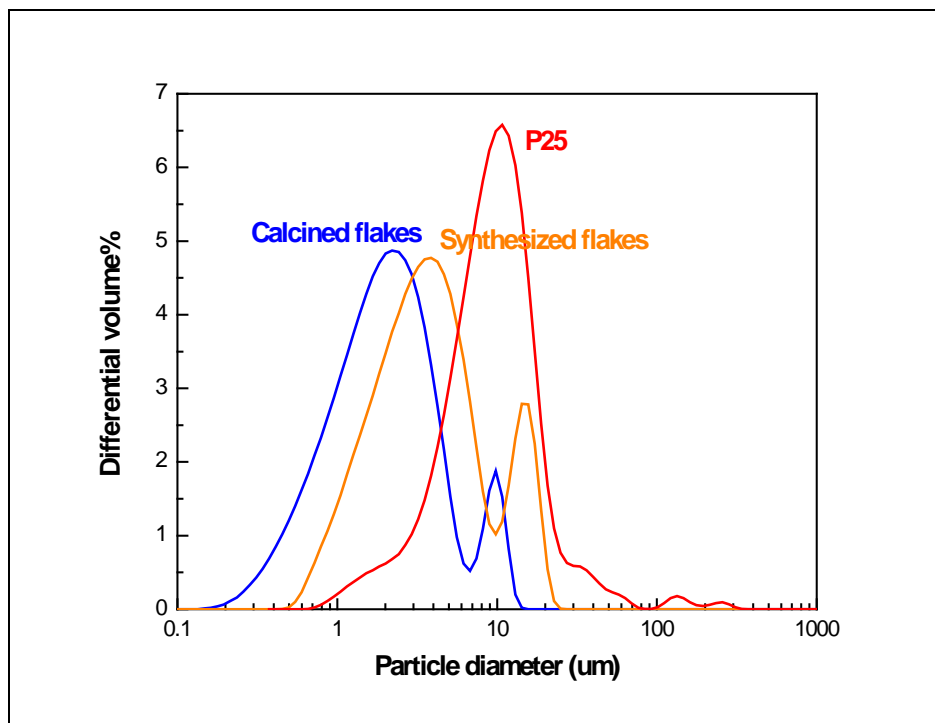


Figure 5-12. Particle size distribution of titania slurries for P25, synthesized and calcined titania flakes after ultrasonication at 100W for 15 minutes.

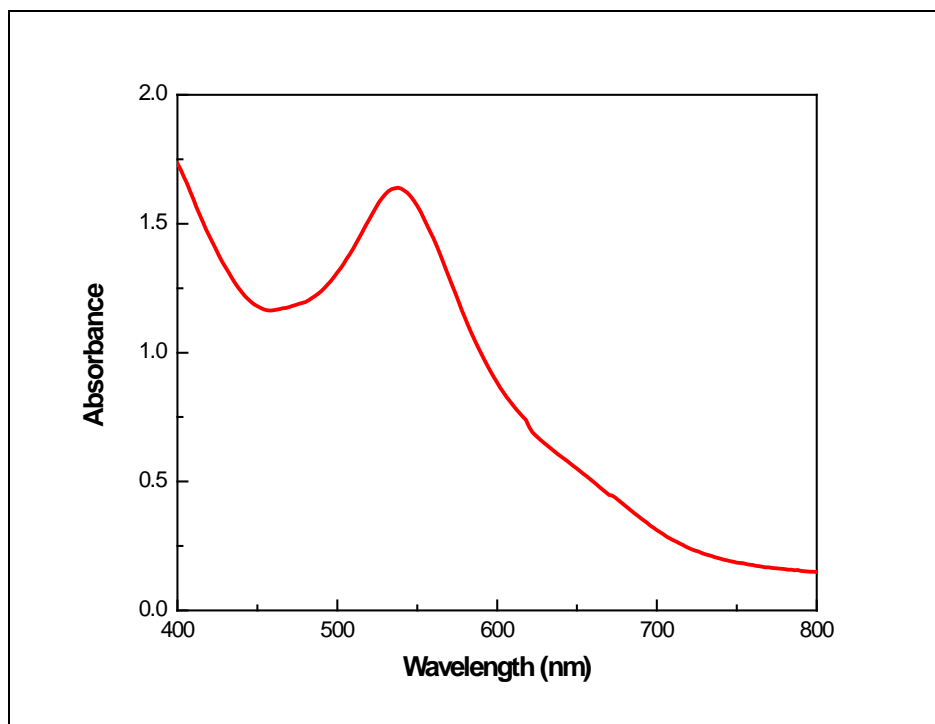


Figure 5-13. Absorption spectrum of 0.3 mM Ru complex dye solution (also as known N-719 dye).

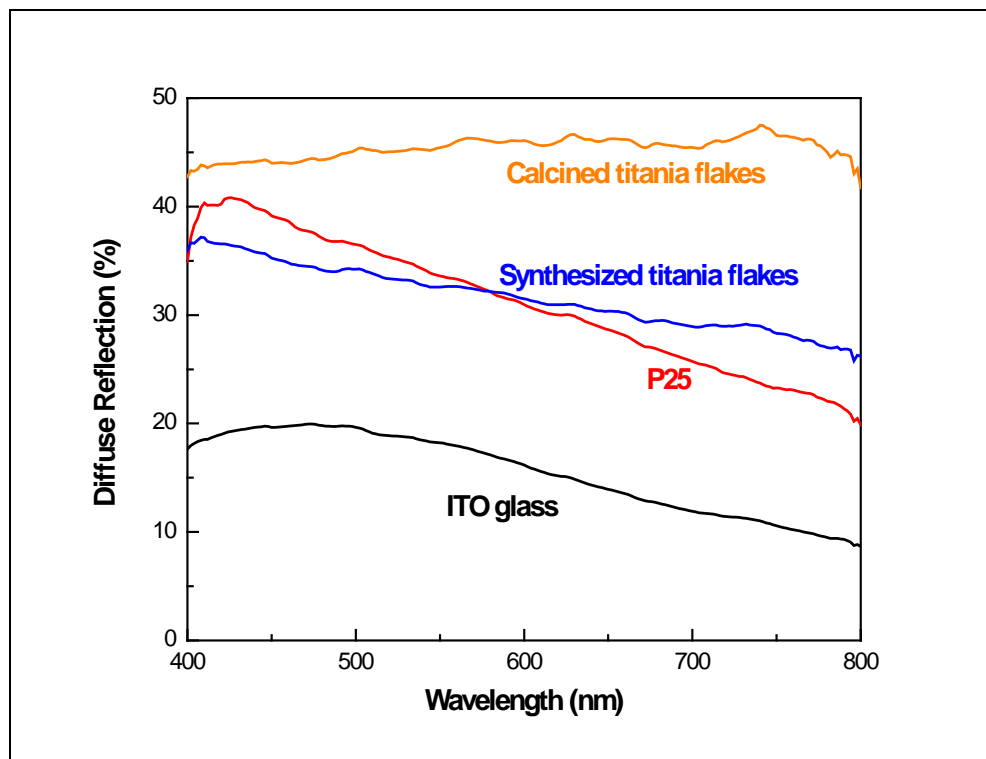


Figure 5-14. Diffuse reflectance spectra of the titania films prepared from Degussa P25 nanoparticles, synthesized and calcined titania flakes of similar thickness.

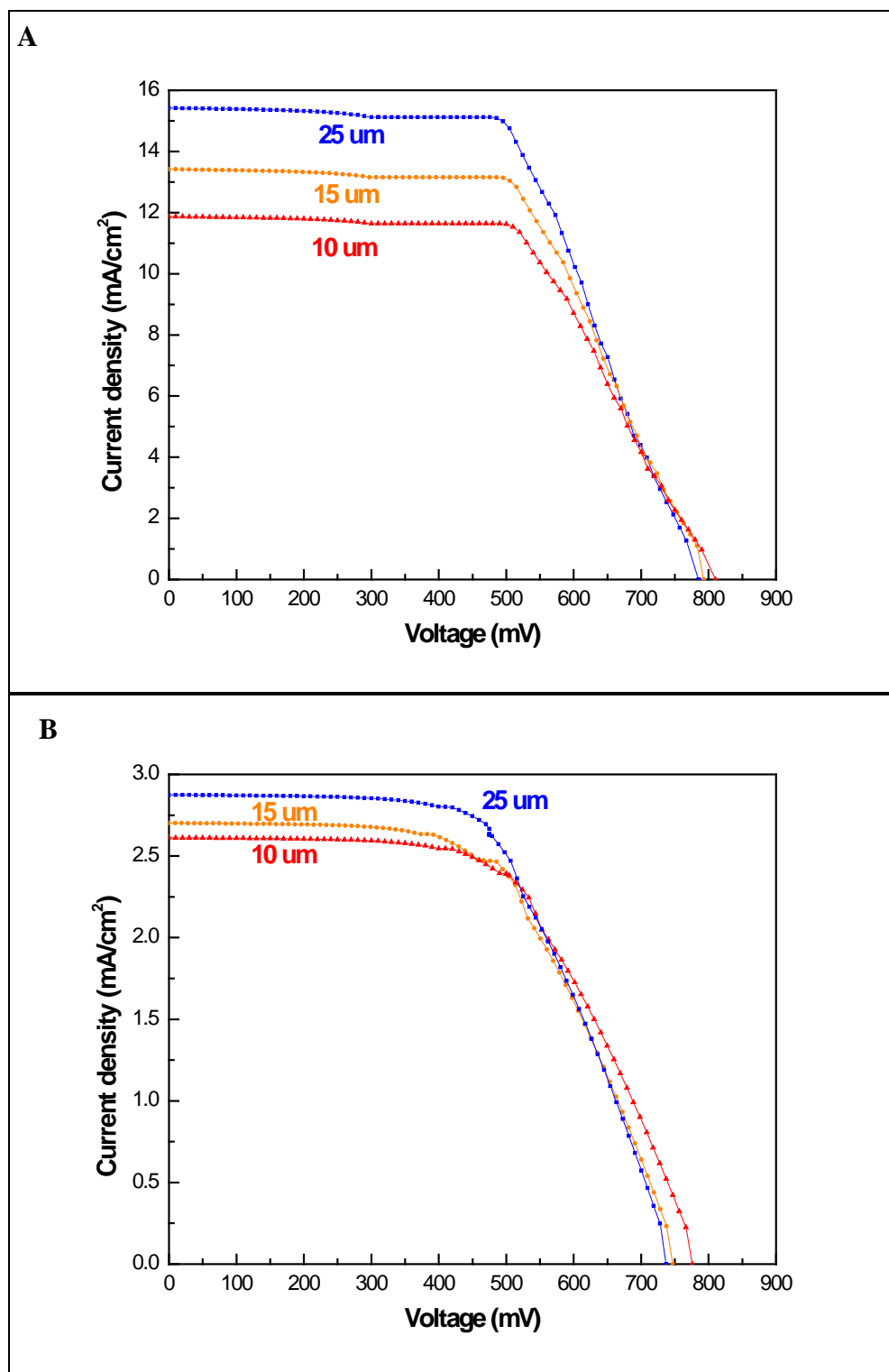


Figure 5-15. I-V curves of dye sensitized solar cells with different film thicknesses. A) calcined titania flakes. B) P25.

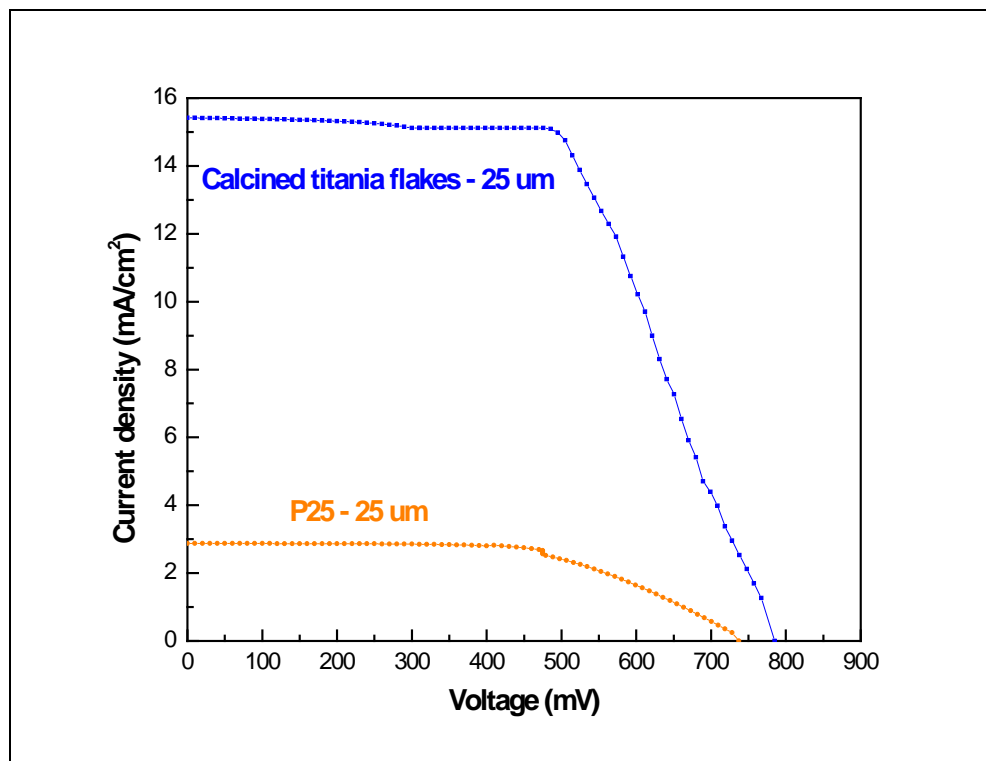


Figure 5-16. I-V characteristics of DSSCs made from P25 and calcined flakes of similar thickness under AM 1.5 simulated sunlight irradiation.

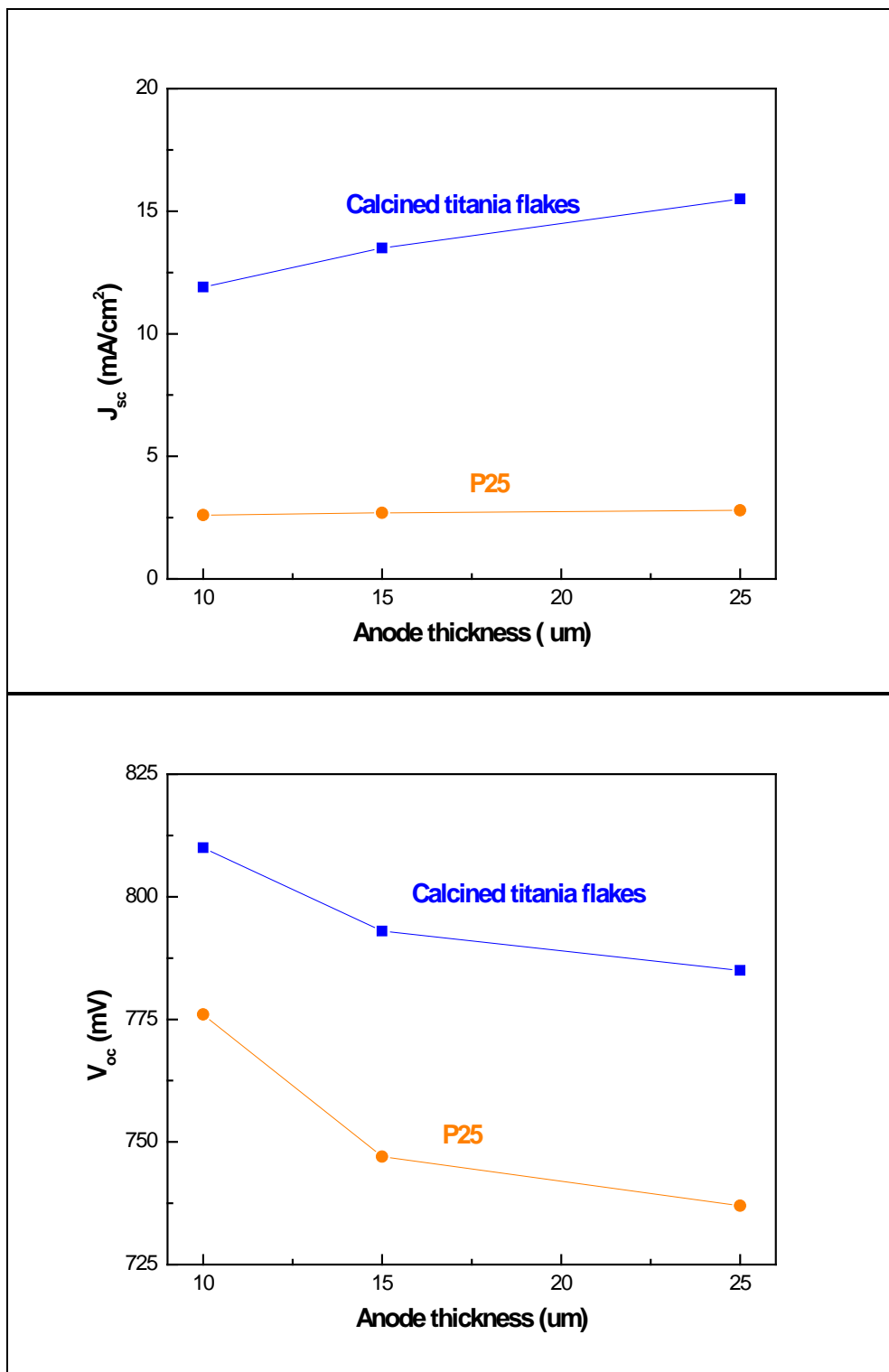


Figure 5-17. Comparison of the J_{sc} and V_{oc} of P25 and calcined flakes cells as a function of film thickness.

CHAPTER 6 SUMMARY, CONCLUSIONS, AND FUTURE WORK

Summary

The first goal of this study was to develop a new type of photocatalyst able to decompose more than 99% organic molecules in waste water within 2 hours. To accomplish this goal, high aspect ratio titania nanoflakes were successfully synthesized using the surface control hydrolysis method. Many characterization techniques were used to investigate both physical and chemical properties of titania flakes. When using calcined titania flakes as photocatalysts, completely photodegradation of the stimulated waste water (50 μM methylene blue solution) was achieved under UVA irradiation within 2 hours. At the same time, one of the most successful commercial products, Degussa P25, only showed 87% degradation under the same operational condition. In order to optimize the photocatalytic performance of titania flakes, statistics design of experiment were used to develop a predictive model within the investigated range. The results showed that the optimum condition of photocatalysis for calcined flakes was: median catalyst loading (75 ppm), higher aeration rate (10 ft^3/hr), and higher light intensity (mW/cm^2). Although titania flakes showed higher photocatalytic efficiency, higher energy required to activate this new materials due to larger band gap resulted from the quantum confinement effect.

The second goal of this study was to develop an energy-efficient photocatalyst without scarifying the high photocatalytic activity. In order to take the advantage of the most abundant energy in the world, solar power, narrowing the band gap of titania nanoflakes was the important approach. In this study, vanadium doped titania flakes were successfully fabricated using the same synthesis method. The decrease of band gap energy for vanadium doped samples was confirmed by the UV-Visible spectrometer. Accordingly, vanadium concentration, aeration rate, and catalyst loading were used as three main parameters in the statistics design analysis. It was

found that 1 atomic % vanadium doped flakes have the highest photocatalytic activity under visible light illumination. Completely decomposition of the organic species in the same simulated polluted water was achieved using 1 atomic % vanadium doped flakes under pure visible light illumination within 2 hours; on the other hand, P25 nanoparticles did not show significant visible photocatalytic activity.

Dye-sensitized solar cell is a promising technique to meet the clean energy demand in the future. However, the further improvement on the efficiency of this device is crucial for competing with the current electricity generation technology. Modified surface hydrolysis synthesized titania nanoflakes possessed many unique properties such as high aspect ratio, high specific surface area, slower recombination rate, mass production possibility... etc. Therefore, we expected enhanced photovoltaic performance for DSSCs when replacing the typical semiconductor layers, titania nanoparticles, with calcined titania nanoflakes. The results showed that 5 fold improvements compared to P25 nanoparticles based cell was achieved when assembling DSSCs with calcined flakes. Although the efficiency of titania flakes based cell has not been optimized, the preliminary results showed encouraging efficiency (7.4%).

Conclusions

The main conclusions in this study include:

- Over 99% of methylene blue solution (50 μM) was degraded by the high aspect ratio calcined titania nanoflakes under UVA irradiation within 2 hours, whereas not completely decomposition of dye solutions was achieved using P25 nanoparticles as photocatalysts under the same process condition.
- The same concentration of dye solutions were decomposed more than 99% under visible light illumination within 2 hours when using 1 atomic % vanadium doped flakes as remediation agent while almost no visible photocatalytic ability was shown for P25 nanoparticles.
- 7.4% of photon energy conversion efficiency of calcined flakes based DSSC which was 5 times improvement compared to P25 based cell was accomplished.

Future Work

The following were several recommendations for future work:

- From the optical measurements of titania samples, titania nanoflakes have highly light scattering ability compared to commercial products. Therefore, they have highly potential to be pigment materials. Further experiments such as hiding power, viscosity, and rheology need to be carried out in order to investigate the optimum formula for making paint using titania flakes.
- Thickness of titania flakes could be manipulated by adjusting the ratio of titania precursor to organic solvent. The desired thickness of titania flakes could be made accordingly to specific applications.
- Further DOE could be very useful to investigate the influence of thickness on certain applications. For example, one of the main parameters in this study, photocatalytic activity, could depend on the thickness of flakes.
- The real properties of visible photocatalysis using vanadium doped flakes could be investigated by carrying out the experiment under sun light illumination. And the optimum concentration of vanadium could be measured using the DOE technique.
- The optimization of the formula for DSSCs using flakes based materials need to be conducted by using the DOE. And larger area of DSSCs should be made and tested in order to extend the application to commercial scale.

APPENDIX A
ANALYSIS VARIANCE FOR UV PHOTOCATALYSIS USING SYNTHESIZED FLAKES

A: Flow rate
B: Catalyst loading
C: Light intensity
Response: Decomposition%

Table A-1. Analysis of variance table

Source	Sum of Squares	df	Mean Square	F Value	p-value Prob > F	
Model	4318.20	5	863.64	18.94	0.0069	significant
A	253.13	1	253.13	5.55	0.0780	
B	2443.01	1	2443.01	53.58	0.0019	
C	852.84	1	852.84	18.70	0.0124	
AB	224.72	1	224.72	4.93	0.0906	
BC	544.50	1	544.50	11.94	0.0259	
Curvature	1.46	1	1.46	0.032	0.8669	not significant
Residual	182.39	4	45.60			
Lack of Fit	143.70	2	71.85	3.71	0.2121	not significant
Pure Error	38.69	2	19.34			
Cor Total	4502.04	10				

The Model F-value of 18.94 implies the model is significant. There is only a 0.69% chance that a "Model F-Value" this large could occur due to noise.

Values of "Prob > F" less than 0.0500 indicate model terms are significant. In this case B, C, BC are significant model terms. Values greater than 0.1000 indicate the model terms are not significant. If there are many insignificant model terms (not counting those required to support hierarchy), model reduction may improve your model.

The "Curvature F-value" of 0.03 implies the curvature (as measured by difference between the average of the center points and the average of the factorial points) in the design space is not significant relative to the noise. There is a 86.69% chance that a "Curvature F-value" this large could occur due to noise.

The "Lack of Fit F-value" of 3.71 implies the Lack of Fit is not significant relative to the pure error. There is a 21.21% chance that a "Lack of Fit F-value" this large could occur due to noise. Non-significant lack of fit is good -- we want the model to fit.

Table A-2. Statistical results

Std. Dev.	6.75	R-Squared	0.9595
Mean	42.67	Adj R-Squared	0.9088
C.V. %	15.82	Pred R- Squared	0.4699
PRESS	2386.32	Adeq Precision	12.410

The "Pred R-Squared" of 0.4699 is not as close to the "Adj R-Squared" of 0.9088 as one might normally expect. This may indicate a large block effect or a possible problem with your model and/or data. Things to consider are model reduction, response tranformation, outliers, etc.

"Adeq Precision" measures the signal to noise ratio. A ratio greater than 4 is desirable. Your ratio of 12.410 indicates an adequate signal. This model can be used to navigate the design space.

APPENDIX B
ANALYSIS VARIANCE FOR UV PHOTOCATALYSIS USING CALCINED FLAKES

A: Flow rate
B: Catalyst loading
C: Light intensity
Response: Decomposition%

Table B-1. Analysis of variance table

Source	Sum of Squares	df	Mean Square	F Value	p-value Prob > F	
Model	4099.21	5	819.84	454.42	< 0.0001	significant
A	37.84	1	37.84	20.98	0.0102	
B	1693.62	1	1693.62	938.73	< 0.0001	
C	2271.38	1	2271.38	1258.96	< 0.0001	
AB	9.24	1	9.24	5.12	0.0863	
BC	87.12	1	87.12	48.29	0.0023	
Curvature	10.88	1	10.88	6.03	0.0700	not significant
Residual	7.22	4	1.80			
Lack of Fit	5.69	2	2.85	3.73	0.2115	not significant
Pure Error	1.53	2	0.76			
Cor Total	4117.31	10				

The Model F-value of 454.42 implies the model is significant. There is only a 0.01% chance that a "Model F-Value" this large could occur due to noise.

In this case A, B, C, BC are significant model terms.

The "Curvature F-value" of 6.03 implies there is curvature in the design space. There is only a 7.00% chance that a "Curvature F-value" this large could occur due to noise.

The "Lack of Fit F-value" of 3.73 implies the Lack of Fit is not significant relative to the pure error. There is a 21.15% chance that a "Lack of Fit F-value" this large could occur due to noise.

Table B-2. Statistical results

Std. Dev.	1.34	R-Squared	0.9982
Mean	61.49	Adj R-Squared	0.9960
C.V. %	2.18	Pred R- Squared	0.9771
PRESS	94.47	Adeq Precision	62.669

The "Pred R-Squared" of 0.9771 is in reasonable agreement with the "Adj R-Squared" of 0.9960. "Adeq Precision" measures the signal to noise ratio. Your ratio of 62.669 indicates an adequate signal. This model can be used to navigate the design space.

APPENDIX C
ANALYSIS VARIANCE FOR UV PHOTOCATALYSIS USING P25 NANOPARTICLES

A: Flow rate
B: Catalyst loading
C: Light intensity
Response: Decomposition%

Table C-1. Analysis of variance table

Source	Sum of Squares	df	Mean Square	F Value	p-value Prob > F	
Model	4569.44	5	913.89	1370.83	< 0.0001	significant
A	34.44	1	34.44	51.67	0.0020	
B	1601.78	1	1601.78	2402.67	< 0.0001	
C	2895.61	1	2895.61	4343.41	< 0.0001	
AB	32.80	1	32.80	49.21	0.0022	
BC	4.80	1	4.80	7.21	0.0550	
Curvature	62.84	1	62.84	94.26	0.0006	significant
Residual	2.67	4	0.67			
Lack of Fit	1.94	2	0.97	2.67	0.2725	not significant
Pure Error	0.73	2	0.36			
Cor Total	4634.95	10				

The Model F-value of 1370.83 implies the model is significant. There is only a 0.01% chance that a "Model F-Value" this large could occur due to noise. Values of "Prob > F" less than 0.0500 indicate model terms are significant. In this case A, B, C, AB are significant model terms. Values greater than 0.1000 indicate the model terms are not significant.

The "Curvature F-value" of 94.26 implies there is significant curvature in the design space. There is only a 0.06% chance that a "Curvature F-value" this large could occur due to noise.

The "Lack of Fit F-value" of 2.67 implies the Lack of Fit is not significant relative to the pure error. There is a 27.25% chance that a "Lack of Fit F-value" this large could occur due to noise.

Table C-2. Statistical results

Std. Dev.	0.82	R-Squared	0.9994
Mean	51.56	Adj R-Squared	0.9987
C.V. %	1.58	Pred R- Squared	0.9930
PRESS	32.67	Adeq Precision	108.239

The "Pred R-Squared" of 0.9930 is in reasonable agreement with the "Adj R-Squared" of 0.9987. "Adeq Precision" measures the signal to noise ratio. Your ratio of 108.239 indicates an adequate signal. This model can be used to navigate the design space.

APPENDIX D
ANALYSIS VARIANCE FOR VISIBLE PHOTOCATALYSIS USING VANADIUM DOPED
FLAKES

A: Flow rate
B: Catalyst loading
C: Vanadium concentration
Response: Decomposition%

Table D-1. Analysis of variance table

Source	Sum of Squares	df	Mean Square	F Value	p-value Prob > F	
Model	9972.65	5	1954.53	96.26	< 0.0001	significant
A	117.81	1	117.81	5.80	0.0610	
B	649.80	1	649.80	32.00	0.0024	
C	8638.70	1	8638.70	425.47	< 0.0001	
AB	16.53	1	16.53	0.81	0.4082	
BC	349.80	1	349.80	17.23	0.0089	
Residual	101.52	5	20.30			
Lack of Fit	100.51	3	33.50	66.56	0.0148	not significant
Pure Error	1.01	2	0.50			
Cor Total	9874.17	10				

The Model F-value of 96.26 implies the model is significant. There is only a 0.01% chance that a "Model F-Value" this large could occur due to noise.

In this case B, C, BC are significant model terms.

Table D-2. Statistical results

Std. Dev.	4.51	R-Squared	0.9897
Mean	51.05	Adj R-Squared	0.9794
C.V. %	8.83	Pred R- Squared	0.9012
PRESS	975.37	Adeq Precision	27.438

The "Pred R-Squared" of 0.9012 is in reasonable agreement with the "Adj R-Squared" of 0.9794. "Adeq Precision" measures the signal to noise ratio. A ratio greater than 4 is desirable. Your ratio of 27.438 indicates an adequate signal. This model can be used to navigate the design space.

LIST OF REFERENCES

- [1] Gleick, P. H. *The World's Water 2000 - 2001*; Island Press, 2000.
- [2] WHO *Global Water Supply and Sanitation Assessment 2000 Report*, WHO/UNICEF Joint Monitoring Programme for Water Supply and Sanitation, World Health Organization and United Nations Children Fund, **2000**.
- [3] Gogate, P. R.; Pandit, A. B. *Advances in Environmental Research* **2004**, 8, 501.
- [4] Pera-Titus, M.; García-Molina, V.; Baños, M. A.; Giménez, J.; Esplugas, S. *Applied Catalysis B: Environmental* **2004**, 47, 219.
- [5] Bartlett, A. A. *Am. J. Phys.* **1986**, 54, 398.
- [6] Mann, M. E.; Bradley, R. S.; Hughes, M. K. *Nature* **1998**, 392, 779.
- [7] Hoffert, M. I.; Caldeira, K.; Benford, G.; Criswell, D. R.; Green, C.; Herzog, H.; Jain, A. K.; Khesghi, H. S.; Lackner, K. S.; Lewis, J. S.; Lightfoot, H. D.; Manheimer, W.; Mankins, J. C.; Mauel, M. E.; Perkins, L. J.; Schlesinger, M. E.; Volk, T.; Wigley, T. M. L. *Science* **2002**, 298, 981.
- [8] Hoffert, M. I.; Caldeira, K.; Jain, A. K.; Haites, E. F.; Harvey, L. D. D.; Potter, S. D.; Schlesinger, M. E.; Schneider, S. H.; Watts, R. G.; Wigley, T. M. L.; Wuebbles, D. J. *Nature* **1998**, 395, 881.
- [9] Kamat, P. V. *The Journal of Physical Chemistry C* **2007**, 111, 2834.
- [10] Hubbert, M. K. *Science* **1949**, 109, 103.
- [11] Hubbert, M. K. *Am. J. Phys.* **1981**, 49, 1007.
- [12] Deffeyes, K. S. *Hubbert's Peak: The Impending World Oil Shortage*; Princeton University Press, 2001.
- [13] Fujishima, A.; Honda, K. *Nature* **1972**, 238, 37.
- [14] Clark, R. J. H. *Comprehensive Inorganic Chemistry*, 1973; Vol. 3.
- [15] Kirk, R. E.; Othmer, D. F. *Encyclopedia of Chemical Technology*; John Wiley and Sons, 1963.
- [16] Fox, M. A.; Dulay, M. T. *Chemical Reviews* **1993**, 93, 341.
- [17] Hoffmann, M. R.; Martin, S. T.; Choi, W.; Bahnemann, D. W. *Chemical Reviews* **1995**, 95, 69.
- [18] Kamat, P. V. *Chemical Reviews* **1993**, 93, 267.

- [19] Linsebigler, A. L.; Lu, G.; Yates, J. T. *Chemical Reviews* **1995**, *95*, 735.
- [20] Zhu, C.; Wang, L.; Kong, L.; Yang, X.; Wang, L.; Zheng, S.; Chen, F.; MaiZhi, F.; Zong, H. *Chemosphere* **2000**, *41*, 303.
- [21] Martin, S. T.; Herrmann, H.; Choi, W.; Hoffmann, M. R. *Journal of the Chemical Society, Faraday Transactions* **1994**, *90*, 3315.
- [22] Martin, S. T.; Herrmann, H.; Hoffmann, M. R. *Journal of the Chemical Society, Faraday Transactions* **1994**, *90*, 3323.
- [23] Muscat, J.; Swamy, V.; Harrison, N. M. *Physical Review B* **2002**, *65*, 224112.
- [24] Mo, S.-D.; Ching, W. Y. *Physical Review B* **1995**, *51*, 13023.
- [25] Li, J.-G.; Ishigaki, T.; Sun, X. *The Journal of Physical Chemistry C* **2007**, *111*, 4969.
- [26] Elizardo, K. In *Pollution Engineering* 1991, p 106.
- [27] Carraway, E. R.; Hoffman, A. J.; Hoffmann, M. R. *Environmental Science & Technology* **1994**, *28*, 786.
- [28] Ishibashi, K.-i.; Fujishima, A.; Watanabe, T.; Hashimoto, K. *Journal of Photochemistry and Photobiology A: Chemistry* **2000**, *134*, 139.
- [29] Kormann, C.; Bahnemann, D. W.; Hoffmann, M. R. *Environmental Science & Technology* **1991**, *25*, 494.
- [30] Stafford, U.; Gray, K. A.; Kamat, P. V. *Heterogeneous Chem. Rev.* **1996**, *3*, 77.
- [31] Fox, M. A.; Dulay, M. T. *Journal of Photochemistry and Photobiology A: Chemistry* **1996**, *98*, 91.
- [32] Rothenberger, G.; Moser, J.; Graetzel, M.; Serpone, N.; Sharma, D. K. *Journal of the American Chemical Society* **1985**, *107*, 8054.
- [33] Chen, D.; Ray, A. K. *Applied Catalysis B: Environmental* **1999**, *23*, 143.
- [34] Crittenden, J. C.; Liu, J.; Hand, D. W.; Perran, D. L. *Water Res.* **1997**, *31*, 429.
- [35] Kudo, A.; Hijii, S. *Chem. Lett.* **1999**, *28*, 1103.
- [36] Okamoto, K.; Yamamoto, Y.; Tanaka, H.; Itaya, A. *Bull. Chem. Soc. Jpn.* **1985**, *58*, 2023.
- [37] Yu, Y.; Leu, R. M.; Lee, K. C. *Water Res.* **1996**, *30*, 1169.

- [38] Curc3, D.; Gim3nez, J.; Addardak, A.; Cervera-March, S.; Esplugas, S. *Catalysis Today* **2002**, *76*, 177.
- [39] Styliidi, M.; Kondarides, D. I.; Verykios, X. E. *Applied Catalysis B: Environmental* **2004**, *47*, 189.
- [40] Bahemann, D. W.; Kormann, C.; Hoffmann, M. R. *J. Phys. Chem.* **1987**, *91*, 3789.
- [41] Faust, B. C.; Hoffmann, M. R.; Bahnemann, D. W. *J. Phys. Chem.* **1989**, *93*, 6371.
- [42] Kormann, C.; Bahnemann, D. W.; Hoffmann, M. R. *The Journal of Physical Chemistry* **1988**, *92*, 5196.
- [43] Riddick, T. M. *Zeta-Meter Manual.*; Zeta Meter Inc.: New York., 1968.
- [44] Zeta Potential of Colloids in Water and Waste Water, A. S. D.-. Materials, A. S. f. T. a., Ed. 1985.
- [45] Gaya, U. I.; Abdullah, A. H. *Journal of Photochemistry and Photobiology C: Photochemistry Reviews* **2008**, *9*, 1.
- [46] Evgenidou, E.; Fytianos, K.; Poulios, I. *Applied Catalysis B: Environmental* **2005**, *59*, 81.
- [47] Fu, X.; Clark, L. A.; Zeltner, W. A.; Anderson, M. A. *Journal of Photochemistry and Photobiology A: Chemistry* **1996**, *97*, 181.
- [48] Muradov, N. Z.; T-Raissi, A.; Muzzey, D.; Painter, C. R.; Kemme, M. R. *Solar Energy* **1996**, *56*, 445.
- [49] Tunesi, S.; Anderson, M. A. *Chemosphere* **1987**, *16*, 1447.
- [50] Fujishima, A.; Rao, T. N.; Tryk, D. A. *Journal of Photochemistry and Photobiology C: Photochemistry Reviews* **2000**, *1*, 1.
- [51] Heller, A. *Accounts of Chemical Research* **1995**, *28*, 503.
- [52] Ljjna, S. *Nature* **1991**, *354*, 56.
- [53] Ollis, D. F.; Pelizzetti, E.; Serpone, N. *Environ. Sci. Technol.* **1991**, *25*, 1522.
- [54] Mills, A.; Le Hunte, S. *Journal of Photochemistry and Photobiology A: Chemistry* **1997**, *108*, 1.
- [55] Berger, T.; Sterrer, M.; Diwald, O.; Kn3zinger, E. *ChemPhysChem* **2005**, *6*, 2104.

- [56] Berger, T.; Sterrer, M.; Diwald, O.; Knäuper, E.; Panayotov, D.; Thompson, T. L.; Yates, J. T. *The Journal of Physical Chemistry B* **2005**, *109*, 6061.
- [57] Nakaoka, Y.; Nosaka, Y. *Journal of Photochemistry and Photobiology A: Chemistry* **1997**, *110*, 299.
- [58] Gerischer, H.; Heller, A. *J. Electrochem. Soc.* **1992**, *139*, 113.
- [59] Gerischer, H.; Heller, H. *J. Phys. Chem.* **1991**, *95*, 5261.
- [60] Wang, C. M.; Heller, A.; Gerischer, H. *J. Am. Chem. Soc.* **1992**, *114*, 5230.
- [61] Jun, Y.; et al. *Journal of Applied Physics* **2006**, *99*, 084908.
- [62] Muggli, D. S.; Falconer, J. L. *Journal of Catalysis* **1999**, *187*, 230.
- [63] Muggli, D. S.; Falconer, J. L. *Journal of Catalysis* **2000**, *191*, 318.
- [64] Yoshida, K.; Nanbara, T.; Yamasaki, J.; Tanaka, N. *J. Appl. Phys.* **2006**, *99*, 084908.
- [65] Yoshida, K.; Yamasaki, J.; Tanaka, N. *Appl. Phys. Lett.* **2004**, *84*, 2542.
- [66] Carp, O.; Huisman, C. L.; Reller, A. *Progress in Solid State Chemistry* **2004**, *32*, 33.
- [67] Ohno, T.; Akiyoshi, M.; Umebayashi, T.; Asai, K.; Mitsui, T.; Matsumura, M. *Applied Catalysis A: General* **2004**, *265*, 115.
- [68] Ohno, T.; Tanigawa, F.; Fujihara, K.; Izumi, S.; Matsumura, M. *Journal of Photochemistry and Photobiology A: Chemistry* **1999**, *127*, 107.
- [69] Patrick, B.; Kamat, P. V. *The Journal of Physical Chemistry* **1992**, *96*, 1423.
- [70] Bahnemann, D. W. *Israel Journal of Chemistry* **1993**, *33*, 115.
- [71] Anpo, M.; Shima, T.; Kodama, S.; Kubokawa, Y. *The Journal of Physical Chemistry* **1987**, *91*, 4305.
- [72] Hagfeldt, A.; Graetzel, M. *Chemical Reviews* **1995**, *95*, 49.
- [73] Henglein, A. *Berichte der Bunsen-Gesellschaft-Physical Chemistry* **1997**, *101*, 1562.
- [74] Weller, H.; Eychmuller, A. *Advances in Photochemistry*; John Wiley and Sons. Inc., 1995; Vol. 20.
- [75] Hoffman, A. J.; Carraway, E. R.; Hoffmann, M. R. *Environmental Science & Technology* **1994**, *28*, 776.

- [76] Nedeljkovic, J. M.; Nenadovic, M. T.; Micic, O. I.; Nozik, A. J. *The Journal of Physical Chemistry* **1986**, *90*, 12.
- [77] Nosaka, Y.; Ohta, N.; Miyama, H. *The Journal of Physical Chemistry* **1990**, *94*, 3752.
- [78] Hoffman, A. J.; Mills, G.; Yee, H.; Hoffmann, M. R. *The Journal of Physical Chemistry* **1992**, *96*, 5546.
- [79] Lepore, G. P.; Langford, C. H.; Víchová, J.; Vlcek, A. *Journal of Photochemistry and Photobiology A: Chemistry* **1993**, *75*, 67.
- [80] Morales, A. M.; Lieber, C. M. *Science* **1998**, *279*, 208.
- [81] Pan, Z. W.; Dai, Z. R.; Wang, Z. L. *Science* **2001**, *291*, 1947.
- [82] Dai, Z. R.; Pan, Z. W.; Wang, Z. L. *Journal of the American Chemical Society* **2002**, *124*, 8673.
- (83) Shen, G.; Bando, Y.; Liu, B.; Golberg, D.; Lee, C. J. *Advanced Functional Materials* **2006**, *16*, 410.
- [84] Wang, Z. L. *J. Phys. Condens. Matter.* **2004**, *16*, R829.
- [85] Ye, C.; Fang, X.; Hao, Y.; Teng, X.; Zhang, L. *The Journal of Physical Chemistry B* **2005**, *109*, 19758.
- [86] Burda, C.; Chen, X.; Narayanan, R.; El-Sayed, M. A. *Chem. Rev.*, **2005**, *105*, 1025.
- [87] Amano, F.; Nogami, K.; Abe, R.; Ohtani, B. *The Journal of Physical Chemistry C* **2008**, *112*, 9320.
- [88] Jang, E.; Won, J. H.; Hwang, S. J.; Choy, J. H. *Advanced Materials* **2006**, *18*, 3309.
- [89] Jang, J. S.; Yu, C.-J.; Choi, S. H.; Ji, S. M.; Kim, E. S.; Lee, J. S. *Journal of Catalysis* **2008**, *254*, 144.
- [90] Ye, C.; Bando, Y.; Shen, G.; Golberg, D. *The Journal of Physical Chemistry B* **2006**, *110*, 15146.
- [91] Serpone, N.; Lawless, D.; Khairutdinov, R. *The Journal of Physical Chemistry* **1995**, *99*, 16646.
- [92] Anpo, M.; Aikawa, N.; Kubokawa, Y.; Che, M.; Louis, C.; Giamello, E. *The Journal of Physical Chemistry* **1985**, *89*, 5017.
- [93] Sasaki, T.; Nakano, S.; Yamauchi, S.; Watanabe, M. *Chemistry of Materials* **1997**, *9*, 602.

- [94] Li, L.; Liu, C.-y.; Liu, Y. *Materials Chemistry and Physics* **2009**, *113*, 551.
- [95] Takahashi, R.; Sato, S.; Sodesawa, T.; Arai, K.; Yabuki, M. *J. Catal.* **2005**, *229*, 24.
- [96] Asahi, R.; Morikawa, T.; Ohwaki, T.; Aoki, K.; Taga, Y. *Science* **2001**, *293*, 269.
- [97] Irie, H.; Watanabe, Y.; Hashimoto, K. *Chem. Lett.* **2003**, *32*, 772.
- [98] Nakahira, A.; Konishi, K.; Yokota, K.; Honma, T.; Aritani, H.; Tanaka, K. *J. Ceram. Soc. Jpn.* **2006**, *114*, 46.
- [99] Umebayashi, T.; Yamaki, T.; Itoh, H.; Asai, K. *Journal of Physics and Chemistry of Solids* **2002**, *63*, 1909.
- [100] Nagaveni, K.; Hegde, M. S.; Madras, G. *The Journal of Physical Chemistry B* **2004**, *108*, 20204.
- [101] Anpo, M.; Takeuchi, M. *Journal of Catalysis*, *216*, 505.
- [102] Anpo, M.; Takeuchi, M.; Ikeue, K.; Dohshi, S. *Current Opinion in Solid State and Materials Science* **2002**, *6*, 381.
- [103] Briand, L. E.; Bonetto, R. D.; Sanchez, M. A.; Thomas, H. J. *Catalysis Today* **1996**, *32*, 205.
- [104] Yamashita, H.; Anpo, M. *Catalysis Surveys from Asia* **2004**, *8*, 35.
- [105] Yamashita, H.; Harada, M.; Misaka, J.; Takeuchi, M.; Ikeue, K.; Anpo, M. *Journal of Photochemistry and Photobiology A: Chemistry* **2002**, *148*, 257.
- [106] Gu, D.-E.; Yang, B.-C.; Hu, Y.-D. *Catalysis Letters* **2007**, *118*, 254.
- [107] Martin, S. T.; Morrison, C. L.; Hoffmann, M. R. *The Journal of Physical Chemistry* **1994**, *98*, 13695.
- [108] Wu, J. C. S.; Chen, C.-H. *Journal of Photochemistry and Photobiology A: Chemistry* **2004**, *163*, 509.
- [109] Kiosek, S.; Raftery, D. J. *J. Phys. Chem* **2001**, *105*, 2815.
- [110] Zhao, Z.; Yamada, Y.; Teng, Y.; Ueda, A.; Nakagawa, K.; Kobayashi, T. *Journal of Catalysis* **2000**, *190*, 215.
- [111] Tedeschi, S.; Stevens, N.; Cepeda, D.; Lee, Y.-Y.; Powers, K.; Ranade, M.; El-Shall, H. *Powder Technology* **2009**, *191*, 188.

- [112] Maile, F. J.; Pfaff, G.; Reynders, P. *Progress in Organic Coatings* **2005**, *54*, 150.
- [113] Pfaff, G.; Reynders, P. *Chemical Reviews* **1999**, *99*, 1963.
- [114] Inagaki, M.; Imai, T.; Yoshikawa, T.; Tryba, B. *Applied Catalysis B: Environmental* **2004**, *51*, 247.
- [115] Zhang, Z.; Wang, C.-C.; Zakaria, R.; Ying, J. Y. *The Journal of Physical Chemistry B* **1998**, *102*, 10871.
- [116] Baiju, K. V.; Shukla, S.; Sandhya, K. S.; James, J.; Warriar, K. G. K. *The Journal of Physical Chemistry C* **2007**, *111*, 7612.
- [117] Sasaki, T.; Watanabe, M. *The Journal of Physical Chemistry B* **1997**, *101*, 10159.
- [118] Kanta, A.; Sedev, R.; Ralston, J. *Langmuir* **2005**, *21*, 2400.
- [119] Parfitt, G. D. *Pure Appl. Chem.* **1976**, *48*, 415.
- [120] Crist, B. C. *Handbook of Monochromatic XPS Spectra: The Elements and Native Oxides*; Wiley, 2000.
- [121] Parfitt, G. D. *Progress in Surface and Membrane Science*; Academic Press, 1976.
- [122] Kim, G. M.; Lee, S. M.; Michler, G. H.; Roggendorf, H.; Gösele, U.; Knez, M. *Chemistry of Materials* **2008**, *20*, 3085.
- [123] Sun, L.; Bolton, J. R. *The Journal of Physical Chemistry* **1996**, *100*, 4127.
- [124] Lachheb, H.; Puzenat, E.; Houas, A.; Ksibi, M.; Elaloui, E.; Guillard, C.; Herrmann, J.-M. *Applied Catalysis B: Environmental* **2002**, *39*, 75.
- [125] Ohno, T.; Sarukawa, K.; Tokieda, K.; Matsumura, M. *J. of Catal.* **2001**, *203*, 82.
- [126] Hurum, D. C.; Agrios, A. G.; Gray, K. A.; Rajh, T.; Thurnauer, M. C. *The Journal of Physical Chemistry B* **2003**, *107*, 4545.
- [127] Aguedach, A.; Brosillon, S.; Morvan, J.; Lhadi, E. K. *Applied Catalysis B: Environmental* **2005**, *57*, 55.
- [128] De Heredia, J. B.; Torregrosa, J.; Dominguez, J. R.; Peres, J. A. *Journal of Hazardous Materials* **2001**, *83*, 255.
- [129] Kusvuran, E.; Gulnaz, O.; Irmak, S.; Atanur, O. M.; Ibrahim Yavuz, H.; Erbatur, O. *Journal of Hazardous Materials* **2004**, *109*, 85.

- [130] Tanaka, K.; Padermpole, K.; Hisanaga, T. *Water Research* **2000**, *34*, 327.
- [131] Tang, W. Z.; Huren, A. *Chemosphere* **1995**, *31*, 4157.
- [132] Houas, A.; Lachheb, H.; Ksibi, M.; Elaloui, E.; Guillard, C.; Herrmann, J.-M. *Applied Catalysis B: Environmental* **2001**, *31*, 145.
- [133] Madia, G.; Elsener, M.; Koebel, M.; Raimondi, F.; Wokaun, A. *Applied Catalysis B-Environmental* **2002**, *39*, 181.
- [134] Reddy, B. M.; Ganesh, I.; Reddy, E. P. *The Journal of Physical Chemistry B* **1997**, *101*, 1769.
- [135] Fern'ndez-Garc'a, M.; Mart'nez-Arias, A.; Hanson, J. C.; Rodriguez, J. A. *Chemical Reviews* **2004**, *104*, 4063.
- [136] Kemp, T. J.; McIntyre, R. A. *Polymer Degradation and Stability* **2006**, *91*, 165.
- [137] Sene, J. J.; Zeltner, W. A.; Anderson, M. A. *The Journal of Physical Chemistry B* **2003**, *107*, 1597.
- [138] Karvinen, S. M. *Industrial & Engineering Chemistry Research* **2003**, *42*, 1035.
- [139] Di Paola, A.; Marc, G.; Palmisano, L.; Schiavello, M.; Uosaki, K.; Ikeda, S.; Ohtani, B. *The Journal of Physical Chemistry B* **2001**, *106*, 637.
- [140] Marci, G.; Palmisano, L.; Sclafani, A.; Venezia, A. M.; Campostrini, R.; Carturan, G.; Martin, C.; Rives, V.; Solana, G. *Journal of the Chemical Society, Faraday Transactions* **1996**, *92*, 819.
- [141] Bhattacharyya, K.; Varma, S.; Tripathi, A. K.; Bharadwaj, S. R.; Tyagi, A. K. *The Journal of Physical Chemistry C* **2008**, *112*, 19102.
- [142] Forzatti, P.; Tronconi, E.; Busca, G.; Tittarelli, P. *Catalysis Today* **1987**, *1*, 209.
- [143] Ivanova, T.; Harizanova, A.; Surtchev, M.; Nenova, Z. *Solar Energy Materials and Solar Cells* **2003**, *76*, 591.
- [144] Luca, V.; Thomson, S.; F. Howe, R. *Journal of the Chemical Society, Faraday Transactions* **1997**, *93*, 2195.
- [145] Depero, L. E.; Bonzi, P.; Musci, M.; Casale, C. *Journal of Solid State Chemistry* **1994**, *111*, 247.
- [146] Iketani, K.; Sun, R.-D.; Toki, M.; Hirota, K.; Yamaguchi, O. *Materials Science and Engineering B* **2004**, *108*, 187.

- [147] Kumar, P. M.; Badrinarayanan, S.; Sastry, M. *Thin Solid Films* **2000**, 358, 122.
- [148] Sleigh, C.; Pijpers, A. P.; Jaspers, A.; Coussens, B.; Meier, R. J. *Journal of Electron Spectroscopy and Related Phenomena* **1996**, 77, 41.
- [149] Stakheev, A. Y.; Shpiro, E. S.; Apijok, J. *The Journal of Physical Chemistry* **1993**, 97, 5668.
- [150] Robba, D.; Ori, D. M.; Sangalli, P.; Chiarello, G.; Depero, L. E.; Parmigiani, F. *Surface Science* **1997**, 380, 311.
- [151] Casaletto, M. P.; Kaciulis, S.; Lisi, L.; Mattogno, G.; Mezzi, A.; Patrono, P.; Ruoppolo, G. *Applied Catalysis A: General* **2001**, 218, 129.
- [152] Kobayashi, M.; Miyaji, K.; Saitoh, M.; Hiramoto, T. In *Semiconductor Device Research Symposium, 2005 International* 2005, p 173.
- [153] Lars, S.; Andersson, T. *Catalysis Letters* **1990**, 7, 351.
- [154] Mizushima, K.; Tanaka, M.; Asai, A.; Iida, S.; Goodenough, J. B. *Journal of Physics and Chemistry of Solids* **1979**, 40, 1129.
- [155] Moshfegh, A. Z.; Ignatiev, A. *Catalysis Letters* **1990**, 4, 113.
- [156] Sawatzky, G. A.; Post, D. *Physical Review B* **1979**, 20, 1546.
- [157] Wong, G. S.; Concepcion, M. R.; Vohs, J. M. *Surface Science* **2003**, 526, 211.
- [158] Trifir, F. *Catalysis Today* **1998**, 41, 21.
- [159] Herrmann, J.-M.; Disdier, J.; Deo, G.; E. Wachs, I. *Journal of the Chemical Society, Faraday Transactions* **1997**, 93, 1655.
- [160] O'Regan, B.; Gratzel, M. *Nature* **1991**, 353, 737.
- [161] Chiba, Y.; Islam, A.; Watanabe, Y.; Komyia, R.; Koide, N.; Han, L. *Japanese Journal of Applied Physics* **2006**, 45, L638.
- [162] Jose, R.; Thavasi, V.; Ramakrishna, S. *J. Am. Ceram. Soc.* **2009**, 92, 289.
- [163] Snaith, H.; Schmidt-Mende, L. *Advanced Materials* **2007**, 19, 3187.
- [164] Lee, K. E.; Charbonneau, C.; Shan, G.; Demopoulos, G. P.; Gauvin, R. *JOM* **2009**, 61, 52.
- [165] Grätzel, M. *Progress in Photovoltaics: Research and Applications* **2000**, 8, 171.

- [166] Grätzel, M. *Progress in Photovoltaics: Research and Applications* **2006**, *14*, 429.
- [167] Hagfeldt, A.; Gratzel, M. *Accounts of Chemical Research* **2000**, *33*, 269.
- [168] Frank, J.; Nikos, K.; Jao van de, L. *Coordination Chemistry Reviews* **2004**, *248*, 1165.
- [169] Chen, D.; Huang, F.; Cheng, Y. B.; Caruso, R. A. *Advanced Materials* **2009**, *21*, 2206.
- [170] Vargas, W. E.; Niklasson, G. A. *Solar Energy Materials and Solar Cells* **2001**, *69*, 147.
- [171] Yang, L.; Lin, Y.; Jia, J.; Xiao, X.; Li, X.; Zhou, X. *Journal of Power Sources* **2008**, *182*, 370.
- [172] Jiang, X.; Herricks, T.; Xia, Y. *Advanced Materials* **2003**, *15*, 1205.
- [173] Zhang, M.; Lin, G.; Dong, C.; Wen, L. *Surface and Coatings Technology* **2007**, *201*, 7252.
- [174] Ito, S.; Zakeeruddin, S.; Humphry-Baker, R.; Liska, P.; Charvet, R.; Comte, P.; Nazeeruddin, M.; Péchy, P.; Takata, M.; Miura, H.; Uchida, S.; Grätzel, M. *Advanced Materials* **2006**, *18*, 1202.

BIOGRAPHICAL SKETCH

Yang-Yao Lee was born in Taipei City, Taiwan in 1977. He graduated from the Tatung in May 2000 and enrolled in the National Taiwan University for the master degree in materials science and engineering. He served the military service in 2002 and was discharged in 2004. He began the graduate studies at University of Florida in 2006 and joined Dr. Kevin Power's group in 2007. He received his Ph.D. from the Department of Materials Science and Engineering at University of Florida in the fall of 2010.